



UNIVERSITAT
POLITÈCNICA
DE VALÈNCIA



UNIVERSITAT POLITÈCNICA DE VALÈNCIA
DEPARTAMENTO DE INGENIERÍA ELECTRÓNICA

Computational Models and Experimentation for Radiofrequency-based Ablative Techniques

**“Modelos computacionales y experimentación
para técnicas ablativas por radiofrecuencia”**

Ph.D. THESIS

Ana González Suárez

ADVISORS

Dr. Enrique Berjano Zanón

Dra. Macarena Trujillo Guillén

Valencia, January 2014

“I am among those who think that science has great beauty. A scientist in his laboratory is not only a technician: he is also a child placed before natural phenomena which impress him like a fairy tale. We should not allow it to be believed that all scientific progress can be reduced to mechanisms, machines, gearings, even though such machinery has its own beauty.”

— **Marie Curie**. During a debate in Madrid ‘The Future of Culture’ (1933)

A mis padres y a Javi

Acknowledgements

In general, I would like to thank everybody who in one or another way has contributed to the achievement of this PhD Thesis.

Especially, I would like to express my deepest gratitude to my advisors, Enrique and Macarena, for giving me the wonderful opportunity to start my research work with them and for their support and invaluable guidance during these years. Without a shred of doubt, it was a real pleasure for me to work alongside you.

I am most grateful to the external reviewers, Dr. Tobias Preusser, Dr. Dieter Haemmerich and Dr. Punit Prakash, for their time and effort devoted to review the PhD Thesis manuscript, and for the valuable suggestions and comments they made, which unquestionably helped me to improve the quality of this work.

I do not want to forget to express my sincere gratitude to Dr. Walfre Franco for giving me the opportunity to train and conduct my predoctoral stay at The Wellman Center for Photomedicine and for his valuable support and help during those months. Undoubtedly, it was a pleasure for my working with him. I also want to thank Dr. Joel Jimenez-Lozano for the great help provided with the computational modeling of skin. Furthermore, I want to mention that one of the best things of my stay in Boston was undoubtedly the fact of meeting two wonderful people, Enoch and Monica, who they made me feel at home. I hope to see you both soon, either in Spain, México or USA.

Moreover, I would like to express my gratitude to the Conselleria d'Educació of the Generalitat Valenciana for the predoctoral grant VaLi+D (ACIF/2011/194), which provided me the financial support to conduct during these last years the development of this PhD Thesis and allowed me to participate in several projects (TEC2008-01369, TEC2011-27133-C02-01, INNOVA11-01-5502, PAID-06-11 Ref. 1988 and UPV-FE-5040); and also for the predoctoral visiting fellowship (BEFPI/2013/003) that gave me the financial support to do a stay for 4 months.

Finally, I would like to dedicate my dissertation work to my parents and Javi. I sincerely believe that I would have not been able to conclude this work without their infinite patience, support and understanding at all times.

Abstract

Ablative techniques based on radiofrequency (RF) energy are used to produce a safe and localized heating of target biological tissue. In recent years there has been rapid growth in the number of new medical procedures employing these techniques, accompanied by the emergence of new electrode designs and energy delivery protocols. However, there are still many unknowns about the true electro-thermal behavior of energy applicators, along with energy-tissue interaction issues in specific applications.

The main purpose of this PhD Thesis is to gain a better understanding of the electrical and thermal phenomena involved in the heating of biological tissues by RF currents, in order to improve the efficacy and safety of the techniques currently used in clinical practice in different areas, such as cardiac surgery, oncology and dermatology. An additional aim is to suggest technological improvements for designing new applicators. The Thesis combines two methodologies widely used in the field of Biomedical Engineering: computational modeling (mathematical) and experimental (*ex vivo* and *in vivo*) tests.

Our cardiac research was focused on improving intraoperative ablation of atrial fibrillation by an epicardial (minimally invasive) approach. To do this, we used mathematical models to assess an impedance measurement system as a method of quantifying the amount of epicardial fat present prior to ablation. We also studied how to improve ablation of the ventricular wall using an endocardial-endocardial approach (interventricular septum) and an endocardial-epicardial approach (ventricular free wall). This involved comparing computer simulations of the efficiency of bipolar and unipolar modes of ablation in terms of the transmural of the lesion across the ventricular wall.

Surgical oncology focused on RF-assisted hepatic resection. RF heating techniques should be able to minimize intraoperative bleeding and seal vessels and ducts by creating a thermal coagulative necrosis. If this heating occurs in the vicinity of large vessels, there is a risk of damage to this vessel. Using mathematical models

and in vivo experiments, we evaluated whether the effect of blood flow within a large vessel would be able to thermally protect the wall when RF-assisted resection is performed in the vicinity. We also conducted computational and ex vivo and in vivo experimental studies on the electro-thermal behavior of bipolar internally cooled RF applicators. These are a safer alternative to the monopolar applicators due to the fact that RF currents flow almost exclusively through the biological tissue between the electrodes.

The dermatological area focused on improving the treatment of disorders of the subcutaneous tissue (e.g. lipomatosis, lipedema, Madelung disease and cellulite) by a theoretical study of the optimum dosimetry for each case. For this we evaluated the electrical, thermal and thermo-elastic effects of two different structures of subcutaneous tissue during RF heating, as well as the thermal damage to both structures after heating has been quantified.

Resumen

Las técnicas ablativas basadas en energía por radiofrecuencia (RF) se emplean con el fin de lograr un calentamiento seguro y localizado en el tejido biológico. En los últimos años ha habido un rápido crecimiento en el número de nuevos procedimientos médicos que hacen uso de dichas técnicas, lo cual ha ido acompañado de la aparición de nuevos diseños de electrodos y protocolos de aplicación de energía. Sin embargo, existen todavía muchas incógnitas sobre el verdadero comportamiento electro-térmico de los aplicadores de energía, así como de la interacción energía-tejido en aplicaciones concretas.

El principal propósito de esta Tesis Doctoral es adquirir un mejor conocimiento de los fenómenos eléctricos y térmicos involucrados en los procesos de calentamiento de tejidos biológicos mediante corrientes de RF. Esto permitirá, por un lado, mejorar la eficacia y seguridad de las técnicas actualmente empleadas en la clínica en campos tan diferentes como la cirugía cardíaca, oncológica o dermatológica; y por otro, sugerir mejoras tecnológicas para el diseño de nuevos aplicadores. La Tesis Doctoral combina dos metodologías ampliamente utilizadas en el campo de la Ingeniería Biomédica, como son el modelado computacional (matemático) y la experimentación (*ex vivo* e *in vivo*).

En cuanto al área cardíaca, la investigación se ha centrado, por una parte, en mejorar la ablación intraoperatoria de la fibrilación auricular por aproximación epicárdica, es decir, susceptible de ser realizada de forma mínimamente invasiva. Para ello, se ha estudiado mediante modelos matemáticos un sistema de medida de la impedancia epicárdica como método de valoración de la cantidad de grasa previo a la ablación. Por otra parte, se ha estudiado cómo mejorar la ablación de la pared ventricular por aproximación endocárdica-endocárdica (septo interventricular) y endocárdica-epicárdica (pared libre del ventrículo). Con este objetivo, se han comparado mediante modelado por computador la eficacia de los modos de ablación

bipolar y unipolar en términos de la transmuralidad de la lesión en la pared ventricular.

En lo que respecta al área de cirugía oncológica, la investigación se ha centrado en la resección hepática asistida por RF. Las técnicas de calentamiento por RF deberían ser capaces de minimizar el sangrado intraoperatorio y sellar vasos y ductos mediante la creación de una necrosis coagulativa por calentamiento. Si este calentamiento se produce en las cercanías de grandes vasos, existe un problema potencial de daño a la pared de dicho vaso. En este sentido, se ha evaluado con modelos matemáticos y experimentación in vivo si el efecto del flujo de sangre dentro de un gran vaso es capaz de proteger térmicamente su pared cuando se realiza una resección asistida por RF en sus cercanías. Además, se ha realizado un estudio computacional y experimental ex vivo e in vivo del comportamiento electro-térmico de aplicadores de RF bipolares internamente refrigerados, puesto que representan una opción más segura frente a los monopolares en la medida en que las corrientes de RF fluyen casi exclusivamente por el tejido biológico situado entre ambos electrodos.

Respecto al área dermatológica, la investigación se ha centrado en mejorar el tratamiento de enfermedades o desórdenes del tejido subcutáneo (tales como lipomatosis, lipedema, enfermedad de Madelung y celulitis) mediante el estudio teórico de la dosimetría correcta en cada caso. Para ello, se han evaluado los efectos eléctricos, térmicos y termo-elásticos de dos estructuras diferentes de tejido subcutáneo durante el calentamiento por RF, y se ha cuantificado el daño térmico producido en ambas estructuras tras dicho calentamiento.

Resum

Les tècniques ablatives basades en radiofreqüència (RF) es fan servir amb el propòsit d'aconseguir un escalfament segur i localitzat en el teixit biològic. Als darrers anys hi ha hagut un ràpid creixement en el nombre de nous procediments mèdics que fan ús d'aquestes tècniques, la qual cosa ha anat acompanyada de l'aparició de nous dissenys d'elèctrodes i protocols d'aplicació d'energia. Tanmateix, encara hi ha moltes incògnites sobre el vertader comportament electro-tèrmic dels aplicadors d'energia, així com de la interacció energia-teixit en aplicacions concretes.

El principal propòsit d'aquesta Tesi Doctoral és aconseguir un millor coneixement dels fenòmens elèctrics i tèrmics implicats en els processos de escalfament de teixits biològics mitjançant corrents de RF. Això permetrà, d'una banda, millorar l'eficàcia i seguretat de les tècniques actualment emprades en la clínica en camps tan diferents com ara la cirurgia cardíaca, oncològica o dermatològica; i, de l'altra banda, suggerir millores tecnològiques en el disseny de nous aplicadors. La Tesi combina dues metodologies àmpliament emprades en el camp de l'Enginyeria Biomèdica, com són el modelatge computacional (matemàtic) i l'experimentació (ex vivo i in vivo).

En l'àrea cardíaca, la recerca s'ha centrat, d'una banda, en la millora de l'ablació intraoperatòria de la fibril·lació auricular fent ús de l'aproximació epicàrdica, és a dir, susceptible de ser duta a terme de manera mínimament invasiva. Per a això s'ha estudiat, mitjançant models matemàtics, un sistema de mesura de la impedància epicàrdica com a mètode de valoració de la quantitat de greix previ a l'ablació. D'altra banda, s'ha estudiat com millorar l'ablació de la paret ventricular per aproximació endocàrdica-endocàrdica (septum interventricular) i endocàrdica-epicàrdica (paret lliure del ventricle). Amb aquest objectiu, s'ha comparat, mitjançant modelatge per computador, l'eficàcia dels modes d'ablació bipolar i unipolar en termes de la transmuralitat de la lesió en la paret ventricular.

En l'àrea de la cirurgia oncològica, la recerca s'ha centrat en la resecció hepàtica assistida per RF. Les tècniques de escalfament per RF haurien de ser capaces de minimitzar el sagnat intraoperatori i segellar vasos i ductes mitjançant la creació d'una necrosi coagulativa per calfament. Si aquest escalfament es produeix prop de grans vasos, existeix el problema potencial de dany a la seva paret. En aquest sentit, s'ha avaluat amb models matemàtics i experimentació in vivo si l'efecte del cabal de sang dins del vas és capaç de protegir tèrmicament la seva paret quan es realitza una resecció assistida per RF al seu voltant. A més, s'ha realitzat un estudi computacional i experimentació ex vivo i in vivo del comportament electro-tèrmic d'aplicadors de RF de tipus bipolar i internament refrigerats, ja que representen una opció més segura front als monopolars en la mesura que els corrents de RF circulen gairebé exclusivament pel teixit biològic localitzat entre els dos elèctrodes.

En l'àrea dermatològica, la recerca s'ha centrat en la millora del tractament de malalties o alteracions de teixit subcutani (com per exemple lipomatosis, lipedema, malaltia de Madelung i cel·lulitis) mitjançant l'estudi teòric de la dosimetria correcta en cada cas. Per a això, s'han avaluat els efectes elèctrics, tèrmics i termo-elàstics de dues estructures diferents de teixit subcutani durant el calfament per RF, i s'ha quantificat el dany tèrmic produït en ambdues estructures després d'aquest escalfament.

Table of Contents

ACKNOWLEDGEMENTS	XII
ABSTRACT	VIII
RESUMEN	XI
RESUM	XIII
LIST OF ACRONYMS	XXI
LIST OF SYMBOLS	XXII
CHAPTER 1. INTRODUCTION	25
1.1. Background: Radiofrequency ablation (RFA).....	25
1.1.1. <i>RFA modes</i>	26
1.1.2. <i>Electrode design</i>	28
1.1.3. <i>Clinical applications</i>	29
1.1.3.a. <i>RF cardiac ablation</i>	29
1.1.3.b. <i>RF-assisted hepatic resection</i>	34
1.1.3.c. <i>RF heating of subcutaneous adipose tissue</i>	37
1.2. Objectives and Organization.....	41
CHAPTER 2. MATHEMATICAL MODELING OF EPICARDIAL RF ABLATION OF ATRIAL TISSUE WITH OVERLYING EPICARDIAL FAT	45
2.1. Abstract.....	45
2.2. Introduction.....	46
2.3. Methods.....	47
2.3.1. <i>Description of the theoretical model</i>	47
2.3.2. <i>Governing equations</i>	48
2.3.3. <i>Characteristics of model elements</i>	49
2.3.4. <i>Boundary and initial conditions</i>	50

2.3.5. <i>Construction of the numerical model</i>	50
2.3.6. <i>Modeling the RF ablation mode</i>	51
2.3.7. <i>Modeling the ablation with a cooled electrode</i>	52
2.4. Results.....	52
2.4.1. <i>Construction of the model</i>	52
2.4.2. <i>Effect of frequency for the dry electrode case</i>	52
2.4.3. <i>Ablation with cooled electrode</i>	53
2.4.4. <i>Comparison between ablation techniques</i>	54
2.5. Discussion.....	54
2.6. Conclusions.....	57

CHAPTER 3. IMPEDANCE MEASUREMENT TO ASSESS EPICARDIAL FAT PRIOR TO RF INTRAOPERATIVE CARDIAC ABLATION: FEASIBILITY STUDY USING A COMPUTER MODEL.....69

3.1. Abstract.....	69
3.2. Introduction.....	70
3.3. Methods.....	71
3.3.1. <i>Description of the theoretical model</i>	71
3.3.2. <i>Impedance measuring technique</i>	72
3.3.3. <i>Governing equations</i>	72
3.3.4. <i>Boundary conditions</i>	73
3.3.5. <i>Construction of the numerical model</i>	73
3.3.6. <i>Effect of different fat profiles</i>	74
3.3.7. <i>Effect of lateral width of epicardial fat</i>	74
3.4. Results.....	75
3.4.1. <i>Construction of the model</i>	75
3.4.2. <i>Effect of different fat profiles</i>	75
3.4.3. <i>Effect of lateral width of epicardial fat</i>	76
3.5. Discussion.....	76
3.6. Conclusions.....	77

CHAPTER 4. RF ABLATION WITH CATHETERS PLACED ON OPPOSING SIDES OF THE VENTRICULAR WALL: COMPUTER MODELING COMPARING BIPOLAR AND UNIPOLAR MODES	85
4.1. Abstract	85
4.2. Introduction.....	86
4.3. Materials and methods	87
4.3.1. <i>Computer modeling</i>	87
4.4. Results.....	91
4.4.1. <i>Development of computational models</i>	91
4.4.2. <i>Interventricular septum ablation</i>	92
4.4.3. <i>Ventricular free wall ablation</i>	92
4.4.4. <i>Effect of air on the epicardial side</i>	93
4.4.5. <i>Effect of changing the orientation of epicardial catheter</i>	93
4.4.6. <i>Effect of the misalignment of catheters</i>	94
4.5. Discussion.....	94
4.5.1. <i>Study Limitations</i>	97
4.6. Conclusions.....	97
CHAPTER 5. FEASIBILITY STUDY OF AN INTERNALLY COOLED BIPOLAR APPLICATOR FOR RF COAGULATION OF HEPATIC TISSUE: EXPERIMENTAL AND COMPUTATIONAL STUDY	109
5.1. Abstract	109
5.2. Introduction.....	110
5.3. Materials and methods	112
5.3.1. <i>Description of the device</i>	112
5.3.2. <i>Ex vivo experimental setup</i>	112
5.3.3. <i>In vivo experimental setup</i>	113
5.3.4. <i>Computational modeling</i>	114
5.4. Results.....	119
5.5. Discussion.....	121
5.6. Conclusions.....	124

CHAPTER 6. COULD THE HEAT SINK EFFECT OF BLOOD FLOW INSIDE LARGE VESSELS PROTECT THE VESSEL WALL FROM THERMAL DAMAGE DURING RF-ASSISTED SURGICAL RESECTION? A COMPUTER MODELING AND AN IN VIVO EXPERIMENTAL STUDY133

6.1. Abstract.....	133
6.2. Introduction.....	134
6.3. Materials and methods.....	136
6.3.1. <i>Description of the RF-assisted device</i>	136
6.3.2. <i>Computer modeling</i>	136
6.3.3. <i>Modeling blood flow</i>	140
6.3.3.a. <i>Method 1: constant h_v</i>	140
6.3.3.b. <i>Method 2: temperature-dependent h_v</i>	141
6.3.3.c. <i>Method 3: advection heat method</i>	142
6.3.4. <i>Comparison of blood flow models</i>	143
6.3.5. <i>Thermal modeling</i>	143
6.3.6. <i>Experimental setup</i>	144
6.4. Results.....	145
6.4.1. <i>Computer modeling</i>	145
6.4.2. <i>Comparison of blood flow models</i>	145
6.4.3. <i>Thermal modeling</i>	146
6.4.4. <i>Experimental validation</i>	148
6.5. Discussion.....	149
6.6. Conclusions.....	153

CHAPTER 7. THERMO-ELASTIC RESPONSE TO RF HEATING WITH THERMAL DAMAGE QUANTIFICATION OF SUBCUTANEOUS ADIPOSE TISSUE OF DIFFERENT FIBROUS SEPTA ARCHITECTURES: A COMPUTATIONAL MODELING STUDY.....165

7.1. Abstract.....	165
7.2. Introduction.....	166
7.3. Materials and methods.....	168
7.3.1. <i>Physical Situation</i>	168
7.3.2. <i>Governing Equations</i>	168

7.3.3. <i>Tissue Characteristics</i>	171
7.3.4. <i>Boundary and initial conditions</i>	171
7.4. Results.....	173
7.4.1. <i>Electric Response</i>	173
7.4.2. <i>Temperature Response and Damage Quantification</i>	173
7.4.3. <i>Thermo-elastic Response</i>	174
7.4.4. <i>Comparison with case of absence of fibrous septa</i>	175
7.5. Discussion.....	175
7.6. Conclusions.....	177
CHAPTER 8. GENERAL DISCUSSION	189
CHAPTER 9. CONCLUSIONS	193
REFERENCES	197
PUBLICATIONS	215
LIST OF FIGURES	219
LIST OF TABLES	224

List of Acronyms

2D	Two-dimensional
3D	Three-dimensional
AF	Atrial fibrillation
BM	Bipolar mode
DC	Direct-current
FEM	Finite Element Method
HIFU	High intensity focused ultrasound
IVS	Interventricular septum
LV	Left ventricle
MRI	Magnetic resonance imaging
MUMPS	Multifrontal massively parallel sparse
RF	Radiofrequency
RFA	Radiofrequency ablation
RV	Right ventricle
SEUM	Sequential unipolar mode
SIUM	Simultaneous unipolar mode
UM	Unipolar mode
VFW	Ventricular free wall
VT	Ventricular tachycardia

List of Symbols

A	Frequency factor, s^{-1}
c	Specific heat, $J/kg \cdot K$
C	Tissue water content, %
\mathbf{C}	Stiffness tensor
c_b	Heat capacity of blood, $J/Kg \cdot K$
\mathbf{E}	Vector electric field, V/m
E	Young's Modulus, Pa
\mathbf{F}_v	External volume forces, Pa/m^2
h	Enthalpy
h_{a-s}	Heat transfer coefficient in the air-skin, W/m^2K
$h_{CL} = h_{CR}$	Heat transfer coefficient in the –blood, W/m^2K
h_e	Free thermal transfer coefficient, W/m^2K
$h_{EL} = h_{ER}$	Heat transfer coefficient in the electrode–blood, W/m^2K
h_{EN-B}	Heat transfer coefficient in the endocardium–blood, W/m^2K
h_{EPI-A}	Heat transfer coefficient in the epicardium–ambient, W/m^2K
h_{fg}	Latent heat, J/m^3
h_i	Heat transfer coefficient inside the electrode, W/m^2K
h_v	Heat transfer coefficient at the tissue-vessel interface, W/m^2K
\mathbf{I}	Identity matrix
\mathbf{J}	Vector current density, A/m^2
k	Thermal conductivity, $W/m \cdot K$
Nu	Nusselt number, dimensionless
P	Power, W
Pr	Prandtl number, dimensionless
q	Heat source from RF power, W/m^3
Q_m	Metabolic heat generation, W/m^3

Q_p	Heat loss caused by blood perfusion, W/m^3
R	Universal gas constant, $8.314472 \text{ J/mol}\cdot\text{K}$
Re	Reynolds number, dimensionless
S	Duhamel term
T	Temperature, $^{\circ}\text{C}$
t	Time, s
T_b	Blood temperature, $^{\circ}\text{C}$
T_{\max}	Maximal temperature, $^{\circ}\text{C}$
u	Velocity of the flow, m/s
u_b	Blood velocity, m/s
Z	Electrical impedance, Ω
α	Thermal expansion coefficient, $1/^{\circ}\text{C}$
β	Arc of the vessel damage, $^{\circ}$
ΔE	Activation energy for the irreversible damage reaction, J/mol
ϵ	Strain tensor, dimensionless
ε	Permittivity, F/m
μ	Dynamic viscosity, $\text{N}\cdot\text{s/m}$
ρ	Mass density, kg/m^3
ρ_b	Density of blood, kg/m^3
σ	Electrical conductivity, S/m
σ	Stress tensor, Pa
Φ	Voltage, V
$\Omega(t)$	Degree of tissue injury
ν	Poisson's ratio, dimensionless
ω_b	Blood perfusion coefficient, s^{-1}

Chapter 1

Introduction

1.1. Background: Radiofrequency ablation (RFA)

The energy-based ablative techniques currently used in numerous medical-surgical areas employ different types of energy (laser, microwave, radiofrequency - RF- or ultrasound -HIFU-) to destroy or alter biological tissue for a particular therapeutic purpose. Although the use of RF currents for the surgical treatment of different diseases is relatively new, heat has been in use as a means of therapy for thousands of years. For example, the Ancient Greeks had their steam baths, the Mesoamericans their temascalí, the Chinese had herbal baths and the Ancient Egyptians used cauterization to stop bleeding and in other treatments, techniques that were later improved on by the Moors in the Iberian Peninsula (Berjano *et al* 2010).

The first breakthrough in tissue-heating technology came through the experiments with high frequency currents on the human body conducted by d'Arsonval in 1891. He observed that currents over 10 kHz did not produce any kind of nervous or muscular stimulation, but only a progressive heating. This finding was the starting point of current electrosurgery, which uses electric currents of sinusoidal waveform with frequencies in the range between 300 kHz and 1 MHz, known as *radiofrequency (RF) currents*.

In the early 20th century, Carl Franz Nagelschmidt repeated d'Arsonval's experiment in the treatment of lesions and malignant growths, and named the procedure *diathermy*. In 1928 Cushing and Bovie developed the first electrocautery

device (known as the *Bovie knife*) to stop bleeding, which is still today an essential tool in surgical practice. The current version has been improved in order to cut with a certain degree of hemostasis, coagulate small blood vessels, or achieve the carbonization of surface tissue (fulguration).

The term *RF ablation* (RFA) emerged in the mid 80s due to the rapid growth in the number of new (more or less invasive) surgical procedures that used RF currents, accompanied by new electrode designs and energy delivery protocols (Berjano *et al* 2010). RFA is a procedure in which RF energy is applied to biological tissue through electrodes and raises the local temperature to a point at which a thermal lesion is caused, but without implying the mechanical excision of a section of tissue.

1.1.1. RFA modes

An RFA procedure is performed with an RF generator serving as the primary component of an electrical circuit. The generator is the source of current in the circuit and the human body serves as a resistor (VanSonnenberg *et al* 2005). RF energy is transmitted to the body through two metal electrodes in contact with the tissue. The generator creates a voltage differential between both electrodes which is alternating, sinusoidal and with a fixed frequency of approximately 500 kHz. The electrical charge carriers inside the biological tissue are ions; whereas in the generator, the wires and electrodes are electrons. The charge is transferred between the two different types of carrier in the electrode-tissue interface. Due to the high frequency used in ablation, the electric field established by the electrodes changes its polarity every 2 μ s (1/500 kHz), which makes the displacement direction of the ions change fast enough to produce heat by ionic agitation, without any kind of electrical stimulation. The ionic agitation is most pronounced when the current density is highest, and consequently is where most heating occurs. The rest of the lesion is created by heat conduction (Berjano 2008). The absence of stimulation with alternating currents above 10 kHz was postulated by D'Arsonval (1891). Subsequently, Nerst (1908) postulated that the current required to produce

stimulation varies with the square root of frequency (Nerst Law), so that high frequencies would require tremendous intensities to produce stimulation.

As the behavior of RF current varies according to the position and dimensions of the two electrodes connected to the generator, both monopolar and bipolar arrangements are used in RF ablation (Figure 1.1).

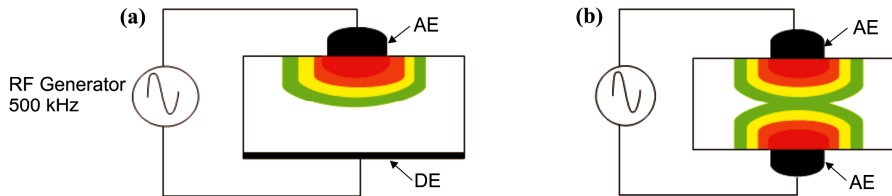


Figure 1.1. RFA using monopolar (a) and bipolar (b) arrangements. AE: active electrode and DE: dispersive electrode.

With a monopolar arrangement (Figure 1.1(a)), ablation is confined to a targeted volume of tissue by inserting an RF electrode connected to a generator directly into the tissue. The electrode tip (active electrode) is relatively small, and so the current density surrounding this tip is high, which creates a localized thermal effect due to ionic agitation. A return connection to the RF generator is required to complete the circuit. This return is established by placing a dispersive electrode in contact with the skin, usually on the patient's thigh. This grounding pad has a large surface area, keeping current density low to eliminate heating at the sites of contact (VanSonnenberg *et al* 2005). This configuration has the following limitations: the thermal lesions created have great depth, which results in excessive destruction of healthy tissue; RF currents can produce undesirable and dangerous thermal lesions to intermediate or distant organs, which is especially important when surgery is performed by a laparoscopic approach in conditions of reduced visibility (Wattiez *et al* 1995); and an adequately monitored dispersive electrode has to be used to ensure good electrode-skin contact to avoid skin burns.

The bipolar arrangement (Figure 1.1(b)) uses two identical (active) electrodes between which RF current flows. This arrangement requires less power

than the monopolar configuration to achieve the same coagulating effect and has the additional advantage of not needing a dispersive electrode, thus avoiding the risk of skin burns through poor skin/dispersive electrode contact. However, the most important advantage is that bipolar electrodes prevent RF currents flowing through adjacent tissue, thus minimizing the risk of injury to other organs.

1.1.2. Electrode design

RFA electrode designs are of two types, according to whether or not they have internal tip cooling: dry (non-irrigated) and cooled (irrigated) electrodes. Wittkamp *et al* (1988) were the first to suggest that irrigation of the catheter tip with saline could prevent excessive temperature rises and allow more power to be delivered to the tissue. Cooled electrodes avoid dehydration and carbonization of the tissue adjacent to the electrode when the temperature reaches approximately 100°C during RFA. This permits the RF current to continue flowing to deeper areas and achieve larger thermal lesions. However, dry electrodes tend to overheat the tissue adjacent to the electrode, which causes a sudden increase in electrical impedance to the point where the RF generator cannot deliver any more power and thus inhibits further ablation and lesion growth (Berjano 2008).

Two types of cooled electrode designs are commonly used in clinical RF heating at the present time (Latchamsetty and Oral 2012): closed-irrigated electrodes (Figure 1.2(a)), also known as internally-cooled electrodes, and open-irrigated electrodes (Figure 1.2(b)). The former type has a closed internal circuit through which circulates a cooling fluid (4-20°C) which never comes into contact with the tissue. In contrast, open-irrigated electrodes have perforations through which the cooled fluid is infused into the tissue. These two designs can be combined in a single RF (hybrid) applicator which has recently been proposed only for RF tumor ablation (Burdío *et al* 2007).

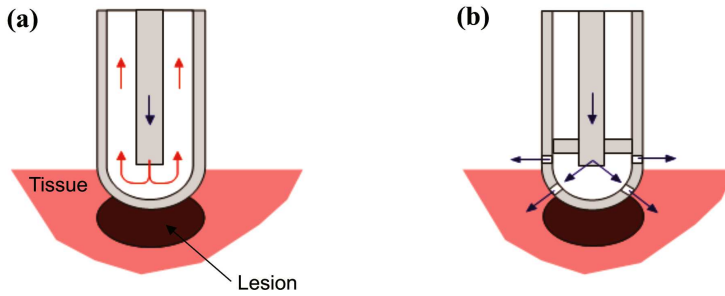


Figure 1.2. Cooled electrodes: (a) closed-irrigated electrode (or internally cooled electrode) and (b) open-irrigated electrode.

1.1.3. Clinical applications

The clinical applications of RF heating of biological tissue include diverse areas such as the destruction of liver tumors by using percutaneous electrodes guided by imaging techniques (Leen and Horgan 2007), RF-assisted resection of an organ affected by cancer (Burdío *et al* 2008), elimination of cardiac arrhythmias by RF catheter ablation (Blaauw and Crijns 2007), correction of hyperopia in refractive corneal surgery (Berjano *et al* 2007), treatment of gastroesophageal reflux (Spicák 2007), thermal remodeling of oral cavity tissue to cure sleep obstructive apnea (Steward 2004), therapeutic heating of articular cartilage (Yetkinler *et al* 2002), RF heating of cutaneous tissues to cause shrinkage of dermal collagen and induce stimulation of fibroblast cells to produce new collagen (Sadick and Makino 2004), and more recently, RF heating of subcutaneous tissues to induce irreversible thermal damage of adipose tissue (Franco *et al* 2009, 2010). In this section, we describe the background of each of the three clinical-surgical areas on which the Thesis is focused: RF cardiac ablation, RF-assisted hepatic resection and RF heating of subcutaneous adipose tissue.

1.1.3.a. RF cardiac ablation

The objective of RF cardiac ablation is the elimination of a cardiac arrhythmia, which is an electrical malfunction of a group of cardiac cells. The

correct electrical activity of these cells controls the beating of the heart and thus the pumping of blood around the body (Berjano *et al* 2010). The most frequent cardiac arrhythmia ablated by RF energy is atrial fibrillation, but there are other arrhythmias that can be treated by this method, such as ventricular tachycardia, atrial flutter, nodal reentry, or atrial ectopic tachycardia (focal).

The first case of cardiac arrhythmia ablation (surgery) was treated by high energy (fulguration) direct current (DC) in 1968 (Berjano 2008). Huang *et al* (1987) described ablation using alternating RF current through a percutaneous catheter. RF ablation by percutaneous catheter is now the dominant therapeutic method for a variety of arrhythmias (Berjano *et al* 2010). Figure 1.3 shows an overview of percutaneous cardiac ablation for treatment of a cardiac arrhythmia. A catheter with an ablation electrode on its tip is inserted into the heart (atrium or ventricle) through a vein or artery and is connected to an RF generator. The group of cells inside the heart responsible for the arrhythmia is located by means of electrophysiological mapping. RF currents are then applied through the ablative electrode (active electrode) and a large-area (dispersive) electrode attached to the patient's back (i.e. monopolar arrangement). The maximal electrical current density is achieved in the tissue in the immediate vicinity of the ablative electrode, raising the temperature in this zone, whereas farther away the tissue temperature is increased mainly by thermal conduction. The region heated above $\approx 50^{\circ}\text{C}$ becomes nonviable and defines the lesion volume, which must include the targeted region and extend as little as possible beyond it in order to be therapeutically effective (Panescu *et al* 1995b).

At present, percutaneous RFA uses catheter-coupled electrodes from 6Fr to 10Fr in diameter. Their ablation electrodes are usually between 4 and 10 mm long, with a semispherical tip which may have no irrigation or close/open irrigation (Berjano *et al* 2010, Latchamsetty and Oral 2012). Figure 1.4 shows a closed-irrigated catheter (7Fr, ablative electrode 8-mm in length) and an open-irrigated catheter (7Fr, ablative electrode 4-mm in length; 10 irrigation holds: 1 at the central tip, 3 at distal sites, 3 in the middle and 3 at proximal sites).

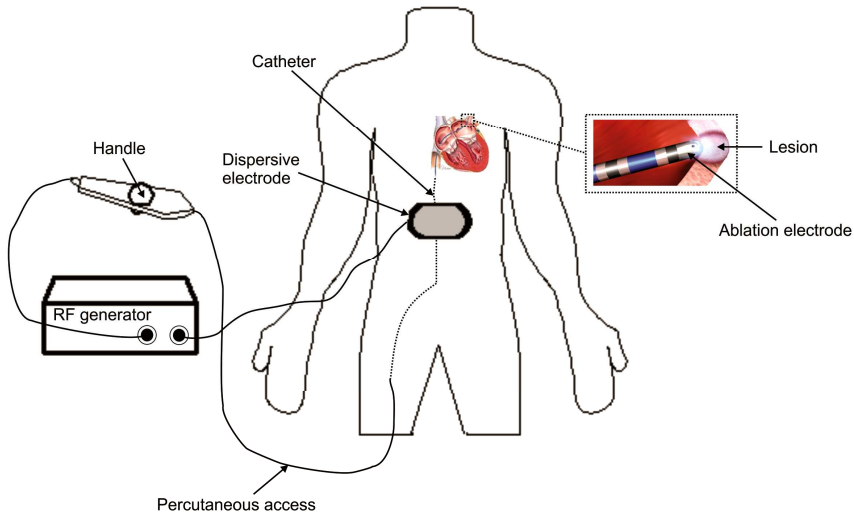


Figure 1.3. Overview of percutaneous cardiac ablation for treatment of a cardiac arrhythmia, which implies a disorder of the electrical activity of a group of cardiac cells. A catheter with an ablation electrode on its tip is inserted into the heart through a leg vein and connected to an RF generator. Once the tip of the catheter is inside the heart and the group of cells responsible for the arrhythmia is located, RF currents are applied through the ablative electrode (active electrode) and a large-area (dispersive) electrode attached to the patient's back.

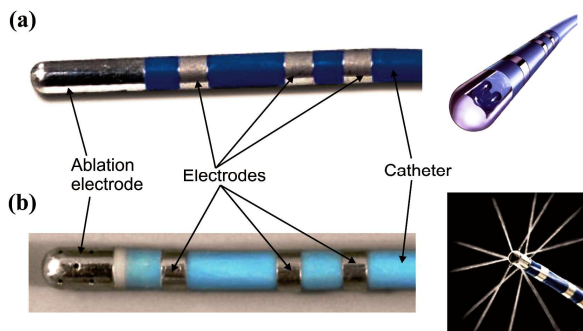


Figure 1.4. Multi-electrode catheter probes: (a) closed-irrigated-tip and (b) open-irrigated-tip catheter. Detail of the irrigation type on the tip of the catheters (right).

Cardiac arrhythmias can also be treated by surgical (intraoperative) RFA in two different ways: 1) ablation is performed without heart arrest (minimally invasive surgery through small incisions), producing lesions on the epicardium surface; or 2) with heart arrest (open-chest surgery through electrodes included in handheld devices), using a system of extracorporeal circulation and causing lesions on the internal surface of the heart (endocardium). Different monopolar and bipolar electrode designs are used for this type of surgery.

Two electrode designs are used for intraoperative RFA with a monopolar arrangement: multi-electrode handheld probes (Melo *et al* 2000, Pasic *et al* 2001), which are placed over the tissue during the RF energy delivery; and uni-electrode probes (pen applicators), which are dragged and slipped over the tissue surface simultaneously with the RF energy delivery (Figure 1.5). This arrangement has some limitations: lesions are shallow (i.e. probably nontransmural), especially in the epicardial approach, due to endocardial cooling by circulation of blood inside the atrium and anatomical factors such as overlying epicardial fat (Berjano and Hornero 2004) or fibrosis caused by adhesion (Santiago *et al* 2003a); it may also cause damage to nearby coronary arteries, strokes and fistula in the esophagus (Berjano and Hornero 2005a, 2005b).



Figure 1.5. Uni-electrode probes: Cardioblate[®] monopolar pens (Medtronic, Minneapolis, MN, USA).

Electrosurgical forceps are also used in intraoperative RFA with a bipolar arrangement (Voeller *et al* 2010). These have long electrodes that allow elongated and continuous lesions to be created without gaps, as is required when treating atrial fibrillation. Figure 1.6 shows two forcep designs for intraoperative cardiac ablation: the Cardioblade BP (Medtronic, Minneapolis, MN, USA) which is an open-irrigated device, and the closed-irrigated device Isolator (AtriCure, Cincinnati, OH, USA). Using this configuration, there have been no complications with the monopolar arrangement and in addition the lesions are more transmural since they are limited to the tissue between the two electrodes.

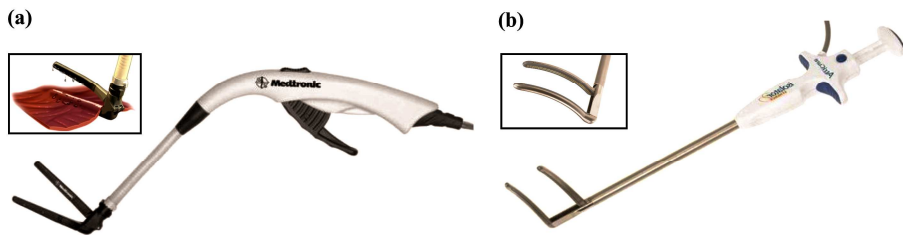


Figure 1.6. Electro-surgical forceps for RF bipolar cardiac ablation: (a) open-irrigated (Cardioblade BP[®]) and (b) closed-irrigated (Isolator[®]) forceps.

The RFA of cardiac arrhythmias, either by percutaneous (catheter ablation) or cardiac surgery (intraoperative ablation) has been a well-established clinical procedure in the last 20 years. However, there are still many unknowns in some of the electro-thermal processes involved in RF heating of cardiac tissue. This lack of knowledge is reflected in the current dearth of techniques and devices capable of performing ablations quickly and safely under certain conditions. For example, there are currently no devices capable of giving easy access to atrial tissue and automatically creating continuous transmural lesions in areas with overlying fatty tissue (Kiser *et al* 2007). Our interest is therefore focused on developing new systems for intraoperative RFA of atrial fibrillation by an epicardial (minimally invasive) approach, as will be discussed in Chapters 2 and 3. There is also uncertainty as to the most effective ablation mode (bipolar, sequential unipolar and

simultaneous unipolar mode) in terms of achieving transmural lesions across the ventricular wall to eliminate ventricular tachycardias. This issue will be dealt with in Chapter 4. In short, the successful solution of these questions could lead not only to the development of new medical and surgical devices, but also to a more rational and safer use of the currently available clinical techniques.

1.1.3.b. RF-assisted hepatic resection

Most liver tumors are secondary (i.e. derived from a primary cancer of the colon, pancreas, lymphoma, prostate, bladder or lung) and some may undergo specific surgery called *resection* (or transection), a procedure that aims to mechanically remove the tissue fragment including the tumor (see Figure 1.7).

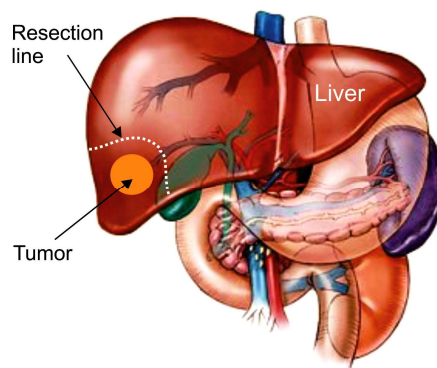


Figure 1.7. Liver with tumor showing the resection line on removing the tissue fragment containing the tumor.

The main drawback of the techniques presently used in hepatic resection is the excessive blood loss they involve (between 200 and 500 mL), resulting in perioperative complications, high rate of tumor recurrence and low rate of patient survival. The increase in transection time has also been associated with higher morbidity and mortality (Sitzmann and Greene 1994, Stephenson *et al* 1988). It is therefore necessary to design new surgical devices capable of reducing bleeding and transection times, since they are determinants of the operative outcome (Takayama *et al* 2001).

Some of the latest methods use RF heating to thermally coagulate the tissue prior to conducting the resection and thus minimize intraoperative blood loss. The rationale is to create sufficiently deep thermal lesions that will seal the small vessels in the transection plane (Poon *et al* 2005). Weber *et al* (2002) were the first to describe the concept of pre-coagulating the tissue prior to transection in order to reduce the associated bleeding. To do this, they used RF tumor ablation electrodes (Cooltip[®] RF devices) to achieve a coagulation area with a peripheral width around the tumor of about 1-2 cm, subsequently transecting the coagulated tissue with a simple scalpel.

This surgical method has led to the development of new devices such as Habib 4X (RITA Medical Systems Inc, Fremont, CA, USA) (Avay *et al* 2008) and In-line (Resect Medical, Fremont, CA, USA) (Yao and Morris 2006), based on a number of needles inserted into the theoretical resection line in order to create a barrier of coagulated tissue. The coagulated line is then transected using a cold scalpel (see Figure 1.8). The main problem is that these devices are not able to coagulate large vessels, so it is not known whether the coagulation has been complete. In fact, cutting the tissue may itself dissect one of these vessels and cause substantial blood loss.

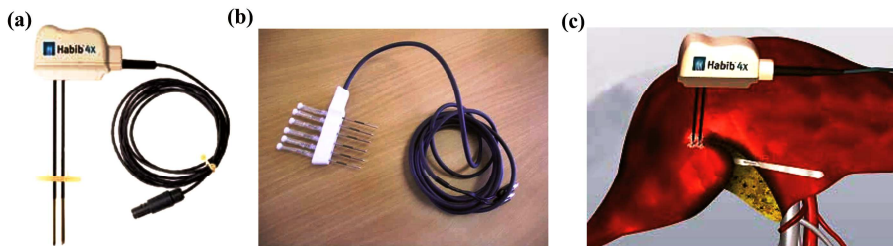


Figure 1.8. (a) Habib[®] 4X multiprobe bipolar RF device, (b) In-line[®] RFA device, and (c) process used to achieve a hepatic resection with these systems.

Another device used to coagulate liver tissue by RF energy is Ligasure (Covidien, Mansfield, MA, USA) (see Figure 1.9), which is based on a clamp system (i.e. bipolar arrangement) and allows sealing blood vessels up to 7 mm (Poon

et al 2005). The latest models (Ligasure Atlas[®]) incorporate a cutting system to be used after sealing.

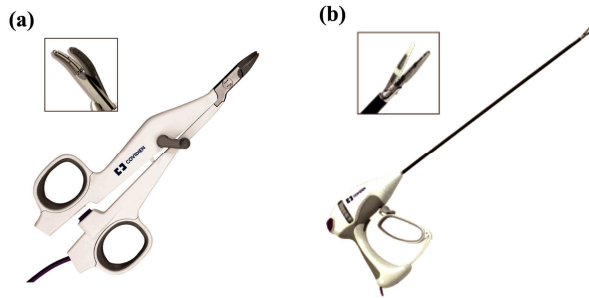


Figure 1.9. Ligasure[®] bipolar RF device for open (a) and laparoscopic surgery (b).

One of the most frequently used devices in RF-assisted hepatic resection is Tissuelink (Salient Surgical Technologies, Portsmouth, NH, USA) (Poon *et al* 2005, Arita *et al* 2005). This is a monopolar device with open irrigation (also known as saline-linked), i.e. it has perforations in the tip through which a continuous drip of cooled saline is infused into the tissue (see Figure 1.10) to prevent surface charring by maintaining the tissue surface below 100°C (Topp *et al* 2004). The main advantages of this device are the reduction of bleeding during resection and a faster transection time (Poon *et al* 2005). However, it has several disadvantages: firstly, it can cause scalding of liver parenchyma, which would make it difficult to identify blood vessels or the main hepatic ducts and therefore increases the chance of hilar injury during liver transection (Arita *et al* 2005). Secondly, there is a potential risk of burning contiguous organs with the hot saline and the saline flow rate is critical to producing the desired haemostatic effect without excessive charring (Sprunger and Herrell 2005).



Figure 1.10. Tissuelink[®] dissecting sealer for RF-assisted hepatic resection. Detail of saline drip at the tip of the device (right).

In order to solve the above problems, Burdío *et al* developed the Coolinside device (Apeiron Medical, Valencia, Spain) for RF-assisted hepatic resection (Figure 1.11), which is based on a monopolar arrangement with closed irrigation (also known as internally cooled). They compared its performance with TissueLink, observing less blood loss during resection and faster transection times (Burdío *et al* 2008, 2009). However, some aspects of its performance need further study in order to optimize the technique and achieve safer and more efficient resections. This includes characterizing its electro-thermal behavior in a bipolar arrangement and assessing its impact in the proximity of large vessels, i.e. when resecting large liver fragments (greater hepatectomy). These are some of the issues that will be developed in depth in Chapters 5 and 6 of this PhD Thesis.

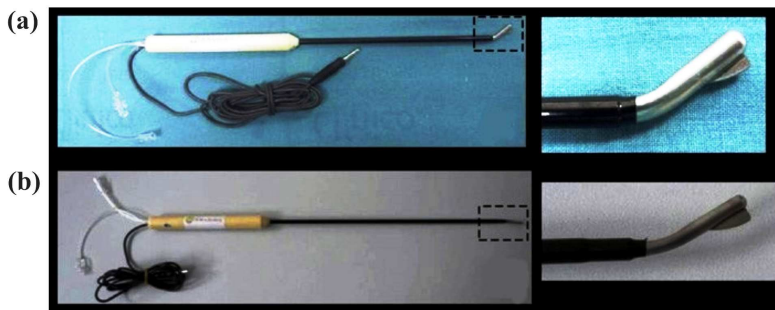


Figure 1.11. Coolinside[®] RF monopolar device for open (a) and laparoscopic surgery (b).

1.1.3.c. RF heating of subcutaneous adipose tissue

There has recently been increased interest in using RF currents in a non-invasive technique for selective heating of subcutaneous adipose tissue (Franco *et al* 2009, 2010). Unlike other clinical areas, the heating of cutaneous and subcutaneous tissues is not straightforward, since the RF device is in contact with non homogeneous tissues, resulting in more complex physical interactions between RF currents and tissue. Subcutaneous tissue (also known as hypodermis) morphology consists of a fine, collagenous and fibrous septa network enveloping clusters of adipocyte cells (see Figure 1.12). Furthermore, the density and orientation of fibrous

septa within subcutaneous tissue may vary from person to person. These variations are linked to different cellulite grades, which correlate with the percentile of adipose tissue versus connective tissue in a given volume of hypodermis and invaginations inside the dermis. Cellulite Grade is assessed by visual inspection according to skin appearance and scaled in appearance from Grade 0, smooth skin, to Grade 4 “cottage cheese” (Mirrashed *et al* 2004).

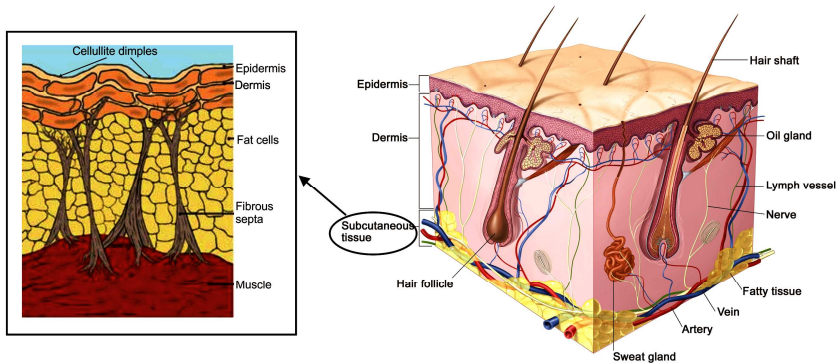


Figure 1.12. The skin-fat structure composed of three layers: epidermis, dermis and subcutaneous tissue. The subcutaneous tissue consists of a fine, collagenous and fibrous septa network enveloping clusters of fat cells.

There are many different fat-related disorders (such as, lipomatosis, Madelung’s disease, lipomatosis, lipedema, or cellulite) including excess volume of fat lobules due to local distribution or obesity, thinning and vertical arrangement of fibrous septa due to cellulite, inflammatory conditions and benign fat tumors. Cellulite is not only a problem due to fat accumulation, but is also caused by changes in the structural septa configuration (Jimenez Lozano *et al* 2013). The goal of clinical treatment is to heat tissue up to a certain temperature and keep it there long enough to cause adipocyte cellular damage while sparing overlying and underlying tissues. Franco *et al* (2009, 2010) demonstrated that adipocytes were heat sensitive to 50°C for 1 min and 42–45°C for 15 min thermal exposures, which resulted in delayed cellular death response. In this regard, the fat heats up much more than the skin and muscle when an RF applicator creates an electric field

perpendicular to the skin–fat and fat–muscle interfaces. However, when the electric field is not normal to the tissue surface, the opposite occurs, the skin heats up more than the fat. In this case the heat is used to contract collagen fibers, at the same time stimulating the generation of new collagen inside the dermis, thus creating softer and firmer skin (Sadick 2008).

Franco *et al* (2009, 2010) developed a novel RF device (Cutera, Inc., Brisbane, CA) to induce lethal thermal damage to adipose tissue while maintaining skin and muscle tissues at safe temperatures by establishing a controlled electric field perpendicular to the skin-fat and fat-muscle interfaces. This applicator is based on a monopolar arrangement and consists of a multidimensional series of tightly spaced concentric rings that are energized at variable operational frequencies in order to control the volume of the heated subcutaneous tissue and hence the depth of heating (see Figure 1.13). In this regard, high frequencies are appropriate for treatment of smaller subcutaneous tissue areas while low frequencies are appropriate for larger areas. This design also has the ability to provide uniform tissue heating across the entire surface of the applicator by controlling the distribution of the surface electric potential. Simply changing this distribution varies the extent of the uniform heating and consequently the volume of heated tissue.



Figure 1.13. RF monopolar applicator which consists of a multidimensional series of tightly spaced concentric rings. Detail of the concentric rings geometry (right).

Body contouring has now become one of the most exciting areas in today's aesthetic medicine and surgery, for which Paul and Mulholland (2009) introduced the radiofrequency-assisted liposuction (RFAL) technique. This technique delivers RF energy to heat deep subcutaneous adipose tissue to much higher temperatures without compromising skin safety in order to achieve reduction of subcutaneous tissue with simultaneous tissue contraction. It presents the following apparent advantages with respect to the traditional suction-assisted liposuction as well as other energy liposuction methods, such as power-assisted liposuction (PAL), ultrasound-assisted liposuction (UAL) and laser-assisted liposuction (LAL): faster treatment, reduced tissue trauma, ability to uniformly heat larger volumes of subcutaneous tissue, defragmentation of fat cells and coagulation of blood vessels in the treated zone reducing bleeding and bruising, collagen denaturation after RFAL treatment, and significant contraction and retraction of adipose and dermal tissue after treatment.

Paul and Mulholland (2009) developed the BodyTite™ system (Invasix Ltd, Yokneam, Israel) for body contouring by RFAL. This device uses an external and internal electrode connected by a handpiece (i.e. bipolar arrangement) to deliver RF energy to the adipose tissue and skin (see Figure 1.14(a)). The internal electrode (cannula) is coated with dielectric material and is inserted into the pretumesced fat to be contoured and is moved gently back and forth at various predetermined and controlled depths for uniform heating of the treated volume. This electrode emits the RF current through a small conductive tip. The external electrode has a larger contact area and is moved along the surface of the skin in tandem vertical alignment with the internal cannula tip. The RF energy flows between the internal cannula tip and the external electrode and coagulates tissue in the vicinity of the internal cannula tip and gently heats the dermis below the external electrode (Figure 1.14(b)). In addition to emitting energy, the internal electrode also serves as a suction cannula to provide simultaneous aspiration of the coagulated tissues and allows the surgeon to perform the desired contouring (Paul *et al* 2011). The latest device (CelluTite™) uses the BodyTite system with an internal V-dissector tip (Figure 1.14(a)) to target

moderate and severe lumpy deposits of subcutaneous fat and vertical fibrous septa to flatten the pockets of cellulite and restore a smooth skin surface.

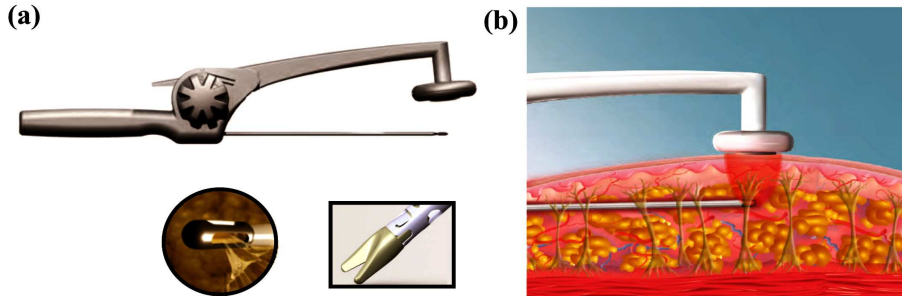


Figure 1.14. (a) Bipolar RF handpiece with the aspirating cannula: cannula for BodyTite system (left) and V-dissector tip for CelluTite system (right). (b) RFAL handpiece inserted into the body with directional energy applied to adipose fat and fibrous septa.

At the present time there is still a lack of understanding of the qualitative and quantitative features of the physical thermo-elastic mechanism of dermal RF heating in the presence of fibrous septa networks between fat lobules. Information on the thermo-elastic response of cutaneous and subcutaneous tissues (including the fibrous septa network), such as the thermal denaturation mechanism of collagen (thermal shrinkage) during RF heating, would be useful for the development of new devices/products and improving existing devices/products/treatments in clinical and cosmetic applications. These are some of the issues that will be developed in depth in Chapter 7.

1.2. Objectives and Organization

The main purpose of this PhD Thesis is to gain a better understanding of the electrical and thermal phenomena involved in the heating of biological tissues by radiofrequency (RF) electrical currents, in order to improve the efficacy and safety of current clinical techniques such as cardiac surgery, oncology and dermatology.

An additional aim is to suggest technical improvements in the design of RF energy applicators. These aims involved the following general and specific objectives:

1. To study techniques for improving **RF cardiac ablation** using an epicardial, endocardial-endocardial and endocardial-epicardial approach.
 - 1.1. To study the effect of different procedural and anatomical factors on transmural lesions in atrial tissue during epicardial RF ablation (RFA).
 - 1.2. To conduct a proof-of-concept of a new probe for assessing the amount of epicardial fat present prior to RFA.
 - 1.3. To study the effect of different modes of RF cardiac ablation on transmural lesions in the ventricular wall by a pair of catheters placed on opposite sides of the wall.
2. To investigate the electrical and thermal behaviour of the applicators currently used in **RF-assisted hepatic resection**.
 - 2.1. To study the electro-thermal behaviour of an internally cooled bipolar applicator for RF-assisted hepatic resection.
 - 2.2. To study the heat sink effect inside a large vessel close to an internally-cooled electrode during RF-assisted hepatic resection.
3. To investigate the electrical, thermal and thermo-elastic performance of subcutaneous tissue structures in order to improve the treatment by **RF heating of subcutaneous adipose tissue** related disorders.
 - 3.1. To study the electrical, thermal and thermo-elastic effect of two different structures of fibrous septa within subcutaneous tissue during RF hyperthermic heating.

This document is arranged as follows:

Chapter 2 covers Objective 1.1 and presents a two-dimensional mathematical model for epicardial RFA, which is used to study the capability of different electrode designs and protocols for delivering RF power to ablate atrial tissue in the presence of epicardial fat. This chapter is an improved version of the

manuscript previously published in *The Open Biomedical Engineering Journal* (González-Suárez *et al* 2010a).

Chapter 3 covers Objective 1.2 and presents a three-dimensional model used to assess a new technique based on bioimpedance measurements using a multi-electrode probe to estimate the quantity of overlying epicardial fat prior to RF cardiac ablation. This chapter is an improved version of the manuscript previously published in *Physiological Measurement* (González-Suárez *et al* 2010b).

Chapter 4, which covers Objective 1.3, presents the two and three-dimensional models used to study temperature distributions and lesion dimensions on the interventricular septum (endocardial-endocardial approach) and ventricular free wall (endocardial-epicardial approach) using different modes of radiofrequency ablation. These models are also used to study the effect of ventricular wall thickness, catheter misalignment and the accidental presence of air in the epicardial space. This work has been submitted to *The International Journal of Hyperthermia*.

Chapter 5, which covers Objective 2.1, presents a two-dimensional model of a closed-irrigated bipolar RF applicator used to check the applicator's electrical-thermal performance and its capacity to create sufficiently deep thermal lesions in hepatic tissue. The computer results were validated with *ex vivo* and *in vivo* studies. Additional computer simulations modeled the *in vivo* scenario and were conducted to study the effect of the applied voltage and duration on lesion depth and to determine the potential of the cooled bipolar applicator to coagulate hepatic tissue. These simulations were extended to the case of a smaller applicator especially designed for laparoscopic use. This chapter is an improved version of the manuscript previously published in *The International Journal of Hyperthermia* (González-Suárez *et al* 2012).

Chapter 6, which covers Objective 2.2, presents the three-dimensional models used to study temperature distributions and thermal lesion dimensions in hepatic tissue around a large vessel coagulated by RF energy with an internally-cooled applicator at different positions and distances from the vessel. The computational results were validated by *in vivo* experiments. The manuscript of this chapter has been submitted to *Medical Physics*.

Chapter 7, which covers Objective 3.1, presents two-dimensional models of skin, subcutaneous tissue and muscle. The modeling of the subcutaneous tissue includes two realistic structures of fibrous septa. These models are used to assess the electrical and thermo-elastic performance of the two subcutaneous tissue structures during RF heating, as well as to quantify the thermal damage in both subcutaneous tissue structures after heating. This chapter is a preliminary manuscript that will be submitted to *Lasers in Surgery and Medicine*.

Chapter 8 contains a general discussion and also suggests future lines of research. The conclusions of the Thesis are given in Chapter 9.

Chapter 2

Mathematical Modeling of Epicardial RF Ablation of Atrial Tissue with Overlying Epicardial Fat

2.1. Abstract

The efficacy of treating atrial fibrillation by RF ablation on the epicardial surface is currently under question due to the presence of epicardial adipose tissue interposed between the ablation electrode and target site (atrial wall). The problem is probably caused by the electrical conductivity of the fat (0.02 S/m) being lower than that of the atrial tissue (0.4-0.6 S/m). Since our objective is to improve epicardial RF ablation techniques, we planned a study based on a two-dimensional mathematical model including an active electrode, a fragment of epicardial fat over a fragment of atrial tissue, and a section of atrium with circulating blood. Different procedures for applying RF power were studied, such as varying the frequency, using a cooled instead of a dry electrode, and different modes of controlling RF power (constant current, temperature and voltage) for different values of epicardial fat thickness. In general, the results showed that the epicardial fat layer seriously impedes the passage of RF current, thus reducing the effectiveness of atrial wall RF ablation.

2.2. Introduction

Radiofrequency (RF) currents have been employed in many surgical and therapeutic procedures, such as atrial fibrillation (AF), a common arrhythmia and a significant public health problem for its clinical prevalence and morbid-mortality. The prevalence of AF increases with age and reaches almost 5% of the population over 69 and 8% of those over 80 (Kannel *et al* 1998). Data from the Framingham heart study show that AF is associated with a 1.5 to 1.9-fold higher death risk and may be associated with thromboembolic stroke (Benjamin *et al* 1994, Wolf *et al* 1991).

A nonsurgical approach based on a percutaneous catheter was initially considered to create the desired lesion pattern in atrial tissue for treating AF (Haïssaguerre *et al* 1994). At present, the use of both percutaneous (via catheter) and surgical (intraoperative) RF ablation to treat AF is increasing, in spite of the lack of knowledge of the mechanisms involved. The atrial myocardium needs to be ablated in order to restore sinus rhythm. The effectiveness of surgical ablation in this intervention is 70-80% independent of the kind of energy used (Khargi *et al* 2005, Cox *et al* 1996, Nakajima *et al* 2002). Early post-ablation recurrence of the arrhythmia probably depends on lesion transmuralty (Miyagi *et al* 2009), and the existence of epicardial fat (Berjano and Hornero 2004). Histological analysis of surgical lesions has shown 25-30% non transmural lesions (Santiago *et al* 2003a, 2003b, Deneke *et al* 2005).

The efficacy of standard RF ablation on the epicardial surface is uncertain due to the varying presence of epicardial adipose tissue interposed between the ablation electrode and target site, i.e. the atrial wall (see Figure 2.1) (Hong *et al* 2007, Thomas *et al* 2003). This is probably caused by the electrical conductivity of the fat (0.02 S/m) being lower than that of atrial tissue (0.4-0.6 S/m).

In order to achieve optimum epicardial ablation of atrial tissue under a layer of fat, different types of energy are currently being researched, such as high intensity focused ultrasound (HIFU) (Mitnovetski *et al* 2009), microwave (Pruitt *et al* 2007), laser (Hong *et al* 2007) and cryoablation (Ba *et al* 2008). As we considered that this issue has not been sufficiently studied, we designed a computer modeling study of

the effect of different electrode designs and protocols for delivering RF power (Berjano 2006) to assess the capacity of different techniques to ablate atrial tissue in the presence of epicardial fat. We first studied the effect of using different frequencies with a standard 4 mm 7-Fr electrode. A previous experimental study had reported that a frequency of 2 MHz resulted in a 22% increase in lesion depth when compared to a frequency of 100 kHz (Koovor *et al* 1996). We then assessed the effect of the RF ablation mode (voltage, current and temperature constant). Finally, taking into account that previous experimental studies have shown that an internally cooled electrode (also known as a cooled-tip electrode) can generate epicardial lesions more efficiently than standard electrodes in zones with overlying epicardial fat (d'Avila *et al* 2004), we also included this kind of electrode in the study.

2.3. Methods

2.3.1. Description of the theoretical model

Although different RF electrode geometries have been proposed for epicardial RF ablation of atrial tissue (Thomas *et al* 2003, Raman *et al* 2002), we simplified the physical situation of the study by using a 4 mm long active electrode with a 3-mm-diameter hemispherical tip. The electrode contacted the tissue at an angle of 90° and hence presented axisymmetric characteristics and a two-dimensional approach could be used. Figure 2.2 shows the proposed theoretical model, which shows the active (stainless steel) electrode with a section of plastic (polyurethane) probe, a fragment of epicardial fat over a fragment of atrial tissue, and a section of atrium with circulating blood. The active electrode is inserted in the fat layer to a depth of 1.5 mm (corresponding to the electrode radius). The value of the model parameters Z and R were calculated by means of a sensitivity analysis in order to avoid boundary effects.

2.3.2. Governing equations

Temperature (T) in the tissue was obtained by solving the *Bioheat Equation*, which governs thermal phenomena during therapeutic heating of biological tissues:

$$\rho c \frac{\partial T}{\partial t} = \nabla \cdot (k \nabla T) + q - Q_p + Q_m \quad (1)$$

where ρ , c and k are respectively the density, specific heat and thermal conductivity of the tissue. The term Q_p corresponds with the heat loss caused by blood perfusion; and Q_m models the metabolic heat generation. This last term is always ignored in RF ablation modeling since it has been shown to be insignificant. It has also been shown that the Q_p term can be ignored in the case of cardiac ablation (Haines and Watson 1989). Finally, q is the heat source generated by RF power. In RF ablation, this term is related with electrical power density P (W/m^3), which is in general a complex number given by (Pearce 1986):

$$P = (\sigma + j\omega\varepsilon) |\mathbf{E}|^2 \quad (2)$$

where σ is electrical conductivity (S/m), ε is permittivity (F/m), and $|\mathbf{E}|$ is the magnitude of the vector electric field (V/m). The value of this vector is evaluated from $\mathbf{E} = -\nabla\Phi$ where Φ is the voltage (V). The voltage is obtained by using Laplace's equation:

$$\nabla \cdot (\sigma \nabla \Phi) = 0 \quad (3)$$

Only the real part of power density, i.e. $\text{Re}\{P\}$ contributes to the heating of the tissue, i.e. $\text{Re}\{P\} = q$. However, the permittivity has in fact a real (non-dissipative) and an imaginary (dissipative) part, i.e. $\varepsilon = \varepsilon' - j\varepsilon''$. Consequently:

$$q = \text{Re}\{P\} = (\sigma + \omega\varepsilon'') |\mathbf{E}|^2 \quad (4)$$

where ω is angular frequency (s^{-1}). The term $\sigma |\mathbf{E}|^2$ represents the heat resulting from dissipation due to convection currents (translational motion of ions), while the term $\omega\varepsilon'' |\mathbf{E}|^2$ represents the heat from dissipation due to irreversible rotation and vibration of bound charge carriers (Pearce 1986).

At the ablation frequencies considered in this study (100–10,000 kHz) and over the distance of interest (electrical power is deposited within a small radius around the active electrode) the biological medium can be considered totally resistive since the displacement currents can be neglected. A quasistatic approach was therefore possible to solve the electrical problem (Doss 1982).

The ANSYS program (ANSYS, Canonsburg, PA, USA) was used for the creation of Finite Element Models (FEM) and for solving the above equations by computer simulations. We used the PLANE67 elements (linear isoparametric type), which allow the coupled thermal-electric problem to be solved, where the electrical problem involves a DC (direct-current) problem. This means that the electrical variables in the model (voltage and current) are DC values, and hence they correspond with the root-mean-square value of the RF signal.

2.3.3. Characteristics of model elements

Table 2.1 shows the thermal and electrical characteristics of the model elements. In order to model the use of different frequencies, we considered the values of electrical conductivity reported in the literature for three frequencies: 100 kHz, 1 MHz, and 10 MHz. Although a previous modeling study on hepatic RF ablation considered a frequency value of 10 kHz (Haemmerich and Wood 2006), this value is too low for RF cardiac ablation, due to the possibility of electrical stimulation. In fact, in an experimental study, a 20 kHz current induced ventricular fibrillation (Koovor *et al* 1996). Since no difference between σ and ϵ'' is made in the literature, we assume that the value of reported electrical conductivity includes both mentioned phenomena, and hence corresponds with an effective value $\sigma_{effective} = \sigma + \omega\epsilon''$. In addition, we considered a change of +2%/°C. The values shown in Table 2.1 are effective values (Berjano and Hornero 2004, Gabriel *et al* 1996). In order to assess the effect of the epicardial fat layer on each ablation mode and electrode design, our study considered four values of fat thickness between 2 and 5 mm. The thickness of the atrial wall was considered to be fixed at 3 mm.

2.3.4. Boundary and initial conditions

In all FEM problems the boundary conditions must be defined. Regarding the electrical boundary conditions, null electrical current (Neumann boundary condition) was used at the symmetry axis, and also on the tissue-ambient and device-ambient interfaces. The electrical boundary conditions on the active and dispersive electrodes depend on the ablation mode considered and hence are described in the following section.

Regarding thermal boundary conditions, null thermal flux was used at the symmetry axis (Neumann boundary condition). The temperature values of surfaces at a distance from the active electrode were fixed by using Dirichlet boundary conditions. We assumed a value of 20°C in the upper limit of the probe and 36°C on the dispersive electrodes (see Figure 2.2).

The effect of free thermal convection in the epicardium-ambient and electrode-ambient interfaces was taken into account using a boundary thermal condition based on Newton's cooling law, which uses a convective heat transfer coefficient (h_{EPI-A}) of 20 W/m²K. The ambient temperature was considered to be 21°C. The effect of forced heat convection in the endocardium-blood was likewise taken into account using a thermal transfer coefficient (h_{EN-B}) of 1770 W/m²K (Schutt *et al* 2009). The blood circulating inside the atrium was considered to be at 36°C. The initial temperature was 36°C for the entire model.

2.3.5. Construction of the numerical model

The dimensions R and Z (see Figure 2.2) were calculated by means of a sensitivity analysis in order to avoid boundary effects. A convergence test was performed to obtain the adequate spatial and temporal resolution. The value of the maximal temperature achieved in the tissue (T_{max}) after 60 s of RF heating was used as a control parameter in these sensitivity and convergence tests.

Spatial resolution was heterogeneous. We used the criterion that the finest zone was always the electrode-tissue interface, since it is known that this zone has the largest voltage gradient and hence the maximum current density value. In the

tissue, grid size was increased gradually with distance from the interface. A tentative spatial and temporal resolution was considered first. We then conducted a computer analysis to determine the appropriate values of R and Z (see Figure 2.2). These simulations were made by increasing the value of the three parameters by equal amounts. When there was a difference of less than 0.5% between T_{\max} and the same parameter in the previous simulation, we considered the former values to be adequate. Finally, we performed convergence tests to determine adequate spatial and temporal resolution. Spatial resolution was achieved by refining the mesh near the blade so that T_{\max} was within 0.5% of the value obtained from the previous refinement step. With an adequate spatial resolution achieved, we decreased the time step until T_{\max} was within 0.5% of the value obtained from the last time step.

RF power was chosen for the study in order to avoid T_{\max} going above 100°C, since no experimental data have been reported dealing with the thermal and electrical characteristics of tissue above this temperature. We then analyzed the voltage and temperature distributions in the tissue using the 50°C isotherm as thermal lesion boundary.

2.3.6. Modeling the RF ablation mode

Three modes of delivering RF power were considered: constant voltage, current and temperature. All the simulations lasted for 60 s. In the constant voltage mode, the electrical potential was fixed on the active electrode a value of 30 V (root-mean-square value of the RF applied voltage), while the potential in the dispersive electrode was fixed at zero volts. In the constant current mode, a current of 12 mA was injected into a node of the active, and the same value was drained from a node on the dispersive electrode. Finally, in the constant temperature mode, the value of the electrical voltage on the active electrode was modulated during heating in order to maintain the center of the active electrode at a temperature of $70\pm 2^\circ\text{C}$ (sampled each 5 s). This was done by means of a trial-and-error method such as employed by Jain and Wolf (1999).

2.3.7. Modeling the ablation with a cooled electrode

Thermal cooling by the saline circulating (coolant) inside the electrode tip was modeled by means of a boundary thermal condition based on Newton's cooling law, and by considering a pre-cooling period, i.e. a previous period without applying RF power, as is employed clinically (d'Avila *et al* 2004). Previous modeling studies on RF cardiac ablation with cooled electrodes had set surface temperature at the coolant temperature (i.e. Dirichlet boundary condition) (Jain *et al* 1995, Panescu *et al* 1995a). However, recent results have suggested that the modeling of RF cooled electrodes should consider a boundary condition based on Newton's cooling law rather than a Dirichlet condition (Rivera *et al* 2009). Since the objective of our study was not to assess the effect of the flow rate of the coolant, we assumed a fixed value of $2000 \text{ W/m}^2\text{K}$ and a coolant temperature value of 20°C . In the cooled electrode, we modeled a constant voltage ablation by using the above described electrical boundary conditions.

2.4. Results

2.4.1. Construction of the model

Optimum outer dimensions were $R = Z = 30 \text{ mm}$. The convergence test provided a grid size of 0.075 mm in the finest zone (fat-active electrode interface), and a step time of 0.5 s during the first 10 s and 1 s for the remaining time. We also checked the grid size away from the electrode. The finite-element model had nearly 4042 nodes and used over 7754 triangular elements.

2.4.2. Effect of frequency for the dry electrode case

Tables 2.2 to 2.4 show the results of the computer simulations for the dry electrode and for three modes of controlling RF power (constant voltage, temperature and current) when frequency is changed between 100 kHz and 10 MHz . In the case of constant voltage (see Table 2.2), we observed that the increase of frequency involved higher T_{max} . Moreover, this behavior was more noticeable for a thinner atrial wall: T_{max} increased from 76.91 to 92.59°C when frequency augmented

from 100 kHz to 10 MHz for the case of a 2 mm thin fat layer, while it increased from 57.77 to 63.19°C for the same frequency augmentation in the presence of a 5 mm thick fat layer. Unfortunately, this increase in T_{\max} did not involve a significant increase in lesion depth. For instance, the percentage of ablated atrial wall increased from 39.20% to 48.77% when frequency increased from 100 kHz to 10 MHz (with 2 mm of fat). With thicker epicardial fat layers (4-5 mm), ablation of the atrial wall was not possible. In fact, at a constant voltage, increasing fat thickness involved a decrease in T_{\max} and in the depth of the lesion in the atrial wall (see Figure 2.3A). In the simulations using constant temperature (see Table 2.3), the results show that increasing frequency hardly involves any variation in either lesion depth in the atrial wall or T_{\max} . In fact, the tiny differences reported in Table 2.3 were probably due to the trial-and-error method employed to simulate the constant temperature protocol of $70\pm 2^\circ\text{C}$ at the electrode tip. Figure 2.3B shows (for 100 kHz) that even though fat thickness is increased, the temperature distribution remains unaltered, and hence the percentage of ablated atrial tissue is lower for thicker fat layers. Finally, the constant current ablation showed that changing frequency did not affect T_{\max} (see Table 2.4). However, a very interesting thermal performance was observed regarding the variation of fat thickness: augmenting fat thickness was directly related to an increase of T_{\max} from ≈ 70 to 82°C (see Figure 2.3C). On the other hand, lesion depth in the atrial wall was greater for thinner fat layers.

2.4.3. Ablation with cooled electrode

The results of the simulations using a cooled electrode are shown in Table 2.5. With this type of electrode and a 2 mm fat layer, augmenting frequency from 100 kHz to 10 MHz involved a significant increase in the depth of the lesion in the atrial wall, from 30.17% to 47.10%, and a moderate increase of T_{\max} (from 68.88 to 75.88°C). Regarding the thermal behavior and thickness of the fat layer, the results were similar to those found for the dry electrode with constant voltage: both T_{\max} and depth lesion decreased as fat thickness increased (Figure 2.4).

2.4.4. Comparison between ablation techniques

Figure 2.5 shows the results of computer simulations for the cases of fat thickness of 2 and 3 mm (atrial lesions were only observed in these cases and hence are used for comparison). The effect of frequency on atrial lesion depth was more marked in the cooled than dry electrodes (especially for thin fat layers of 2 mm). This effect was less marked at constant voltage. When temperature and current were constant, performance was less predictable (especially when we compared the cases 2 and 3 mm fat thickness). The effect of frequency on T_{\max} was only noticeable in the case of constant voltage. In the other ablation modes and with a cooled electrode, T_{\max} kept relatively constant with changes in frequency.

2.5. Discussion

The computer simulations in general showed the difficulty of ablating thick fat layers, as has been previously reported for the case of constant voltage (Berjano and Hornero 2004). In this study we assessed other modes of delivering RF power (constant temperature and current), along with the performance of a cooled electrode, and the effect of changing frequency.

The effect of frequency on T_{\max} and lesion depth in the case of constant voltage can be easily explained. Raising the frequency involves an increase in electrical conductivity (σ) of the atrial tissue (from 0.21 to 0.6 S/m), which means that more current will be delivered, and hence more power will be applied. Moreover, since the σ of the fat remains almost unaffected when frequency rises, this explains why the effect is more marked with thinner fat layers. Our results do not demonstrate that it is impossible to ablate atrial wall with constant voltage for fat layers over 4 mm. In fact, as shown in Table 2.2, the application of 30 V for the case of a 5 mm fat layer and 10 MHz, only involves a T_{\max} of 63.19°C, which means that higher voltage could be applied in order to increase lesion depth. As a consequence, and as is already known, each combination of electrode design and tissue characteristics determines the optimum combination of voltage and duration to enlarge the lesion without reaching 100°C. Our results with constant voltage

therefore only show the trend of T_{\max} and lesion depth when frequency is raised for different fat thicknesses. This trend can be summarized as follows: 1) Increasing fat thickness implies a decrease in T_{\max} and also in the depth of the lesion in the atrial wall, and 2) Increasing frequency involves higher T_{\max} and deeper lesions in the atrial wall, and additionally this increase is more noticeable when the atrial wall is thin. The results suggest that constant voltage is not a safe ablation method on the epicardial fat layer, since fat thickness is generally unknown and it is thus difficult to set a voltage value to achieve a lesion in the atrial wall and at the same time avoid excessive ($\approx 100^\circ\text{C}$) temperatures in the fat and atrial wall tissue. In contrast, ablating at a constant temperature provides safer heating, i.e. without excessive temperatures ($\approx 100^\circ\text{C}$), regardless of fat thickness. The obvious drawback is that when the fat layer is very thick (4-5 mm) it is nearly impossible to reach the atrial wall (see Figure 2.3B). In the constant current ablation we observed that the value of T_{\max} was almost independent of the frequency. This can be explained as follows: on one hand, the electrical conductivity of fat (σ_{FAT}) was not influenced by frequency (see Table 2.1), and on the other hand, electrical power was deposited within a very small zone around the active electrode (corresponding always to fat). Under these circumstances, T_{\max} was somehow proportional to $\sigma_{\text{FAT}} |\mathbf{E}|^2$, or equally $|\mathbf{J}|^2 / \sigma_{\text{FAT}}$. Since both the injected current (I) and contact surface (S) between electrode and tissue were constant, the value of $J (=I/S)$ at the electrode-fat interface was also constant, and this could hence explain this behavior of T_{\max} . Additionally, we observed that increasing fat thickness was directly related to an increase of T_{\max} (see Figure 2.3C). It seems that the change of the atrial tissue's σ_{A} (due to the different frequency) does not sufficiently affect the value of the total impedance of the tissue (Z_{TOTAL}), probably because the current density is low in this zone. However, increasing fat thickness (with $\sigma_{\text{A}} > \sigma_{\text{FAT}}$) does cause a rise in Z_{TOTAL} , and this implies an increase in the total delivered power ($I^2 \cdot Z_{\text{TOTAL}}$), which could raise the value of T_{\max} . This thermal behavior could be employed as a self-controlling procedure to ablate a thick layer of epicardial fat: at the beginning, when the layer is thick the current would create a high temperature which could melt the fat and reduce its thickness. During this process the total applied power would be reduced.

A study was also made of the performance of the cooled electrode. In this case, we observed that for 2 mm fat thickness, raising the frequency did involve a considerable increase in the depth of the lesion in the atrial wall. We are of the opinion that this is due to the location of T_{\max} being shifted towards deeper points by the cooling effect, i.e. in our case (thin fat layer) towards the atrial tissue, where electrical conductivity increases as frequency is higher. The rise in the electrical conductivity of the atrial tissue implies an increase in the RF deposited power, and hence in T_{\max} .

In our study we only considered an electrode size of 4 mm. Despite that it is known that the electrode length affects on the lesion dimensions in RF cardiac ablation, this is particularly true for endocardial approach, where the forced thermal convection caused by cooling blood on the electrode surface has a strong impact in tissue heat removing, and hence on the lesion depth. In contrast, since we modeled an epicardial approach, and under this condition there is not circulating blood around the electrode, we did not consider simulations for other electrode length. Regarding the electrode diameter, we only considered a value of 3 mm, which is about a 7Fr electrode. We think that the effect of increasing this parameter has different effect depending on the ablation protocol (constant temperature, voltage and current) and on the electrode type (dry vs. cooled), due to the change in diameter implies a change in tissue impedance as well. Likewise, the change in insertion depth also implies a change in the tissue impedance (Berjano and Hornero 2004). Additional considering a larger diameter electrode could produce different results quantitatively different to ours (both in lesion dimension and T_{\max}), however, we think that the general conclusions (see below) remain unaltered. Likewise, other factors, such as the angle between tissue surface and electrode axis, and the convective cooling coefficient at endocardium-blood interface, could show different results, but they were not considered in our study since that they have been previously characterized (Berjano and Hornero 2004, Panescu *et al* 1995b).

Since that our results suggest that RF ablation is clearly disadvantageous to ablate cardiac tissue in the presence of epicardial fat layer, other ablation modalities such as High Intensity Focused Ultrasound (HIFU), microwave or cryoablation,

could be potentially more useful. In this respect, the use of HIFU could be useful due to the lower value of attenuation of fat (≈ 6 dB/m-MHz) versus cardiac tissue (35-70 dB/m-MHz). In addition, the capability of microwave power would allow reaching deeper tissue sites. In contrast, the lower value of thermal conductivity of fat (0.2 W/m-K) versus cardiac tissue (0.7 W/m-K) does not suggest an advantage of thermal therapies exclusively based on thermal conduction, such as cryoablation.

2.6. Conclusions

- 1) The effect of increasing frequency on atrial lesion depth was more marked in the case of cooled electrodes than in dry electrodes, especially for thin fat layers (2 mm).
- 2) With dry electrodes, increasing frequency had little influence on atrial lesion depth in the case of constant voltage. In the cases of constant temperature and current, the performance was less predictable (especially with thick fat layers).
- 3) The effect of frequency on T_{\max} was only noticeable in the case of constant voltage. In the other ablation modes with a cooled electrode T_{\max} stayed relatively constant when frequency was altered.
- 4) In general, our computer results suggest that RF ablation of the atrial wall with overlying epicardial fat is difficult due to the marked difference in electrical conductivity between fat (0.025 S/m) and muscle (≈ 0.4 S/m). The epicardial fat layer seriously impedes the passage of RF current, thus reducing the effectiveness of atrial wall ablation. In this regard, it would be desirable to have a technique available to estimate the quantity of overlying epicardial fat prior to ablation (see Chapter 3). This would improve the current ablative techniques, since knowing the amount of epicardial fat present would make it possible to choose a particular RF power delivery protocol in order to optimize the thermal lesion.

Table 2.1. Characteristics of the elements employed in the computer modeling (data from Berjano and Hornero (2004))

Element	σ 100 kHz (S/m)	σ 1 MHz (S/m)	σ 10 MHz (S/m)	ρ (kg/m³)	c (J/kg·K)	k (W/m·K)
Atrial tissue	0.21	0.4	0.6	1200	3200	0.70
Fat	0.025	0.025	0.03	900	2222	0.20
Blood	0.99	0.99	0.99	1000	4180	0.54
Electrode	7.4·10 ⁶			8·10 ³	480	15
Plastic probe	10 ⁻⁵			70	1045	0.026

σ : electrical conductivity (at different frequencies and assessed at 36°C); ρ : mass density; c : specific heat; and k : thermal conductivity.

Table 2.2. Effect of frequency and thickness of fat layer on lesion geometry and maximal temperature (T_{\max}) at a **constant voltage of 30 V** for 60 s.

Frequency (kHz)	F (mm)	T_{\max} (°C)	D (mm)	W (mm)	D_{FAT} (%)	D_{A} (%)
100	2	76.91	3.18	6.50	100	39.20
	3	65.23	2.99	6.06	99.53	0
	4	60.54	3.33	5.80	83.32	0
	5	57.77	3.36	5.12	67.14	0
1000	2	81.60	3.40	6.88	100	46.50
	3	66.71	2.99	6.25	99.77	0
	4	61.23	3.40	5.85	85.05	0
	5	58.17	3.37	5.49	67.38	0
10,000	2	92.59	3.46	6.99	100	48.77
	3	73.71	3.13	6.55	100	4.30
	4	66.94	3.83	6.13	95.65	0
	5	63.19	3.61	6.04	72.14	0

F: Epicardial fat layer thickness, D: lesion depth, W: lesion width, D_{FAT} : Lesion depth in fat expressed as percentage of fat thickness, D_{A} : Lesion depth in atrial tissue expressed as percentage of atrium thickness (3 mm).

Table 2.3. Effect of frequency and fat thickness on lesion geometry and maximal temperature (T_{\max}) at a constant temperature of 70°C for 60 s.

Frequency (kHz)	F (mm)	T_{\max} (°C)	D (mm)	W (mm)	D_{FAT} (%)	D_{A} (%)
100	2	69.34	3.15	6.30	100	38.30
	3	69.15	3.14	6.99	100	4.70
	4	69.92	3.87	7.62	96.83	0
	5	69.89	4.42	7.66	88.30	0
1000	2	69.08	3.14	6.36	100	37.83
	3	70.66	3.18	7.09	100	5.87
	4	69.82	3.85	7.54	96.13	0
	5	69.11	4.38	7.74	87.68	0
10,000	2	70.41	3.10	6.32	100	36.73
	3	70.26	3.20	7.13	100	6.73
	4	69.07	3.86	7.45	96.55	0
	5	69.15	4.50	7.81	89.90	0

F: Epicardial fat layer thickness, D: lesion depth, W: lesion width, D_{FAT} : Lesion depth in fat expressed as percentage of fat thickness, D_{A} : Lesion depth in atrial tissue expressed as percentage of atrium thickness (3 mm).

Table 2.4. Effect of frequency and fat thickness on lesion geometry and maximal temperature (T_{\max}) at a constant current of 12 mA for 60 s.

Frequency (kHz)	F (mm)	T_{\max} (°C)	D (mm)	W (mm)	D_{FAT} (%)	D_{A} (%)
100	2	70.18	3.05	6.11	100	35.10
	3	79.16	3.240	7.44	100	8
	4	81.71	3.88	7.76	96.98	0
	5	82.24	4.43	8.10	88.68	0
1000	2	70.61	2.83	5.66	100	27.63
	3	79.44	3.42	6.94	100	14.13
	4	81.85	3.95	7.59	98.65	0
	5	82.32	4.55	8.08	90.90	0
10,000	2	70.80	2.75	5.71	100	25.10
	3	79.56	3.31	7.10	100	10.20
	4	81.91	3.93	7.86	98.28	0
	5	82.36	4.53	8.13	90.62	0

F: Epicardial fat layer thickness, D: lesion depth, W: lesion width, D_{FAT} : Lesion depth in fat expressed as percentage of fat thickness, D_{A} : Lesion depth in atrial tissue expressed as percentage of atrium thickness (3 mm).

Table 2.5. Effect of frequency and fat thickness on lesion geometry and maximal temperature (T_{\max}) using an RF cooled electrode and 38 V for 60 s.

Frequency (kHz)	F (mm)	T_{\max} (°C)	D (mm)	W (mm)	D_{FAT} (%)	D_{A} (%)
100	2	68.88	2.91	6.48	100	30.17
	3	60.05	2.87	6.26	95.63	0
	4	56.36	3.41	6.71	85.35	0
	5	53.92	3.36	6.23	67.22	0
1000	2	73.76	3.21	6.83	100	40.20
	3	61.69	3.12	6.84	100	4
	4	57.17	3.66	6.35	91.38	0
	5	54.38	3.83	5.85	76.62	0
10,000	2	75.88	3.41	6.90	100	47.10
	3	62.37	3.23	6.46	100	7.70
	4	57.50	3.59	6.07	89.65	0
	5	54.57	3.59	5.34	71.88	0

F: Epicardial fat layer thickness, D: lesion depth, W: lesion width, D_{FAT} : Lesion depth in fat expressed as percentage of fat thickness, D_{A} : Lesion depth in atrial tissue expressed as percentage of atrium thickness (3 mm).

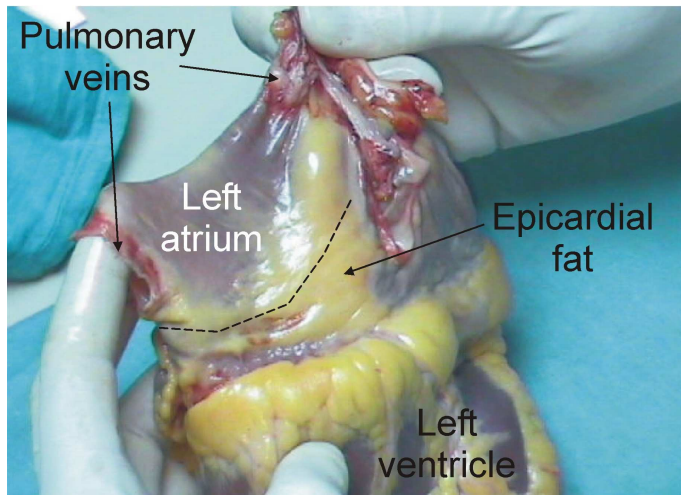


Figure 2.1. Explanted heart in which the presence of epicardial fat can be noted on left atrium. Dashed line represents a possible ablation line.

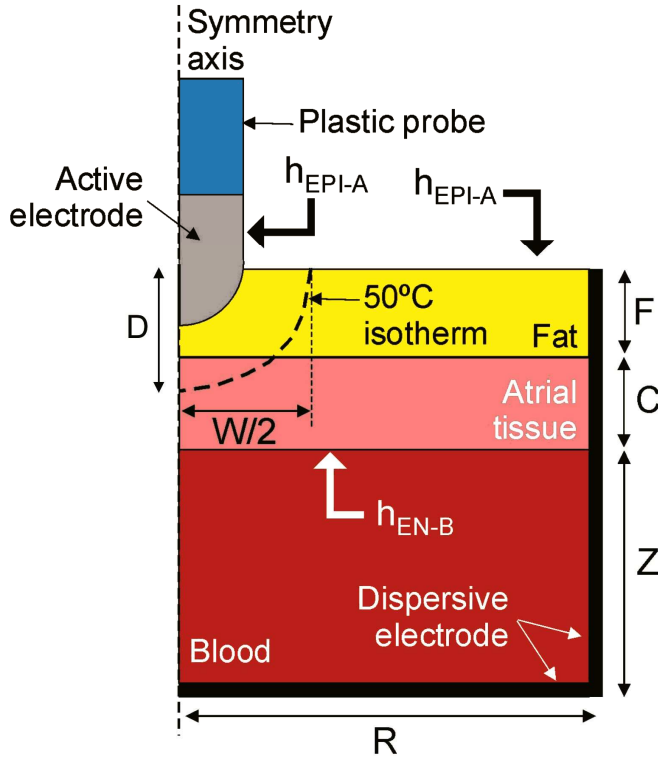


Figure 2.2. Two-dimensional theoretical model proposed (out of scale). Z and R : outer dimensions of the model; C : atrial wall thickness; F : epicardial fat thickness. h_{EPI-A} is the thermal transfer coefficient at the epicardium–ambient and electrode–ambient interfaces, while h_{EN-B} is the thermal transfer coefficient at the endocardium–blood interface. Depth (D) and width (W) of the lesion were assessed using the 50°C isotherm.

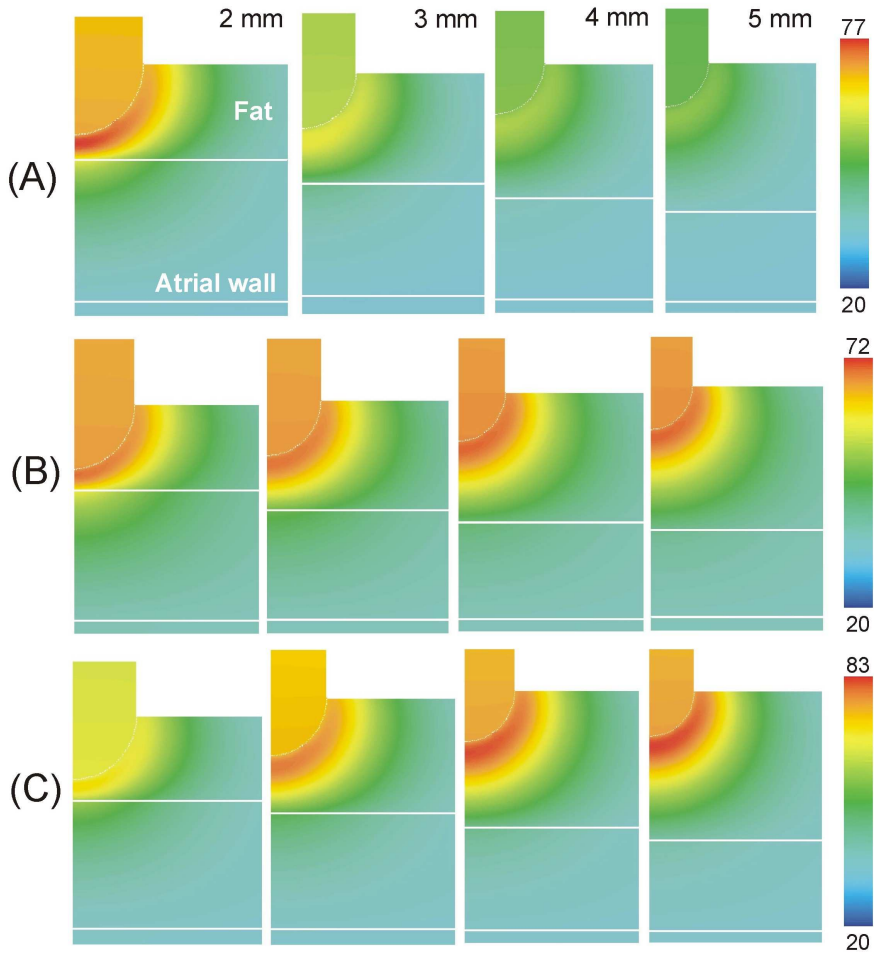


Figure 2.3. Temperature distributions at 60 s for the three modes of delivering RF power: (A) constant 30 V voltage, (B) constant 70°C temperature, (C) constant 12 mA current; and four values of epicardial fat thickness (2, 3, 4 and 5 mm). All the plots are for the case of 100 kHz frequency.

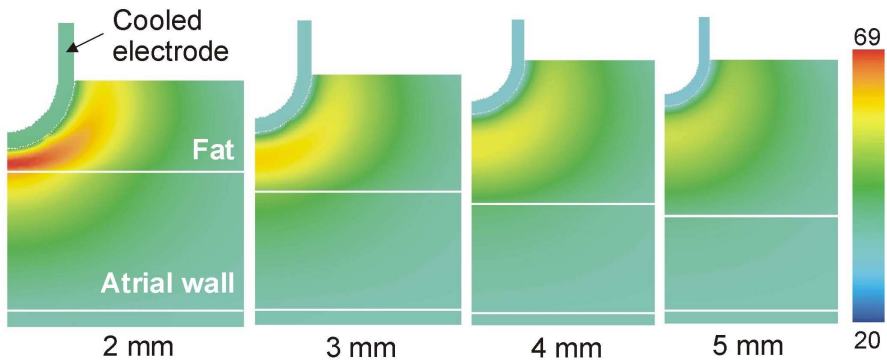


Figure 2.4. Temperature distributions at 60 s for RF ablation using a cooled electrode (38 V) and for four values of epicardial fat thickness (2, 3, 4 and 5 mm). All the plots belong to the 100 kHz frequency case.

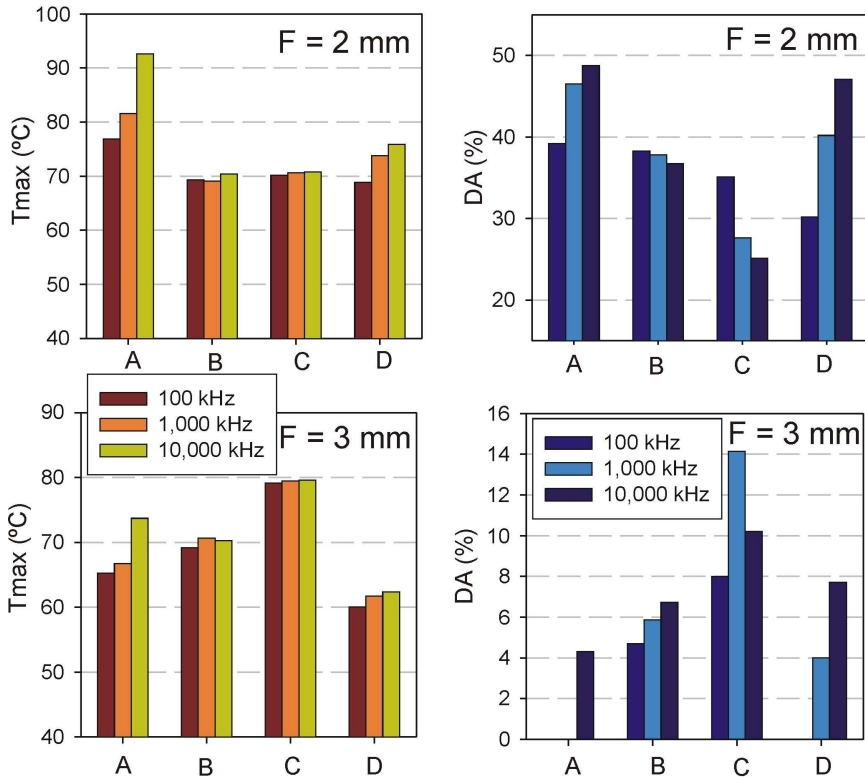


Figure 2.5. Maximal temperature (in °C) (left) and lesion depth in the atrial wall DA (% atrial wall thickness) (right) at 60 s for RF ablation using a dry electrode with different protocols: 30 V constant voltage (A), 70°C constant temperature (B), 12 mA constant current (C), (D) belongs to RF ablation using a cooled electrode and 38 V constant voltage. The figure also shows the results of three different frequencies: 100 kHz, 1 MHz and 10 MHz. The top plots belong to the case of 2 mm epicardial fat thickness and those at the bottom to the case of 3 mm epicardial fat thickness.

Chapter 3

Impedance measurement to assess epicardial fat prior to RF intraoperative cardiac ablation: feasibility study using a computer model

3.1. Abstract

Radiofrequency (RF) cardiac ablation is used to treat certain types of arrhythmias. In the epicardial approach, efficacy of RF ablation is uncertain due to the presence of epicardial adipose tissue interposed between the ablation electrode and the atrial wall. We planned a feasibility study based on a theoretical model in order to assess a new technique to estimate the quantity of fat by conducting bioimpedance measurements using a multi-electrode probe. The Finite Element Method was used to solve the electrical problem. The results showed that the measured impedance profile coincided approximately with the epicardial fat profile measured under the probe electrodes and also that the thicker the epicardial fat, the higher the impedance values. When lateral fat width was less than 4.5 mm, the impedance values altered, suggesting that measurements should always be conducted over a sizeable fat layer. We concluded that impedance measurement could be a practical method of assessing epicardial fat prior to RF intraoperative cardiac ablation, i.e. “to map” the amount of adipose tissue under the probe.

3.2. Introduction

Radiofrequency (RF) cardiac ablation can be used to treat certain types of arrhythmias, such as atrial fibrillation (AF), which is a common arrhythmia and an important public health problem due to its clinical prevalence and morbid-mortality (Kannel *et al* 1998, Benjamin *et al* 1994, Wolf *et al* 1991). The use of both surgical (intraoperative) and percutaneous (via a catheter) RF ablation to treat AF is increasing, in spite of the lack of accurate knowledge of the mechanisms involved. The effectiveness of surgical ablation is 70-80%, regardless of the kind of energy used (Khargi *et al* 2005, Cox *et al* 1996, Nakajima *et al* 2002). It is has been hypothesized that the early post-ablation recurrence of AF probably depends on the incomplete transmural of the lesion (Miyagi *et al* 2009). In fact, histological analyses of lesions have shown that 25-30% are non transmural cases (Santiago *et al* 2003a, 2003b, Deneke *et al* 2005). In the epicardial approach, i.e. when the energy to create the thermal lesion is applied on the epicardial surface, the efficacy of RF ablation is uncertain, due to the varying presence of epicardial adipose tissue interposed between the ablation electrode and target site, i.e. the atrial wall (Miyagi *et al* 2009, Berjano and Hornero 2004). This is probably due to the electrical conductivity of the fat being lower than that of atrial tissue (0.02 and 0.4-0.6 S/m respectively) (González-Suárez *et al* 2010a). In addition, since fat has a lower thermal conductivity (0.2 W/m·K) than atrial tissue (0.7 W/m·K), the presence of this fat layer also probably has a negative impact on creating a transmural lesion, regardless of the type of energy used. In order to maximize effectiveness of epicardial RF ablation therapy, Dumas *et al* (2008) used impedance measurements to predict completeness of lesions. Moreover, different types of energy are currently being researched, such as high intensity focused ultrasound (HIFU) (Mitnovetsky *et al* 2009), microwave (Pruitt *et al* 2007), laser (Hong *et al* 2007) and cryoablation (Ba *et al* 2008) in order to achieve optimum epicardial lesions in atrial tissue. We have previously used computer models to study the capability of different procedural techniques (different electrode designs and protocols for delivering RF power) to ablate atrial tissue in the presence of epicardial fat (González-Suárez *et al* 2010a). Since our results showed the difficulty of ablating the atrial wall in the

presence of thick fat layers (4-5 mm), it would be desirable to have a technique available to estimate the quantity of overlying epicardial fat prior to ablation. We therefore propose a new technique based on impedance measurements to assess epicardial fat thickness. Figure 3.1 shows the physical situation of the proposed technique, which is based on a multi-electrode probe placed over the epicardial surface. Our hypothesis is as follows: the electrical impedance measured between two or more electrodes of the probe could be closely related to the quantity of fat under the electrodes. For example, the impedance measured on a thin fat layer (Z_2) would be lower than on a thick layer (Z_1). An impedance profile (i.e. a set of impedance values, Z_1, Z_2, \dots) could therefore be used to obtain a fat profile.

Theoretical modeling has previously been used to assess the feasibility of new medical techniques and devices (Berjano and Hornero 2005a, 2006). In other words, this methodological approach has been employed as a concept proof. In our case, we designed a computer modeling study to determine the feasibility of the proposed technique. In this type of study it is also very important to assess the effect of external parameters, i.e. those affecting the final outcome when the device or technique is employed in a real stage. This can be done both to minimize their effects (because they involve an undesirable dispersion in the performance of the device) and to find optimum values for improving the performance of the device or technique. As computer modeling can also be used for this task, we used it to determine how anatomical factors (e.g. presence or lack of fat near the measuring electrodes) could affect the accuracy of the estimation of fat thickness.

3.3. Methods

3.3.1. Description of the theoretical model

Figure 3.2 shows the proposed theoretical model, which represents a straight probe over three parallel sections of tissue: epicardial fat, atrial wall and circulating blood, with thicknesses F , A and B , respectively. The probe was considered to have a rectangular section and 3 mm thickness, 1 mm in height and L total length. It consisted of 8 (stainless steel) electrodes 3 mm in length with 4 mm plastic segments

(polyurethane) between them. The first and last sections of the probe were also constructed of polyurethane with a length P (see Figure 3.2). Since there is a symmetry plane, only half of the model was considered.

3.3.2. Impedance measuring technique

We modeled impedance measurements using a tetrapolar (quadripolar) technique, i.e. an electrical current was injected between two outer electrodes and the voltage was measured between two inner electrodes (see Figure 3.3). This technique reduces the effect of electrode impedance and gives better accuracy than the bipolar technique (Grimmes and Martinsen 2008, Geddes 1989). A total of 5 impedance measurements were obtained: Z_A , Z_B , Z_C , Z_D and Z_E , where Z_A was the ratio between the voltage measured between electrodes 2 and 3 (V_{23}) and the current applied through electrodes 1 and 4 (I_{14}), i.e. $Z_A = V_{23}/I_{14}$; Z_B was the ratio between the voltage measured between electrodes 3 and 4 (V_{34}) and the current injected through electrodes 2 and 5 (I_{25}), i.e. $Z_B = V_{34}/I_{25}$; etc. In this way, the value of Z_A is related to the electrical conductivity of the tissue beneath electrodes 2 and 3, Z_B of the tissues beneath the electrodes 3 and 4, and so on until all the tissue under the probe has been “mapped”.

3.3.3. Governing equations

In a preliminary computer modeling study, we assessed the effect of changing the measuring frequency (between 10 kHz and 10 MHz) on the capability of this technique to estimate the epicardial fat profile, and the results suggested that the highest frequency (10 MHz) would be the best option (González-Suárez *et al* 2009). However, that frequency so high could produce practical problems such as electromagnetic interferences which affect other medical equipments and it would be therefore required to implement expensive methods to reduce these interferences. The value of electrical conductivity (σ) for atrial tissue was therefore considered for a frequency of 1 MHz. The biological medium at this frequency can be considered almost totally resistive, since the displacement currents are much less important than conduction currents. The only characteristic considered for the materials employed

in the model was electrical conductivity (Gabriel *et al* 1996): 0.025 S/m for the adipose tissue, 0.4 S/m for the atrial tissue, 0.99 S/m for the blood, 7.4×10^6 S/m for the electrodes (stainless steel) and 10^{-5} S/m for the plastic section of the probe (polyurethane). A quasi-static approach was employed to solve the electrical problem (Doss 1982). The Laplace Equation governed the physical phenomenon.

We used ANSYS version 10.0 (ANSYS, Canonsburg, PA, USA) to build theoretical models and solved them by means of the Finite Element Method (FEM). The SOLID69 element (linear isoparametric type) was used to solve the static electrical problem. This means that although the electrical variables in the theoretical model (voltage and current) are DC values, they correspond with the root-mean-square value of the AC signals in a real situation.

3.3.4. Boundary conditions

A Neumann boundary condition of null electrical current was used both on the symmetry plane and at the rest of the boundaries. To obtain each impedance measurement, we set a value of 1 A at a node inside one current injection electrode, and a value of -1 A at a node inside the other current injection electrode (Neumann boundary conditions (Brankov *et al* 2000)). Obviously, in a real situation, lower electrical current values would be used. A Dirichlet boundary condition of null electrical voltage was set at the nodes containing electrodes to pick up the electrical voltage. The voltage value of the other pick-up electrode corresponded directly with the impedance value, since the impedance was calculated from the ratio of the measured voltage to the total injected current (1 A).

3.3.5. Construction of the numerical model

The outer dimensions R, B and L (see Figure 3.2) were calculated by means of a convergence test in order to avoid boundary effects, i.e. they should be large enough to model an unlimited volume. A convergence test was also performed to obtain the correct spatial resolution (i.e. minimum meshing size). Discretization was spatially heterogeneous: the finest zone was always the electrode-tissue interface,

since it is known that this contains the largest voltage gradient. The meshing size was gradually increased with distance from the interface. In these convergence tests the value of the electrical impedance (Z) was used as a control parameter. First, we considered a tentative spatial resolution of 0.3 mm at the electrode-tissue interface. To determine the appropriate values of R , B and L we conducted a computer analysis by increasing the value of these parameters by equal amounts. When the difference between the impedance and the same parameter in the previous simulation was less than 0.5%, we considered the former values to be appropriate. Finally, we conducted a convergence test to determine the appropriate spatial resolution. The optimum spatial discretization was then achieved by refining the mesh in this zone so that Z was within 0.5% of the value obtained from the previous refinement step.

3.3.6. Effect of different fat profiles

To assess the effect of the overlying epicardial fat on the impedance measurements, we considered four shapes of fat profile: uniform (which corresponds with the model initially shown, see Figure 3.2), linear, convex and concave (see Figure 3.4). The atrial wall and blood layer had a thickness of 2 and 6 mm, respectively, in all the models. For the uniform profile, we studied the effect of changing the epicardial fat layer thickness (F) from 1 to 6 mm. For the other three profiles, we considered a variation of maximum fat thickness from 6 to 1 mm, with minimum fat thickness at 0.1 mm.

3.3.7. Effect of lateral width of epicardial fat

In previous simulations, we had considered only variation in the depth of epicardial fat (F), which meant it was considered to have limitless lateral width. In the present study we considered that the epicardial fat layer had limited lateral width (δ), as shown in Figure 3.5. The idea was to check the robustness of the new procedure, i.e. the impedance measurement should remain close to the value obtained without variation in the fat lateral width when δ was changed. For this part

of the study, only the uniform fat profile was considered. The simulations were performed by decreasing the lateral width (δ) at intervals of 2 mm from 18.5 to 0.5 mm, simultaneously increasing the value of F from 1 to 6 mm (at intervals of 1 mm).

3.4. Results

3.4.1. Construction of the model

The optimum outer dimensions were $R = 20$ mm, $B = 6$ mm, $L = 118$ mm and $P = 33$ mm. The convergence test provided a grid size of 0.3 mm in the finest zone (interface between fat and multi-electrode probe). We also checked the grid size away from the multi-electrode probe. The models had nearly 95,510 nodes and used over 524,000 tetrahedral elements.

3.4.2. Effect of different fat profiles

Figure 3.6 shows the impedance values for the different cases of fat profiles when the epicardial fat thickness varied between 1 and 6 mm. In the case of uniform fat profile (see Figure 3.6(a)), we observed that increasing F from 1 to 6 mm involved an increase in the impedance value, which was almost identical for all impedance measurements: Z_A increased from 103.6 Ω to 1223.3 Ω , Z_B from 103.5 Ω to 1218.4 Ω , Z_C from 103.4 Ω to 1218.6 Ω , etc.

Using the other fat profiles gave similar results: impedance readings decreased as maximum fat thickness was reduced. We also noticed that the impedance profiles followed a linear, convex and concave trend, respectively (Figure 3.6(b), (c) and (d)). Thus, for an $F = 6$ mm, with linear fat profile (Figure 3.6(b)), the impedance value decreased linearly from $Z_A = 917.7$ Ω to $Z_E = 182.7$ Ω . In the case of convex fat profile (Figure 3.6(c)) impedance decreased from $Z_A = 542.9$ Ω at the edge to $Z_C = 135.6$ Ω at the centre and then increased to $Z_E = 610$ Ω at the other edge. Finally, in the presence of a concave fat profile (Figure 3.6(d)), impedance increased from $Z_A = 534.6$ Ω to $Z_C = 823.5$ Ω and decreased to $Z_E = 447$ Ω . In conclusion, each impedance profile matched well with the corresponding fat profile.

3.4.3. Effect of lateral width of epicardial fat

Figure 3.7 shows the impedance values obtained by decreasing the lateral width of epicardial fat. We observed that decreasing fat lateral width (δ) involved a drop in the impedance reading, regardless of fat thickness. This effect was almost negligible for fat lateral widths > 4.5 mm, especially in the case of thin fat layers: the impedance value fell from 103.4Ω to 101.4Ω for the case of a 1 mm thin fat layer, while it dropped from 1218.6Ω to 1010.5Ω in the presence of a 6 mm thick fat layer. In contrast, this effect was more marked with smaller lateral widths (2.5 and 0.5 mm). For instance, with 6 mm of fat thickness impedance fell from 1218.6Ω to 673.1Ω for a lateral width of 2.5 mm and to 188.9Ω for 0.5 mm.

3.5. Discussion

Previous RF ablation studies showed the difficulty of ablating the atrial wall underneath a thick epicardial fat layer (González-Suárez *et al* 2009). We therefore proposed to conduct a feasibility study on a new technique based on impedance measurements to assess the thickness of the epicardial fat prior to RF cardiac ablation. This could improve the ablative technique in general, since a particular RF power delivery protocol could be chosen, or even a particular kind of HIFU, microwave or cryoablation energy in order to optimize the thermal lesion according to the amount of epicardial fat present.

In this study we showed that impedance readings varied with the quantity of fat present under the electrodes. This increase in impedance with epicardial fat thickness was obviously due to the lower electrical conductivity of the epicardial fat (0.025 S/m) as compared to atrial tissue (0.4 S/m). These results are in agreement with the computer-simulation results obtained by Berjano and Hornero (2004) using a two-dimensional mathematical model.

We also observed that the fat profile under the electrodes followed the same trend as the impedance measurement (see Figure 3.6). Our results showed that Z_A for concave fat profile was similar to Z_A for the case of convex fat profile ($\approx 550 \Omega$). This was due to the fact that the impedance map covers only the tissue zone between

electrodes 2 and 7, which means that the fat quantity under electrodes 2 and 3, i.e. those determining the Z_A value, is similar for the two fat profiles (see Figure 3.3).

Although the measurements were initially conducted by considering a fat layer with limitless lateral width, we conducted additional simulations to check whether the results would change in a real situation with limited fat width. Here again, our results showed that impedance values remained close to the results obtained previously for fat lateral widths over 4.5 mm (see Figure 3.7). This suggests that the proposed technique could fail when the multi-electrode probe is placed on epicardial fat with a thin lateral width (less than 4.5 mm).

The model proposed in this study is the first step in assessing epicardial fat prior to RF ablation and has certain limitations. On one hand, we only considered a multi-electrode probe with a rectangular section. Although this type of geometry could present a marked edge effect (Grimmes and Martinsen 2008), it was chosen because the ANSYS modeling technique was easier to implement. Future work should consider a probe with a more realistic geometry, such as a circular section and other factors such as electrode/tissue pressure could be included in the model, especially in the case of circular section probes. From a modeling point of view, this could be done by increasing the electrode insertion depth in the tissue.

3.6. Conclusions

The computational results suggest that measuring impedance could be a practical method of assessing epicardial fat prior to intraoperative cardiac ablation, i.e. “to map” the amount of adipose tissue under the probe. This is based on the fact that the impedance profiles obtained approximately coincided with the profiles of epicardial fat present under the electrodes of the probe.

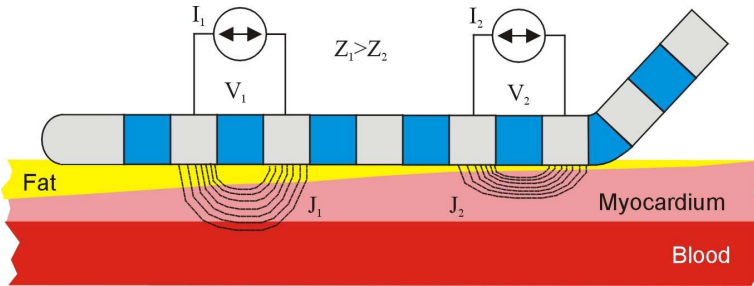


Figure 3.1. Physical situation considered in the study of the estimation of the epicardial fat profile. The idea is based on the fact that the electrical impedance measured between two or more electrodes of the probe could be strongly related to the quantity of fat under the electrodes. For example, the impedance measured on a thin fat layer ($Z_2 = V_2/I_2$) would be lower than on a thick fat layer ($Z_1 = V_1/I_1$).

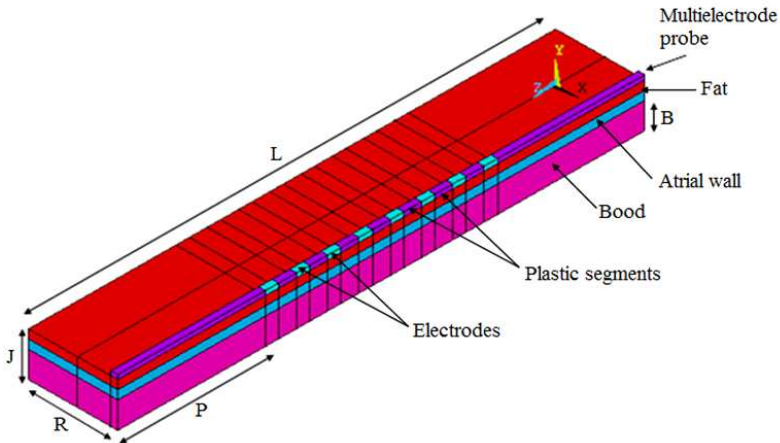


Figure 3.2. Theoretical model proposed with a uniform fat profile. Since there is a symmetrical plane, the model only includes half of all probe-tissues. R (half of the model), B (blood thickness) and L (length of the multielectrode probe): outer dimensions of the model; J : model thickness composed of three layers (F : epicardial fat thickness; A : atrial wall thickness; B : blood volume); P : distance from the first and last electrodes to the boundaries of the model.

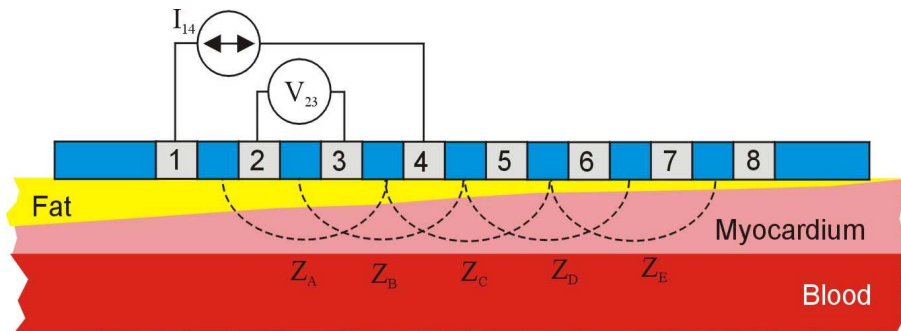


Figure 3.3. The impedance measurements were conducted by using a tetrapolar technique, i.e. an electrical current was injected between two outer electrodes, and an electrical voltage was measured between two inner electrodes. For instance, the figure illustrates by using electrodes 1 and 4 to inject current and electrodes 2 and 3 to pick up voltage, how it is possible "to map" the impedance Z_A (i.e. V_{23}/I_{14}) corresponding with the tissue zone lying beneath electrodes 2 and 3; Z_B (V_{34}/I_{25}) with the zone beneath electrodes 3 and 4, and consecutively until all the tissue under the probe has been "mapped".

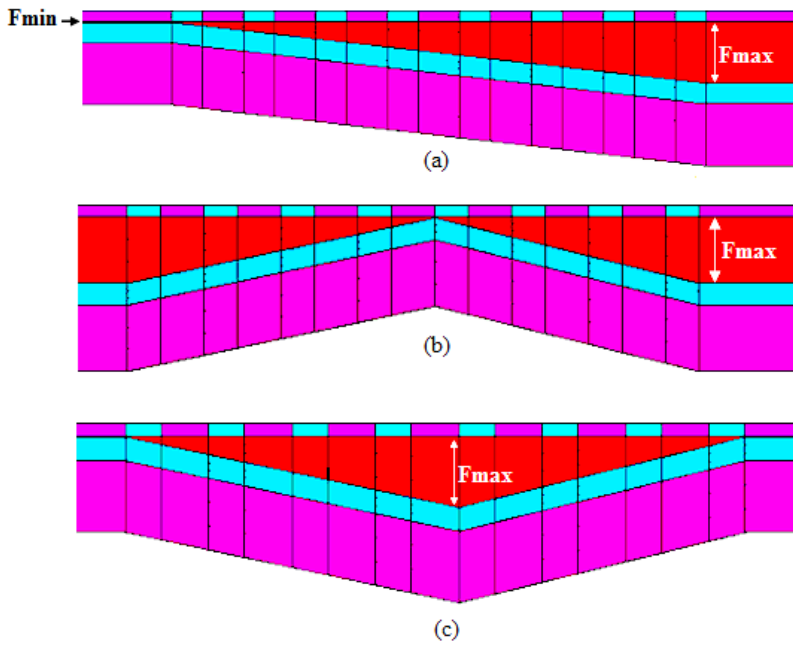


Figure 3.4. Theoretical models with different epicardial fat profiles: (a) linear, (b) convex, and (c) concave.

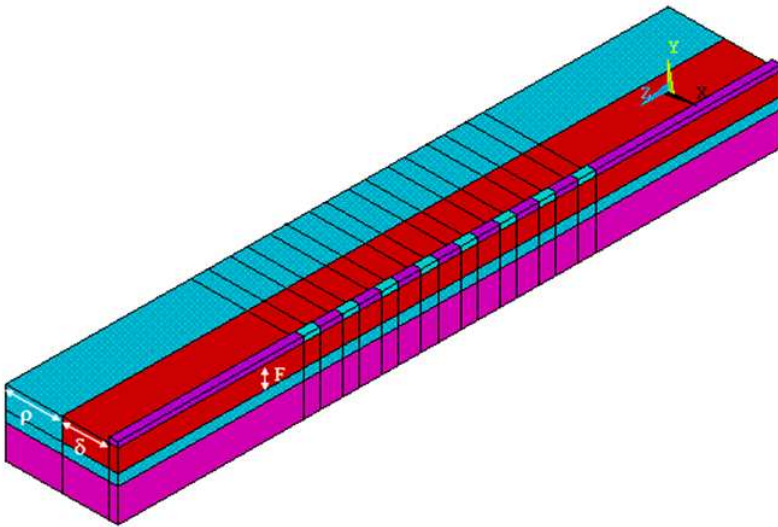
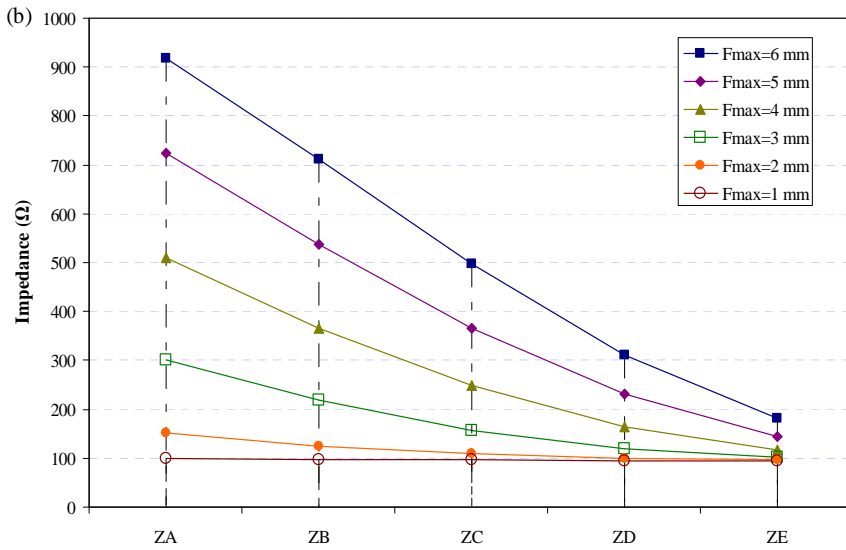
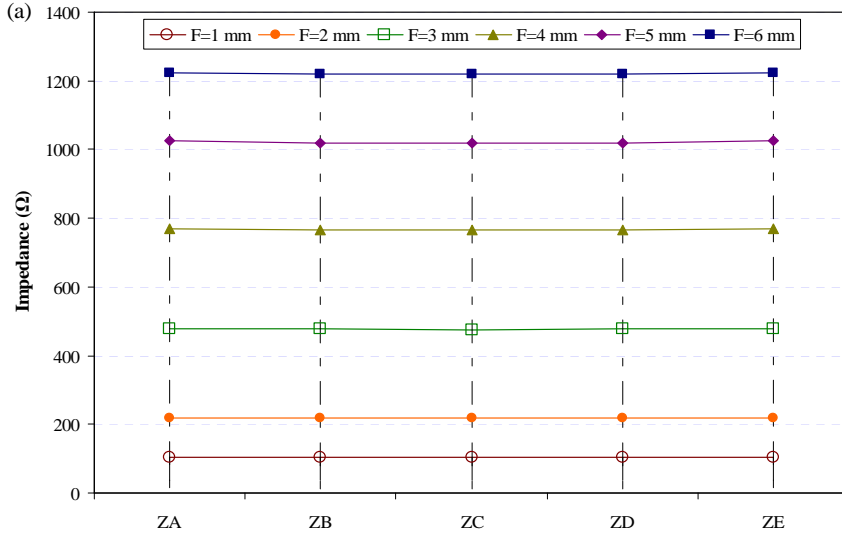


Figure 3.5. Model used to study the effect of lateral width of epicardial fat (δ) on the measured impedance. p : lateral width of atrial tissue; F : epicardial fat layer thickness.



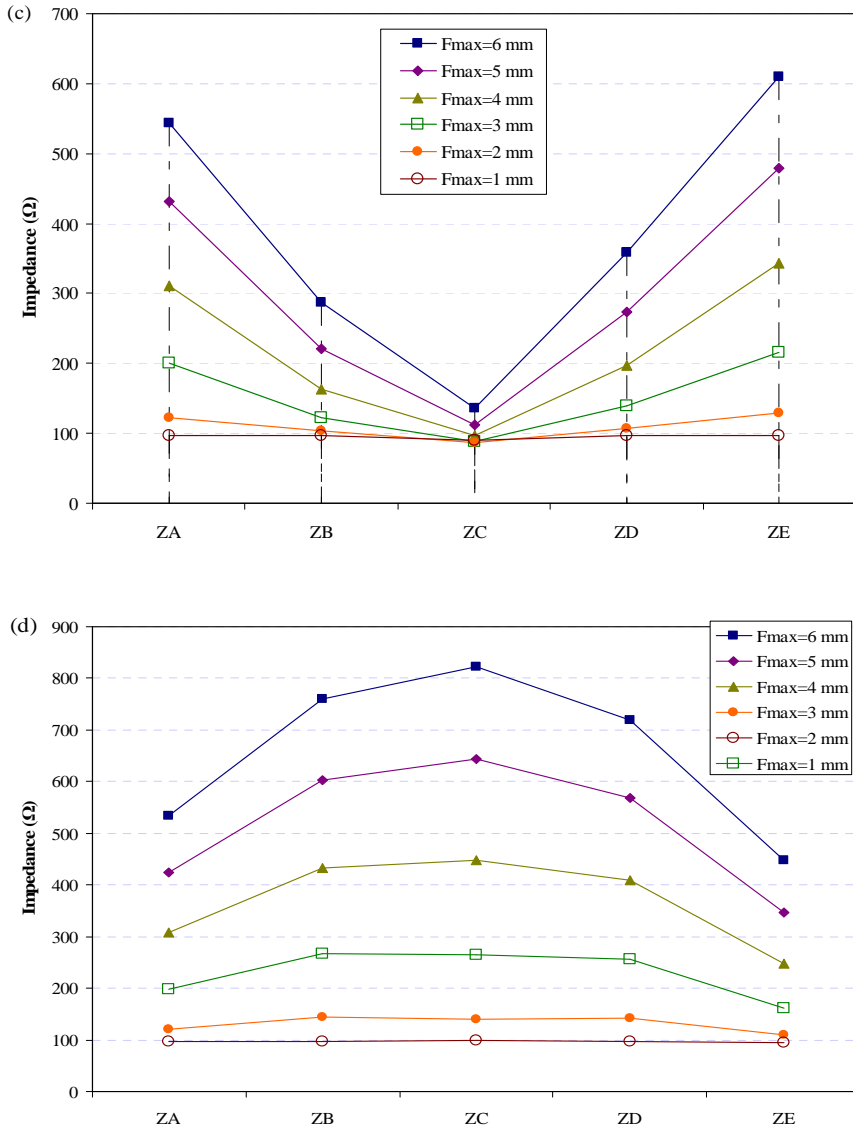


Figure 3.6. Impedance calculated for uniform (a), linear (b), convex (c), and concave (c) fat profiles.

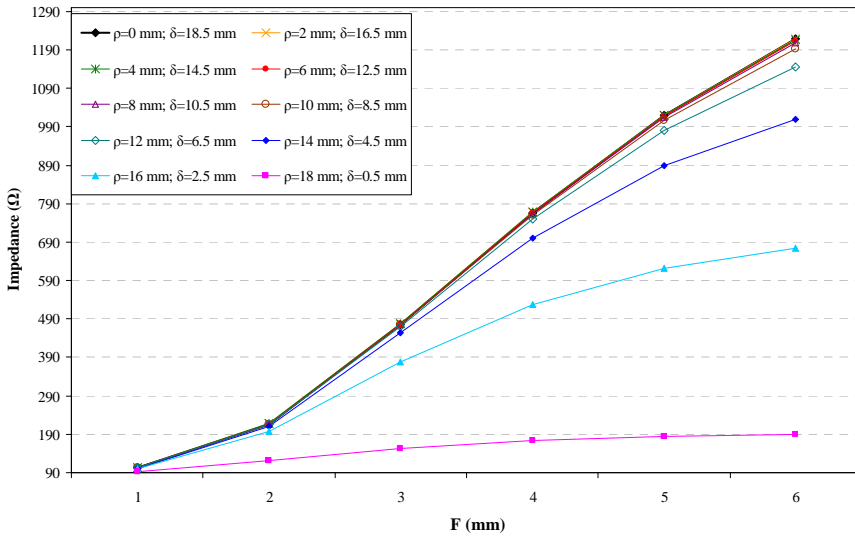


Figure 3.7. Impedance measurements by changing the lateral width of epicardial fat (δ) and the epicardial fat layer thickness (F).

Chapter 4

RF Ablation with Catheters Placed on Opposing Sides of the Ventricular Wall: Computer Modeling Comparing Bipolar and Unipolar Modes

4.1. Abstract

Purpose: To compare the efficacy of bipolar (BM) versus unipolar (UM) mode of radiofrequency ablation (RFA) in terms of creating transmural lesions across the interventricular septum (IVS) and ventricular free wall (VFW).

Materials and methods: We built computational models to study the temperature distributions and lesion dimensions created by BM and UM on IVS and VFW during RFA. Two different UM types were considered: sequential (SEUM) and simultaneous (SIUM). The effect of ventricular wall thickness, catheter misalignment and accidental presence of air in the epicardial space (in the case of VFW) were also studied.

Results: As regards IVS ablation, BM created transmural and symmetrical lesions for wall thicknesses up to 15 mm. SEUM and SIUM, on the other hand, were not able to create transmural lesions with IVS thicknesses ≥ 12.5 and 15 mm, respectively. Lesions were asymmetrical only with SEUM. For VFW ablation, BM also created transmural lesions for wall thicknesses up to 15 mm. However, with

SEUM and SIUM transmuralities were obtained for VFW thicknesses ≤ 7.5 and 12.5 mm, respectively. With the three modes VFW lesions were always asymmetrical. In the scenario with air surrounding the epicardial catheter tip, only SIUM was capable of creating transmural lesions. Overall, BM was superior to UM in IVS and VFW ablation when the catheters were not aligned.

Conclusions: Our findings suggest that BM is more effective than UM in achieving transmuralities across both ventricular sites, except in the situation of air surrounding the epicardial catheter tip.

4.2. Introduction

Successful radiofrequency ablation (RFA) of ventricular tachycardia (VT) originating from sites within the left ventricle such as the interventricular septum (IVS) is often limited by the presence of deep intramural circuits. The creation of such deep lesions while needed, cannot be always achieved with unipolar mode (UM) of RF ablation. Recent experimental studies have shown that using two catheters placed on opposing IVS surfaces to deliver RF in the bipolar mode (BM) allows deeper lesions to be created (Sivagangabalan *et al* 2010, Nagashima *et al* 2011). These results suggest that BM could be more effective than UM at eliminating VTs from deep intramural sites. However, the effects of different ventricular wall thicknesses and catheter alignment on the degree of transmuralities and lesion geometry created have never been studied in detail. Although, BM and UM have previously been compared in the ventricular free wall (VFW) ablations (d'Avila *et al* 2004, Dukkipati *et al* 2011, Sosa *et al* 2000), no information is available on their performance in an endocardium–epicardium approach. A recent study by Nagashima *et al* (2012) did consider this approach, but the effects of the above-mentioned factors were not included.

Our aim was to assess by means of computer modeling the thermal lesions created in the ventricular wall, in particular the degree of transmuralities achieved, in a comparison of BM and two different UM (sequential unipolar mode, SEUM and simultaneous unipolar mode, SIUM). As far as we know, there has not yet been a published study using a computational model to compare these ablation strategies.

Two and three-dimensional computational models were therefore developed and simulations were conducted to investigate temperature distribution and lesion geometry during RFA of the IVS (i.e. endocardium–endocardium approach) and VFW (i.e. endocardium–epicardium approach). The effect of wall thickness, catheter misalignment and the presence of air in the epicardial space were also studied. Although as a rule the epicardial space does not contain any air, during epicardial puncture and instrumentation, small amounts of air may accumulate around the ablation catheter.

4.3. Materials and methods

4.3.1. Computer modeling

Numerical models were based on a coupled electric-thermal problem which was solved numerically using the Finite Element Method (FEM) with COMSOL Multiphysics software (COMSOL, Burlington MA, USA). The governing equation for the thermal problem was the Bioheat Equation (Berjano 2006) which was modified by the enthalpy method (Abraham and Sparrow 2007, Byeongman and Alptekin 2010) incorporating the phase change to model tissue vaporization:

$$\frac{\partial(\rho h)}{\partial t} = \nabla \cdot (k \nabla T) + q - Q_p + Q_m \quad (1)$$

where ρ is density (kg/m^3), h enthalpy, t time (s), k thermal conductivity ($\text{W/m}\cdot\text{K}$), T temperature ($^{\circ}\text{C}$), q the heat source caused by RF power (W/m^3), Q_p the heat loss caused by blood perfusion (W/m^3) and Q_m the metabolic heat generation (W/m^3). Q_p and Q_m were not considered since the former can be ignored in the case of cardiac ablation (far from large vessels) (Haines and Watson 1989) and the latter is negligible in comparison to the other terms (Berjano 2006). In biological tissues enthalpy is related to tissue temperature by the following expression (Abraham and Sparrow 2007, Zhao *et al* 2007):

$$\rho h = \begin{cases} \rho_l c_l T & 0 < T \leq 99^\circ C \\ \rho h(99) + h_{fg} C \frac{(T - 99)}{(100 - 99)} & 99 < T \leq 100^\circ C \\ \rho h(100) + \rho_g c_g (T - 100) & T > 100^\circ C \end{cases} \quad (2)$$

where ρ_i and c_i are the density and specific heat of cardiac tissue before phase-change ($i=l$) and post-phase-change ($i=g$), respectively; h_{fg} is the latent heat and C the tissue water content. We considered a latent heat value of $2.162 \cdot 10^9 \text{ J/m}^3$, which corresponds to the product of the water vaporization latent heat and the water density at 100°C , and a tissue water content of 75% inside the cardiac tissue.

The thermal lesions created in the ventricular wall were assessed using the Arrhenius damage model (Chang 2010, Chang and Nguyen 2004), which associates temperature with exposure time using a first order kinetics relationship:

$$\Omega(t) = \int_0^t A e^{\frac{-\Delta E}{RT}} dt \quad (3)$$

where $\Omega(t)$ is the degree of tissue injury, R the universal gas constant, A the frequency factor (s^{-1}), and ΔE the activation energy for the irreversible damage reaction (J/mol). The parameters A and ΔE are dependent on tissue type; for the cardiac tissue we considered those proposed by Jacques and Gaenni (1989): $A = 2.94 \cdot 10^{38} \text{ s}^{-1}$ and $\Delta E = 2.596 \cdot 10^5 \text{ J/mol}$. We employed the thermal damage contour $\Omega = 1$ which corresponds to a 63% probability of cell death.

At the RF frequencies ($\approx 500 \text{ kHz}$) used in RF heating and over the distance of interest, the biological medium can be considered almost totally resistive, since the displacement currents are much less important than conduction currents. This means a quasi-static approach can be used to solve the electrical problem (Doss 1982). The distributed heat source q is then given by $q = \sigma |\mathbf{E}|^2$, where $|\mathbf{E}|$ is the magnitude of the vector electric field (V/m) and σ is electrical conductivity (S/m). \mathbf{E} is calculated from $\mathbf{E} = -\nabla\Phi$, where Φ is the voltage (V), which is obtained by solving Laplace's equation, which is the governing equation of the electrical problem:

$$\nabla \cdot (\sigma \nabla \Phi) = 0 \quad (4)$$

The models considered two internally cooled catheter tip electrodes (7Fr diameter, 4 mm catheter tip), similar to those used in RF cardiac ablation (d'Avila *et al* 2004, Dukkipati *et al* 2011, Watanabe *et al* 2010, Yokoyama *et al* 2006). Although open-irrigated catheters are commonly used in the case of VFW ablation (Nagashima *et al* 2012), these were associated with problems of fluid accumulation in the epicardial space (due to the catheter irrigation) necessitating frequent aspirations before each lesion (Kumar *et al* 2013). The volume of infused fluid into the epicardial space may also alter the biophysical properties of the pericardial fluid (d'Avila *et al* 2004) and interfere with catheter–tissue contact leading to inadequate lesion formation (Kumar *et al* 2013).

Figure 4.1 shows the model geometry for the IVS ablation case, i.e. both electrodes placed perpendicularly to the septum surfaces (endocardium–endocardium approach) and surrounded by circulating blood. Since the region under study has axial symmetry, a two-dimensional model was used. In the case of VFW ablation (endocardium–epicardium approach), the epicardial catheter is surrounded by pericardial fluid, and hence this approach was modeled by replacing the circulating blood with pericardial fluid on the epicardial side (not shown in Figure 4.1). We have also conducted additional computer simulations in which the pericardial fluid was replaced by air. The simulation of air around the epicardial catheter is important, since small amounts of air could be inadvertently introduced during epicardial puncture or during catheter manipulation during the procedure. Our simulations represented a worst-case scenario in which the electrode is completely surrounded by air.

Ventricular wall thickness (IVS or VFW) was varied between 5 and 15 mm. Ventricle dimensions X and Z were estimated by means of a convergence test in order to avoid boundary effects, using as control parameter the value of the maximal temperature achieved in the tissue (T_{\max}) after 120 s of heating. We first considered a tentative spatial (i.e. minimum meshing size) and temporal resolution. To determine the appropriate parameters of X and Z , we increased their values by equal amounts. When the difference in the T_{\max} between consecutive simulations was less

than 0.5%, we considered the former values to be adequate. We then determined adequate spatial and temporal resolution by means of similar convergence tests using the same control parameter as in the previous test. Discretization was spatially heterogeneous: the finest zone was always the electrode-tissue interface, where the largest voltage gradient was produced and hence the maximum value of current density. In the tissue, grid size was increased gradually with distance from the electrode-tissue interface.

We also built three-dimensional (3D) models, which were used to represent a scenario in which the two electrodes were not aligned exactly opposite to each other. These 3D models also allowed for simulation of parallel placement of the epicardial catheter tip (as opposed to perpendicular) to the epicardium during VFW ablation, as is usual in clinical practice.

The thermal and electrical properties of the model elements are shown in Table 4.1 (Schutt *et al* 2009, Gopalakrishnan 2002, Pätz *et al* 2009). Due to the lack of information on the electrical and thermal characteristics of the pericardial fluid we assumed it to have the same characteristics as saline (Gopalakrishnan 2002) as a first approximation. The electrical (σ) and thermal conductivity (k) of the cardiac tissue were temperature-dependent functions and were defined by piecewise functions. For σ we considered an exponential growth of 1.5%/°C up to 100°C (Schutt *et al* 2009) and then a drop of 4 orders for five degrees to model the desiccation process (Haemmerich *et al* 2003a), while k grew linearly 0.12%/°C up to 100°C, after which temperature k was kept constant (Berjano 2006).

Figure 4.2 shows the electrical and thermal boundary conditions applied to the model. The BM (Figure 4.2(a)) was electrically modeled with an electrical isolation boundary condition set at the model limits and a voltage drop of 40 V applied between the two electrodes throughout the total ablation time of 120 s (Sivagangabalan *et al* 2010), so that the electrical currents were always forced to flow between both electrodes. In the SEUM (Figure 4.2(b)), a constant zero voltage was always set at the model limits (mimicking the electrical performance of the dispersive electrode) and one of the active electrodes was set at 40 V while another was electrically isolated for the first 60 s. These conditions were reversed for the

subsequent 60 s, which gave a total ablation time of 120 s as in (Sivagangabalan *et al* 2010). In the SIUM (Figure 4.2(c)), as in the previous mode, the limits of the model were fixed at 0 V (dispersive electrode), while both electrodes were set at 40 V during the total ablation process (120 s), so that the electrical currents were forced to flow simultaneously between each catheter and the dispersive electrode.

Thermal boundary conditions (Figure 4.2(d)) were a null thermal flux on the symmetry axis and a constant temperature of 37°C (T_{body}) on the surfaces at a distance from the active electrode. The cooling effect produced by the blood circulating inside the ventricles ($T_{\text{blood}} = 37^\circ\text{C}$) was modeled by means of two forced thermal convection coefficients in the endocardium–blood ($h_{\text{CL}} = h_{\text{CR}}$) and electrode–blood ($h_{\text{EL}} = h_{\text{ER}}$) with a value of 708 W/m²K and 3636 W/m²K, respectively (Schutt *et al* 2009). In the VFW model, we considered a free thermal convection coefficient in the epicardium–air/pericardial fluid interface of 20 W/m²K. The cooling effect produced by the fluid circulating inside the electrode was not modeled realistically by means of internal tubes (the electrodes were empty, as shown Figure 4.1), but with a forced thermal convection coefficient (h_i) of 10629 W/m²K and a coolant temperature of 21°C (room temperature). The value of this coefficient was estimated by using the theoretical calculation of forced convection inside a tube (González-Suárez *et al* 2012). We considered an internal flow rate of 36 mL/min (d'Avila *et al* 2004) and half of the tube cross section (1.3 mm²).

4.4. Results

4.4.1. Development of computational models

We obtained a value of $X = Z = 40$ mm (ventricle dimensions), a grid size of 0.2 mm in the finest zone (electrode–tissue interface) and a step time of 0.05 s from the convergence tests. Tissue temperature did not reach more than 111°C in any of the simulations and the temperature in the catheter tip was always lower than 50°C (Sivagangabalan *et al* 2010), as is usual in clinical practice with this kind of electrodes.

4.4.2. Interventricular septum ablation

Figure 4.3 shows the temperature distributions and lesion shapes in the IVS after RFA, considering different septum thickness and the three ablation modes. The solid black line indicates the thermal damage borderline ($\Omega = 1$) and therefore outlines the lesion. Table 4.2 shows the lesion dimensions shown in Figure 4.3.

The lesions created in the IVS using BM (Figure 4.3(a)) were always transmural and symmetrical when the septum wall was between 5 and 15 mm thick, although their geometry differed slightly with thickness. When IVS was ≤ 10 mm, the maximum lesion width occurred in the middle of the septum, while for IVS ≥ 12.5 mm the lesion had an hourglass shape, with the minimum width at the middle of the septum.

The lesion shapes in the case of SEUM (Figure 4.3(b)) differed significantly from those obtained with BM. The most significant finding was that it was not possible to create transmural lesions for septum thicknesses ≥ 12.5 mm and lesions were asymmetrical. When the septum thickness was 15 mm, one would expect two identical lesions to be created independently due to the large distance between electrodes. However, the lesions remained asymmetrical. In fact, the lesion depth around the first activated electrode (left ventricular side) was 3.70 mm, as compared to 5.01 mm on the right side, where the electrode was the second to be activated. The lesions were also found to be in general wider around the secondly activated electrode (right ventricular side) (see surface and maximum widths in Table 4.2).

The lesion shapes in the case of SIUM are shown in Figure 4.3(c). As in BM, the lesions were symmetrical for all thicknesses considered. However, in this case, it was not possible to create transmural lesions for thicknesses ≥ 15 mm.

4.4.3. Ventricular free wall ablation

Figure 4.4 shows the temperature distributions and lesion shapes in the VFW after RFA, considering different ventricular thicknesses and the three ablation modes. Table 4.3 gives the dimensions of these lesions.

The lesions created with BM were transmural for thicknesses up to 15 mm, as shown in Figure 4.4(a) and lesion shape varied according to the thickness. For $VFW \leq 10$ mm, the maximum lesion width occurred in the middle of the ventricular wall (which has the same width as the epicardial surface), while for $VFW \geq 12.5$ mm the lesion had an hourglass shape, with the minimum width at the middle of the ventricular wall. However, unlike IVS ablation, the lesions were never symmetrical and were slightly wider around the electrode placed on the epicardium (right side).

The SEUM was only able to create transmural lesions when the VFW was ≤ 7.5 mm (Figure 4.4(b)). The lesions were always asymmetrical and considerably larger on the epicardial side, regardless of ventricular wall thickness. The most important difference with the IVS case was that the lesion width on the epicardial side was much larger.

With SIUM it was possible to create transmural lesions for $VFW \leq 12.5$ mm (Figure 4.4(c)). The lesion shapes were always asymmetrical and wider around the electrode placed on the epicardium, unlike the IVS ablation.

4.4.4. Effect of air on the epicardial side

We assessed the effect of the accidental presence of air around the epicardial catheter tip. Figure 4.5 shows the temperature distributions and lesion geometries in the VFW using the three modes of ablation. The most important finding was the absence of a thermal lesion on the endocardial side with BM (Figure 4.5(a)). SEUM also failed to create transmural lesions, although a lesion did form on the endocardial side (see Figure 4.5(b)). The lesions created on each side of the wall had similar shapes, with a depth and width of approximately 4 mm and 7 mm, respectively. SIUM was the only technique capable of creating a transmural lesion, which was symmetrical in the shape of an hourglass (see Figure 4.5(c)).

4.4.5. Effect of changing the orientation of epicardial catheter

We also assessed the effect of changing the orientation of the epicardial catheter tip from perpendicular to parallel, as is usual in clinical practice. We used a

3D model due to the lack of axial symmetry in this situation. The BM ablation and pericardial fluid in the epicardial space were considered since it was the best scenario in which transmural lesions were achieved. Figure 4.6 shows the temperature distributions and lesion shapes in the VFW with BM. The lesion shapes in both situations were almost identical, which suggests that the orientation of the epicardial catheter tip does not have a significant effect on lesion geometry.

4.4.6. Effect of the misalignment of catheters

We assessed the effect of the progressive misalignment of the catheters on lesion dimension and transmurality in both IVS and VFW. Only BM and SIUM were considered since we had seen that they were superior to SEUM in creating transmural lesions in both scenarios. Catheter misalignment was varied in steps of 2.5 mm from 0 mm (no misalignment) until the lesion was no longer transmural. The temperature distributions and lesion geometries in the IVS and VFW (both 10 mm thickness) with BM and SIUM are shown in Figures 4.7 and 4.8, respectively.

In general, the lesions were seen to become longer as misalignment increased and the lesion shape became more hourglass-like. BM was superior to SIUM in IVS ablation, since it was capable of creating transmural lesions up to a catheter misalignment of 10 mm. The lesions were always symmetrical in IVS ablation, regardless of ablation mode and catheter misalignment (see Figure 4.7). In the case of VFW ablation, BM was also more effective than SIUM in creating transmural lesions, which happened until catheter misalignment reached 12.5 mm, as shown in Figure 4.8. Unlike IVS ablation, the lesions were asymmetrical and wider on the epicardial surface and were even wider with SIUM.

4.5. Discussion

Our objective was to compare the efficacy of BM and two different UM (SEUM and SIUM) in RF cardiac ablation. Specifically we attempted to look at their ability to create transmural lesions across ventricular tissue in two locations: 1) across the IVS with the electrodes located on either side of the septum, and 2) across

the VFW with one electrode located on the endocardial side of the ventricle and the other on its epicardial surface.

The computer modeling results demonstrated that BM created larger lesions than SEUM and SIUM across the IVS (see Figure 4.3). These findings are in agreement with those obtained in previous experimental studies on bipolar ablation of the IVS. Nagashima *et al* (2011) compared BM and SEUM using saline-irrigated electrodes on excised swine hearts and found that BM produced a higher number of transmural lesions. Sivagangabalan *et al* (2010) also found that BM required fewer ablations to achieve block across ablation lines and created larger lesions in a post infarct ovine model. It is worthy of note that in this study we found the upper transmural limit when using BM (40 V/120 s) across IVS thicknesses up to 15 mm. Although this was assessed using the above parameters in computer modeling, this conclusion is relevant when one is targeting hypertrophied left ventricular myocardium. Interestingly, we also observed that lesions were not symmetrical during SEUM; the lesions were in general larger (in depth and width) on the side of the second activated catheter. We believe that this could be due to the result of higher electrical conductivity on the site of the lesion created around the second activated catheter, due to residual heating from the preceding lesion (electrical conductivity at a given point is inversely proportional to the absorbed RF power and hence to heating) and likely facilitates the deposition of more RF power. The difference in thermal dosage may seem negligible, but our results suggest that this could be significant and may explain the differences in the SEUM lesions in previous experimental results (Sivagangabalan *et al* 2010).

Our results also suggest that BM creates larger lesions than both UM across the VFW (see Figure 4.4), with the lesions being always asymmetrical. This is true as long as the epicardial catheter tip is not surrounded by air, as shown in Figure 4.5. The results show that in this situation, BM produces a thermal lesion only on the epicardial side, making transmural unlikely. This is due to the large difference in electrical current density between the catheter tips, i.e. on the epicardial side the electrode would have limited contact with the tissue, resulting in a lower effective contact area and hence a higher current density; while on the other hand the

endocardial catheter which would be completely surrounded by cardiac tissue and blood (the electrical conductivity of blood is even higher than cardiac tissue) resulting in a lower current density. As the RF power absorbed by the tissue (directly converted into heat) is directly proportional to the square of current density, lesions will be preferentially (or even exclusively) created around the epicardial catheter tip due to its high current density, as opposed to on the endocardial surface. In other words, when air is present around the epicardial catheter tip BM should not be considered as a pure bipolar mode across the VFW. In fact, the temperature distribution shown in Figure 4.5(a) suggests that the electrode on the epicardium actually behaves as a single active electrode, whereas the electrode on the endocardium plays the role of a dispersive electrode, thus giving negligible heating in its vicinity (definition of unipolar mode). SIUM is therefore likely to be more effective than BM in achieving transmural lesions under this condition (see Figure 4.5(c)), at least for wall thicknesses up to 10 mm. From a practical point of view, the presence of air around the epicardial catheter tip could be checked pre-ablation by measuring the unipolar impedances, i.e. between the epicardial electrode and the patch. A much higher value than that found between the endocardial electrode and the patch would suggest the presence of air or suboptimal conditions, favoring non transmural lesions.

The effect of changing the orientation of the catheter tip to the epicardial surface (from perpendicular to parallel) on lesion development during VFW bipolar ablation seems to be insignificant as suggested by the results shown in Figure 4.6.

We also observed that BM was superior to UM in IVS and VFW ablation when both catheters were misaligned, as shown in Figures 4.7 and 4.8. In the case of VFW ablation, transmuralities were maintained up to a misalignment of 12.5 mm between electrodes, while in IVS ablation transmuralities were maintained only up to 10 mm misalignment. This is due to more power being lost in bipolar IVS ablation from heat removal by circulating blood.

4.5.1. Study Limitations

Our study used has certain limitations. We modeled an internally cooled catheter (i.e. closed-irrigated catheter), and although these catheters are used for clinical RF ablation of cardiac tissue (d'Avila *et al* 2004, Dukkipati *et al* 2011, Watanabe *et al* 2010), other types of catheters, such as non-irrigated and open-irrigated catheters, are also employed for this type of intervention. The conclusions reached in this study could therefore be different when using other catheter designs. In addition, although different lesions could be created when considering: a) different insertion depths of the catheter tip into tissue and b) different voltage/time settings, it is likely that the above conclusions regarding the impact on the lesion geometry of BM vs. UM, ventricular wall thickness, and misalignment between electrodes will remain essentially unchanged. The results could be also different using other ablation times, such as in the case of SEUM with 120+120 s in order to balance the comparative study in a different way. Finally, it is important to point out that our study modeled a SIUM based on a voltage applied simultaneously through both electrodes, which is equivalent to using a single RF generator. Otherwise, a SIUM in which two independent RF generators are delivering two voltage signals "isolated from one another" could also provide different results.

4.6. Conclusions

Our findings suggest that BM for RF cardiac ablation on IVS and VFW is superior to both UM in terms of achieving lesion transmural across ventricular walls. This holds true even when the catheters are misaligned as can occur clinically. The only situation in which BM is inferior to UM is in the case of VFW ablation, when there is air around the epicardial catheter tip, in which SIUM is the only mode capable of creating transmural lesions. The results also suggest that the orientation of the catheter tip, i.e. perpendicular vs. parallel, on the epicardial surface during VFW bipolar ablation does not result in significantly different lesion shapes and dimensions.

Table 4.1. Thermal and electrical characteristics of the elements of the numerical models (data from Schutt *et al* (2009), Gopalakrishnan (2002), Pätz *et al* (2009)).

Element/Material		σ (S/m)	k (W/m·K)	ρ (kg/m ³)	c (J/kg·K)
Electrode		$4.6 \cdot 10^6$	71	21500	132
Plastic		10^{-5}	0.026	70	1045
Blood		0.99	0.54	1000	4180
Pericardial fluid (saline)		1.35	0.628	980	4184
Cardiac tissue	Liquid phase	0.541	0.531	1060	3111
	Gas phase			370.44	2155.92

σ , electric conductivity; k , thermal conductivity; ρ , density; and c , specific heat.

Table 4.2. Lesion dimensions (in mm) in the interventricular septum (IVS) for different septum thickness and three modes of RF ablation: bipolar mode (BM), sequential unipolar mode (SEUM) and simultaneous unipolar mode (SIUM).

Ablation Mode	IVS thickness	MW1	SW1	IW	MW2	SW2	D1	D2
BM	10	= IW	6.02	10.43	= IW	=SW1	transmural	
	12.5	8.18	5.56	7.55	=MW1	=SW1	transmural	
	15	9.51	7.28	7.06	=MW1	=SW1	transmural	
SEUM	10	6.80	5.39	3.34	9.29	7.87	transmural	
	12.5	6.39	5.14	-	8.80	7.75	3.78	5.36
	15	6.34	5.11	-	8.86	7.48	3.70	5.01
SIUM	10	= IW	8.35	11.26	= IW	=SW1	transmural	
	12.5	8.46	6.77	3.68	=MW1	=SW1	transmural	
	15	9.16	7.26	-	=MW1	=SW1	5.62	=D1

MW: maximum width; IW: intermediate width; SW: surface width; and D: depth.

1: left side and 2: right side.

Table 4.3. Lesion dimensions (in mm) in the ventricular free wall (VFW) with the epicardial catheter surrounded by pericardial fluid for different wall thickness and three modes of RF ablation: bipolar mode (BM), sequential unipolar mode (SEUM) and simultaneous unipolar mode (SIUM).

Ablation Mode	VFW thickness	MW1	SW1	IW	MW2	SW2	D1	D2
BM	7.5	12.65	8.23	=MW1	=MW1	=MW1	transmural	
	10	13.90	8.58	=MW1	=MW1	=MW1	transmural	
	12.5	11.38	8.05	11.96	13.51	=MW2	transmural	
	15	10.08	7.61	8.40	12.78	=MW2	transmural	
SEUM	7.5	6.73	5.79	6.07	11.61	10.48	transmural	
	10	5.58	4.71	-	12.25	11.67	3.29	5.58
	12.5	5.72	5.12	-	12.58	12.10	3.36	5.72
	15	6.72	5.72	-	12.47	12.03	3.90	4.68
SIUM	7.5	11.67	7.35	=MW1	16.65	=MW2	transmural	
	10	7.52	9.74	11.38	17.67	=MW2	transmural	
	12.5	7.41	6.02	4.13	16.45	=MW2	transmural	
	15	7.79	6.82	-	16.01	=MW2	4.81	5.53

MW: maximum width; IW: intermediate width; SW: surface width; and D: depth.

1: left side and 2: right side.

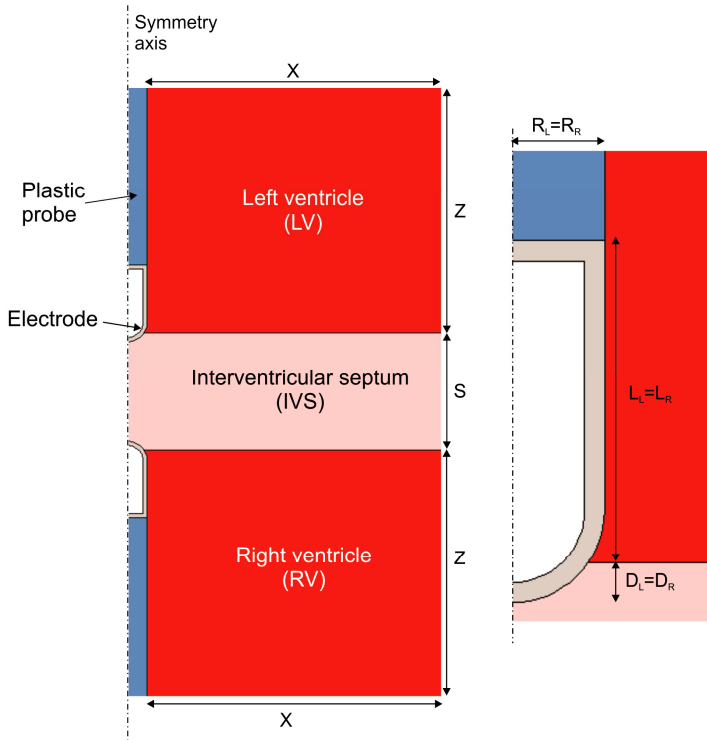


Figure 4.1. Left: Geometry of the computational model for interventricular septum (IVS) ablation. Septum thickness: S . The geometry of the model for ventricular free wall (VFW) ablation was similar, but circulating blood in one ventricle was replaced by pericardial fluid or air. Ventricle dimensions X and Z were obtained from a convergence test. Right: Detail of the electrode on the tissue. Electrode radius: $R_L = R_R = 1.155$ mm (7 Fr), electrode lengths: $L_L = L_R = 3.5$ mm (0.25 mm thickness wall), and insertion depth: $D_L = D_R = 0.5$ mm.

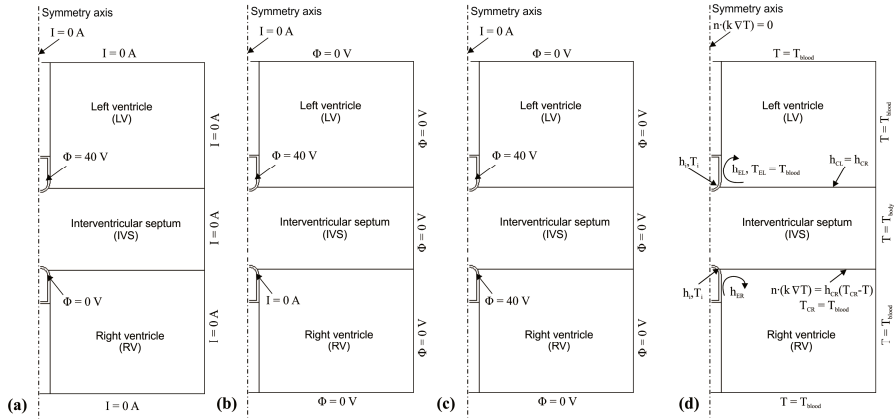


Figure 4.2. Electrical boundary conditions of the model for interventricular septum (IVS) ablation for **(a)** bipolar mode (BM), **(b)** sequential unipolar mode (SEUM) and **(c)** simultaneous unipolar mode (SIUM). **(d)** Thermal boundary conditions for all cases. $h_{CL} = h_{CR}$ and $h_{EL} = h_{ER}$ are the thermal transfer coefficients at the endocardium–blood and the electrode–blood interfaces, respectively.

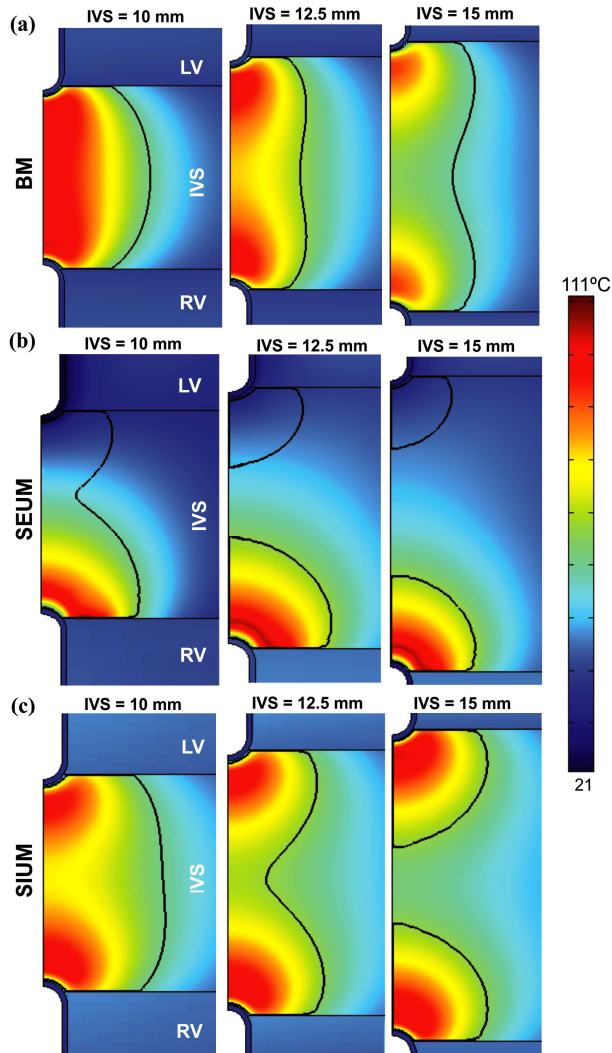


Figure 4.3. Temperature distribution in the tissue after 120 s of RFA across the interventricular septum (IVS) for different septum thickness from 10 to 15 mm, considering three modes of ablation: **(a)** bipolar mode (BM), **(b)** sequential unipolar mode (SEUM), and **(c)** simultaneous unipolar mode (SIUM). The solid black line is the thermal damage border ($\Omega=1$). RL: right ventricle, and LV: left ventricle.

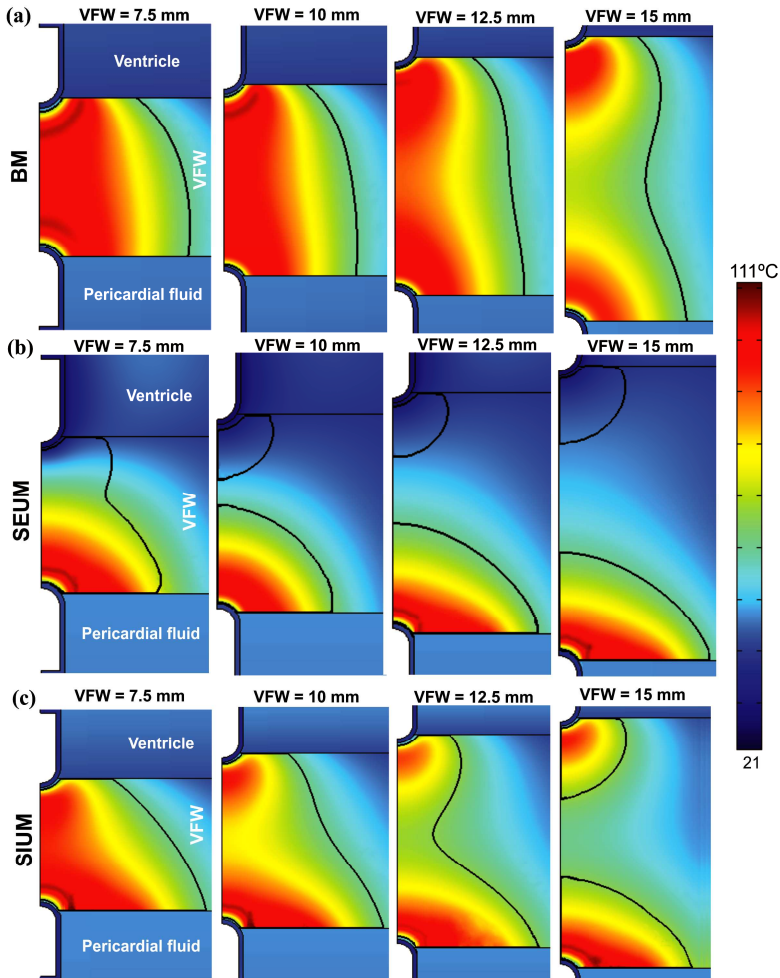


Figure 4.4. Temperature distribution in the tissue after 120 s of RFA across the ventricular free wall (VFW) with pericardial fluid in the epicardial space, considering different wall thickness from 7.5 to 15 mm and three modes of ablation: (a) bipolar mode (BM), (b) sequential unipolar mode (SEUM), and (c) simultaneous unipolar mode (SIUM). The solid black line is the thermal damage border ($\Omega = 1$).

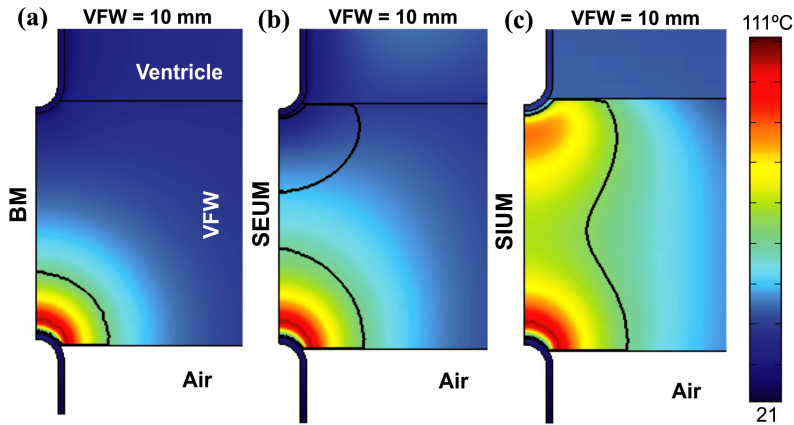


Figure 4.5. Temperature distributions after 120 s of RFA across the VFW (10 mm wall thickness) with the epicardial catheter surrounded by air, considering three modes of ablation: (a) bipolar mode (BM), (b) sequential unipolar mode (SEUM), and (c) simultaneous unipolar mode (SIUM). The solid black line is the thermal damage border ($\Omega = 1$).

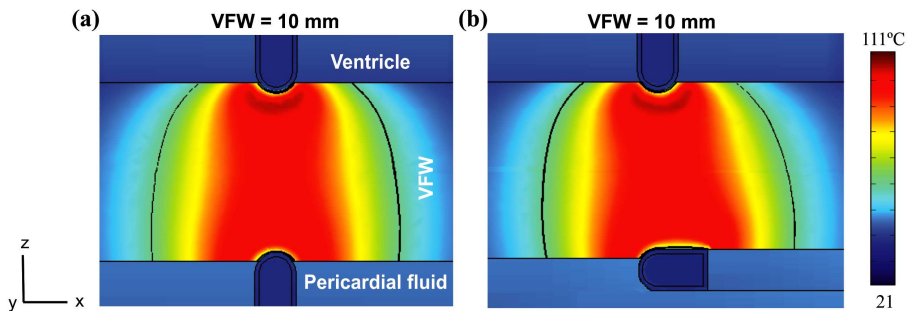


Figure 4.6. Temperature distributions after 120 s of RFA with BM across VFW (10 mm thickness) comparing two orientations of the epicardial catheter: (a) perpendicular and (b) parallel to the epicardium. The solid black line is the thermal damage border ($\Omega = 1$).

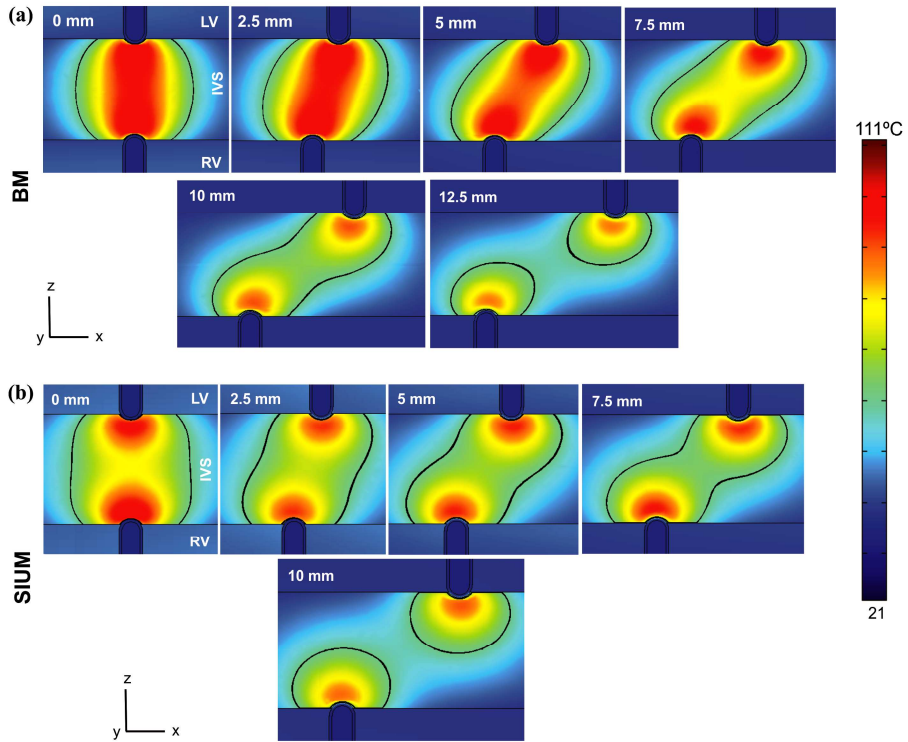


Figure 4.7. Temperature distributions in the tissue after 120 s of RFA with BM **(a)** and SIUM **(b)** across the IVS (10 mm thickness), increasing the misalignment between catheters in steps of 2.5 mm until the lesion was no longer transmural. Note that the lesions were transmural when they reached all the tissue at a plane of the wall, including the center. The solid black line is the thermal damage border ($\Omega = 1$).

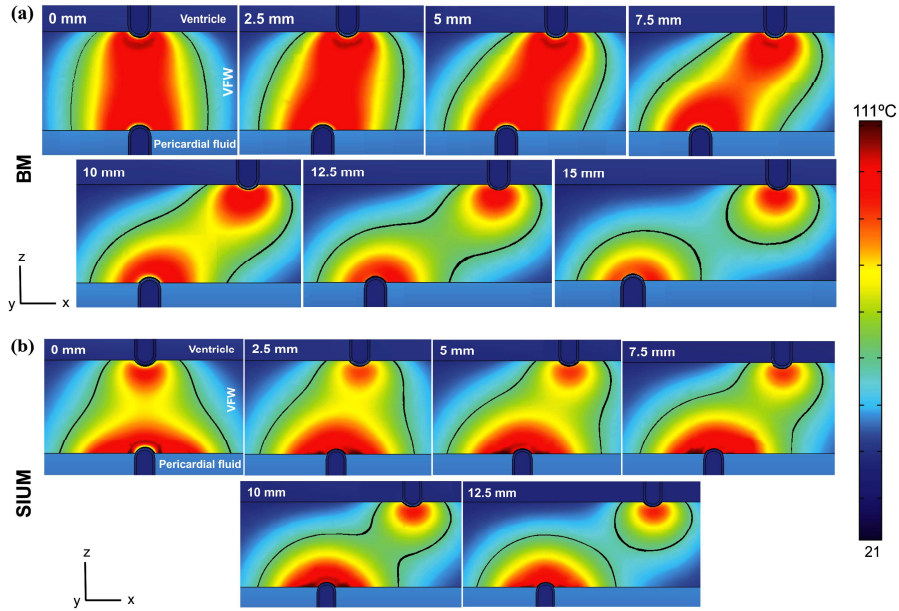


Figure 4.8. Temperature distributions in the tissue after 120 s of RFA with BM and SIUM (b) across the VFW (10 mm thickness), increasing the misalignment between catheters in steps of 2.5 mm until the lesion was no longer transmural. The solid black line is the thermal damage border ($\Omega = 1$).

Chapter 5

Feasibility study of an internally cooled bipolar applicator for RF coagulation of hepatic tissue: Experimental and computational study

5.1. Abstract

Purpose: To study the capacity of an internally cooled radiofrequency (RF) bipolar applicator to create sufficiently deep thermal lesions in hepatic tissue.

Materials and methods: Three complementary methodologies were employed to check the electrical and thermal behavior of the applicator under test. The experimental studies were based on excised bovine (ex vivo study) and porcine liver (in vivo study) and the numerical models were solved by means of the Finite Element Method (FEM).

Results: Experimental and computational results showed good agreement in terms of impedance progress and lesion depth (4 and 4.5 mm respectively for ex vivo conditions, and ≈ 7 and 9 mm respectively for in vivo conditions), although the lesion widths were overestimated by the computer simulations. This could have been due to the method used to assess the thermal lesions; the experimental lesions were assessed by the white coagulation zone whereas the tissue damage function was used to assess the computational lesions.

Conclusions: The experimental results suggest that this applicator could create in vivo lesions to a depth of around 7 mm. It was also observed that the thermal lesion is mainly confined to the area between both electrodes, which would allow lesion

width to be controlled by selecting a specific applicator design. The comparison between the experimental and computational results suggests that the theoretical model could be usefully applied in further studies of the performance of this device.

5.2. Introduction

Radiofrequency (RF) energy devices are widely used to thermally coagulate hepatic tissue e.g. in the destruction of surface tumors (Topp *et al* 2004, Gnerlich *et al* 2009) or minimizing blood loss during hepatic resection by creating thermal coagulative necrosis along the transection plane (Sakamoto *et al* 2004). In both cases the goal is to achieve sufficiently deep thermal lesions. In the former case the lesion should be deep enough to completely destroy the tumor, while in the latter the objective is to seal the small vessels in the transection zone (Poon *et al* 2005). We focused on the RF-assisted resection where the thermal lesions should be as deeper as possible in order to facilitate the subsequent transection. About the lesion width, on the one hand it is interesting to keep safe the non ablated tissue as much as possible (i.e. reducing the thermal spread), for instance in the case of partial nephrectomy where the amount of nephrons is critical. On the other hand, it is also important to create a thermal lesion sufficiently wide to coagulate the vessel in the proximity prior to transection, avoiding the intraoperative bleeding.

RF energy is applied to the tissue mostly by a monopolar arrangement between an active electrode and a large conductive patch (dispersive electrode) in contact with the patient's skin. The TissueLink dissecting sealer (Salient Surgical Technologies, Portsmouth, NH, USA) is one of the most widely used electro-surgical devices in hepatic coagulation. Briefly, it is a monopolar electrode cooled by flushing saline through openings in the electrode. This cooling method was previously proposed for RF cardiac ablation in order to obtain deeper lesions and prevent both excessive heating at the electrode-tissue interface and thrombus formation on the electrode (Everett *et al* 2009, Yokoyama *et al* 2006, Demazumder *et al* 2001). In hepatic RF coagulation this cooling method (also known as *saline-linked*) was used to prevent surface charring and keep tissue surface temperature below 100°C (Topp *et al* 2004). However, this does not prevent the temperatures in

the subsurface from rising above 100°C, which can lead to steam formation and expansion and even to disruption of the surface. The steam may be audible as “steam pops”. In fact, undesirable effects such as steam pops, impedance rise and charring of the tissue surface (and in some cases disruption) have been observed in RF heating of cardiac and hepatic tissue (Topp *et al* 2004, Everett *et al* 2009, Yokoyama *et al* 2006) with both open and closed irrigation (Everett *et al* 2009, Yokoyama *et al* 2006). The use of closed-irrigation (or internally cooled) RF electrodes has been proposed not only for RF cardiac ablation (Cooper *et al* 2004) but also for RF-assisted resection of liver, kidney and pancreas (Burdío *et al* 2010, Ríos *et al* 2011, Dorcaratto *et al* 2012) to minimize blood loss during resection.

Saline-linked technology has recently been implemented in a bipolar arrangement in the Aquamantys System (Salient Surgical Technologies, Portsmouth, NH, USA) (Zeh *et al* 2010). In general, bipolar electrodes are composed of two identical electrodes between which RF current flows. This arrangement requires less power than the monopolar configuration to achieve the same coagulating effect and has the additional advantage of not needing a dispersive electrode, thus avoiding the risk of skin burns by poor contact between the skin and the dispersive electrode. But most importantly, the use of bipolar electrodes prevents RF currents flowing through adjacent tissue, thus minimizing the risk of injury to other organs. This is especially important when surgery is performed by the laparoscopic approach in conditions of reduced visibility (Wattiez *et al* 1995).

Devices based on saline-drip, such as open-irrigation RF electrodes, have certain disadvantages when compared to closed-irrigation electrodes: (1) the risk of burning contiguous organs by hot saline; and (2) the saline flow rate is critical for producing the desired haemostatic effect without excessive charring (Sprunger and Herrell 2005). An internally cooled bipolar RF applicator would therefore combine the above-mentioned advantages of the bipolar configuration and would not have the drawbacks associated with open-irrigation RF electrodes. Although some designs have been proposed for internally cooled bipolar RF applicators, such as the Isolator (Atricure, Cincinnati, OH USA), designed to create thermal lesions in cardiac tissue to cure atrial fibrillation (Voeller *et al* 2010), these electrodes had not previously

been considered to coagulate hepatic tissue, in particular to create thermal lesions sufficiently deep for surface RF ablation or as sealing devices during surgical resection. We therefore conducted a feasibility study of a closed-irrigation bipolar RF applicator. The study was based on three complementary methodologies: *ex vivo*, *in vivo* and computational models. Due to their low cost, the *ex vivo* and computational models were used in the first step to check the electrical and thermal performance of the applicator under test. When its ability to create deep lesions had been assessed we then conducted a pilot experimental *in vivo* test to check the results in a pre-clinical scenario. Finally, additional computer simulations that modeled the *in vivo* scenario were conducted to study the effect of the applied voltage and duration on the lesion depth and to determine the potential of the cooled bipolar applicator to coagulate hepatic tissue. These simulations were extended to the case of a smaller applicator especially designed for laparoscopic use.

5.3. Materials and methods

5.3.1. Description of the device

Figure 5.1 shows the proposed device (D1), which consists of two identical electrodes 5 mm in diameter and 25 mm long, separated by a distance of 6 mm. We chose long rather than pointed electrodes (as in the Aquamantys System) since we needed an applicator able to create thermal coagulative necrosis along the transection plane, as achieved by systems based on multiple-electrode arrays (Pai *et al* 2012). Internal cooling was set at a volumetric flow rate of 100 mL/min and a coolant temperature of 5°C. The electrodes were connected to a CC-1 Cosman Coagulation System RF generator (Radionics, Burlington, MA, USA), which delivers a non modulated sinusoidal waveform up to 100 V (rms) to a 100 Ω load at a maximum current of 1 A.

5.3.2. Ex vivo experimental setup

Six lesions were performed on the surface of excised bovine liver (4.5 kg weight, 17°C initial temperature). The collagenous capsule (Glisson's Capsule)

covering the external surface of the liver was removed prior to the RF application. Room temperature was 22°C. Internal cooling was conducted by means of a Model 323 peristaltic pump (Watson Marlow, Wilmington, MA, USA). We analyzed impedance progress during RF heating and the geometry of the lesions created in the tissue after each heat application. Impedance was sampled at 30 Hz and processed by means of Agilent VEE software (Agilent Technologies, Santa Clara, CA, USA). Each lesion was sliced transversally in order to characterize its geometry (see Figure 5.4(a)). The thermal lesion geometry was assessed by the white coagulation zone and its depth (D) and maximum width (W) were quantified (see Figure 5.4(b)). Both parameters were expressed as the mean \pm standard deviation. A Mann-Whitney Test was used to analyze the differences between groups. Data collection and analysis of impedance progress were performed with Matlab[®] (The MathWorks, Natick, MA, USA) and SPSS 17.0 (Chicago, IL, USA), respectively.

5.3.3. In vivo experimental setup

An in vivo pilot study was performed on a Landrace pig (58 kg) obtained from the farm of the Universitat Autònoma de Barcelona (Barcelona, Spain) with the authorization of the Ethical Commission of Animal and Human Experimentation (Spanish Government) and under the control of the Ethical Commission of the Universitat Autònoma de Barcelona (Authorization Number CEAAH 1256). The anesthesia was supervised by a fully trained veterinary staff member. A combination of azaperone and ketamine (4 mg/kg IM and 10 mg/kg IM) was used for initial sedation. Once sedated, intravenous access was obtained by placing a 20G catheter in a marginal ear vein and morphine (0.2 mg/kg IM) and meloxicam 0.2 mg/kg IV) were given as analgesic therapy. Anesthetic induction was performed with propofol (4 mg/kg IV) and maintained with isoflurane (vaporizer setting 2%) and 100% oxygen through a semi-closed circular system (25 mL/kg/min oxygen). Lactated Ringer's solution (10 mL/kg/hour) was administered through the same catheter throughout surgery. Ventilation was controlled using intermittent positive pressure ventilation (SAV 2500 ventilator, B. Braun, Spain) in order to maintain normocapnia. During the surgical process, temperature, heart rate, respiratory

frequency, expired CO₂, arterial pressure, pulse and electrocardiography were monitored by a Datex Ohmeda Cardiocap II monitor. The animal was aseptically prepared for surgery and a cranial laparotomy was performed to access the liver. The four hepatic lobes were exposed and ten RF coagulations were conducted on the liver surface (35°C) using a constant voltage of 50 V (rms) for 60 s. Room temperature was 20°C. Internal cooling was conducted by means of a PE-PM Radionics peristaltic pump (Integra Radionics, Burlington, MA, USA). Impedance progress was registered during RF heating for each lesion. The pig was euthanized after the study by an IV dose of sodium pentobarbital. As in the ex vivo study, liver excision was performed post-mortem in order to assess the lesions.

5.3.4. Computational modeling

Computational models were based on a coupled electric-thermal problem, which was solved numerically using the Finite Element Method (FEM) with COMSOL Multiphysics software (COMSOL, Burlington MA, USA). The governing equation for the thermal problem was the Bioheat Equation (Berjano 2006):

$$\rho c \frac{\partial T}{\partial t} = \nabla \cdot (k \nabla T) + q + Q_p + Q_m \quad (1)$$

where T is temperature, t time, k thermal conductivity, ρ density and c specific heat. The term Q_m is metabolic heat generation and is ignored in the RF of the liver, since it has been shown to be insignificant; and Q_p is heat loss from blood perfusion:

$$Q_p = \rho_b c_b \omega_b (T_b - T) \quad (2)$$

where ρ_b is the density of blood (1000 kg/m³) (Tungjitkusolmun *et al* 2002), c_b the heat capacity of blood (4180 J/Kg·K) (Tungjitkusolmun *et al* 2002), T_b the blood temperature (37°C), and ω_b the blood perfusion coefficient. The term Q_p was only considered in the simulations of the in vivo conditions. For this case, a blood perfusion coefficient of $\omega_b = 3.8 \cdot 10^{-3} \text{ s}^{-1}$ (corresponding to a 60% perfusion level) was considered (Tungjitkusolmun *et al* 2002). The term Q_p was discarded when modeling ex vivo situations. Term q is the heat source from RF power (Joule loss)

which is given by $q = \sigma|\mathbf{E}|^2$, where $|\mathbf{E}|$ is the magnitude of the vector electric field (V/m) and σ the electrical conductivity (S/m). The value of this vector is calculated from $\mathbf{E} = -\nabla\Phi$, where Φ is the voltage (V). The voltage is obtained by solving Laplace's equation, which is the governing equation of the electrical problem:

$$\nabla \cdot (\sigma \nabla \Phi) = 0 \quad (3)$$

At the RF frequencies (≈ 500 kHz) used in RF heating and over the distance of interest (electrical power is deposited within a small radius around the electrode) the biological medium can be considered almost totally resistive, since the displacement currents are much less important than conduction currents. A quasi-static approach is therefore possible to solve the electrical problem (Doss 1982).

Tissue vaporization was modeled by using the enthalpy method (Abraham and Sparrow 2007, Byeongman and Alptekin 2010). This was performed by modifying Equation (1) and incorporating the phase change according to (Pearce *et al* 2005, Yang *et al* 2007):

$$\frac{\partial(\rho h)}{\partial t} = \nabla \cdot (k \nabla T) + q + Q_p + Q_m \quad (4)$$

where h was the enthalpy. For biological tissues, the enthalpy is related to the tissue temperature by followings (Abraham and Sparrow 2007, Zhao *et al* 2007):

$$\rho h = \begin{cases} \rho_l c_l T & 0 < T \leq 99^\circ C \\ \rho h(99) + h_{fg} C \frac{(T - 99)}{(100 - 99)} & 99 < T \leq 100^\circ C \\ \rho h(100) + \rho_g c_g (T - 100) & T > 100^\circ C \end{cases} \quad (5)$$

where ρ_i and c_i were tissue density and specific heat of liquid tissue ($i=l$) and the post-phase-change tissue ($i=g$), respectively; h_{fg} was the latent heat and C the tissue water content. We considered a value of latent heat of $2.162 \cdot 10^9$ J/m³, which corresponds to the product of the water vaporization latent heat and the water density at 100°C, and a tissue water content of 0.68 inside the liver tissue (Pätz *et al* 2009).

Figure 5.2 shows the physical situation modeled and the proposed computational model, which represents the device over a fragment of hepatic tissue. Since there is a symmetrical plane, the model only includes half of the electrode-tissue set. The electrode, which has the same diameter as the device used in the experiments (Figure 5.1), was assumed to be inserted in the tissue to a depth of 0.5 mm and was separated from the symmetrical plane by 3 mm (6 mm inter-electrode distance).

Tissue dimensions R and H were estimated by means of a convergence test in order to avoid boundary effects, using as control parameter the value of the maximal temperature achieved in the tissue (T_{\max}) after 60 s of heating. We first considered a tentative spatial (i.e. minimum meshing size) and temporal resolution. To determine the appropriate values of R and H , we conducted a computer analysis by increasing the value of these parameters by equal amounts. When the difference between T_{\max} and the same parameter in the previous simulation was less than 0.5%, we considered the former values of R and H to be adequate. We then determined adequate spatial and temporal resolution by means of other convergence tests using the same control parameter as in the previous test. Discretization was spatially heterogeneous: the finest zone was always the electrode-tissue interface, since it is known that this has the largest voltage gradient and hence the maximum value of current density. In the tissue, grid size was increased gradually with distance from the electrode-tissue interface. The optimum spatial discretization was achieved by refining the mesh in this zone so that T_{\max} was within 0.5% of the value obtained from the previous refinement step. With an adequate spatial resolution achieved, we decreased the time step until T_{\max} was within 0.5% of the value obtained from the previous time step.

The thermal and electrical characteristics of the model elements (electrode and tissue) are shown in Table 5.1 (Pätz *et al* 2009, Berjano *et al* 2006, Duck 1990). The electrical and thermal conductivity were temperature-dependent functions. For electrical conductivity we considered an exponential growth of +1.3%/°C and +1.7%/°C up to 100°C for the *ex vivo* and *in vivo* model, respectively. These values were chosen since they provided the best fit for the impedance progress (initial

decreasing slope) of the experimental and computational results. Between 100 and 105°C, σ was kept constant and then decreased linearly by 2 orders for five degrees (Byeongman and Alptekin 2010). Thermal conductivity grew linearly +1.5%/°C up to 100°C, and from then on was kept constant (Berjano 2006).

Figure 5.3 shows the electrical and thermal boundary conditions. For the electrical boundary conditions (Figure 5.3(a)), a constant voltage of 25 V was applied to the electrode and 0 V on the symmetry plane, which was equivalent to 50 V (rms) in the experimental setup. A null electrical current was assumed on surfaces at a distance from the electrode and on the tissue-ambient and electrode-ambient. Impedance value was calculated from the ratio of applied voltage to total current, which was calculated as the integral of the current density (A/m^2) over the symmetry plane, where current density is $\mathbf{J} = \sigma \mathbf{E}$.

For the thermal boundary conditions (see Figure 5.3(b)), a null thermal flux was used on the symmetry plane. The temperature on surfaces at a distance from the electrode (T_{tissue}) was 17°C and 35°C for modeling the ex vivo and in vivo situations, respectively. The effect of free convection at the tissue-ambient and electrode-ambient interfaces was taken into account using a thermal transfer coefficient (h_e) of 20 $\text{W}/\text{m}^2\text{K}$. Room temperature (T_e) was 22°C and 20°C, respectively, for modeling the ex vivo and in vivo situations. The thermal boundary condition of convective coefficient (h_i) was applied to the inner electrode in order to model the cooling effect of the circulating fluid. The value of h_i for laminar flow (Burdío *et al* 2009) was calculated using:

$$Nu = \frac{h_i L}{k_f} \quad (6)$$

where Nu is the (dimensionless) Nusselt number, k_f the thermal conductivity of circulating fluid ($\text{W}/\text{m}\cdot\text{K}$), L the length of the heated area (parallel to the direction of the flow), which was fixed at 25 mm (length of electrode in contact with the tissue, see Figure 5.1 (b)). The average Nusselt (\overline{Nu}) can be estimated from the equation:

$$\overline{Nu} = 0.664(\text{Re}^{1/2})(\text{Pr}^{1/3}) \quad (7)$$

where Re is the Reynolds number and Pr the Prandtl number (both dimensionless). Equation (7) is valid for $Re < 5 \cdot 10^5$. These numbers are calculated from the equations:

$$Re = \frac{\rho_f u L}{\mu} \quad (8)$$

$$Pr = \frac{c_f \mu}{k_f} \quad (9)$$

where ρ_f is the density of circulating fluid (kg/m^3), μ the dynamic viscosity ($\text{N}\cdot\text{s/m}$), c_f the specific heat at constant pressure ($\text{J/kg}\cdot\text{K}$) and u the velocity of the flow (m/s) calculated as:

$$u = \frac{F}{60 \cdot 1000 \cdot A_t} \quad (10)$$

where F is the flow rate of the circulating fluid and A_t the cross-sectional area of the tube $= \pi(0.0025)^2 = 1.9635 \cdot 10^{-5} \text{ m}^2$. We obtained a value for h_i of $1537 \text{ W/m}^2\cdot\text{K}$ (flow rate of 100 mL/min). The characteristics of the circulating fluid were considered to be those of water at 37°C : $k_f = 0.63 \text{ W/m}\cdot\text{K}$, $\rho_f = 999.4 \text{ kg/m}^3$, $\mu = 6.9 \cdot 10^{-4} \text{ N}\cdot\text{s/m}$, and $c_f = 4174 \text{ J/kg}\cdot\text{K}$. We considered a coolant temperature of 5°C .

In each simulation we obtained the impedance progress for 60 s of RF heating and the lesion zone dimensions created in the tissue. These variables were used to compare the computational and experimental results. In order to conduct this comparison we adjusted the initial impedance of the tissue in the computational model to the mean value obtained in each experimental study. This was done by varying the initial tissue electrical conductivity (σ_0) to achieve the same initial impedance as in the experiments (see Table 5.1).

The lesions were assessed by the Arrhenius damage model (Chang 2010, Chang and Nguyen 2004), which associates temperature with exposure time using a first order kinetics relationship:

$$\Omega(t) = \int_0^t A e^{\frac{-\Delta E}{RT}} dt \quad (11)$$

where $\Omega(t)$ is the degree of tissue injury, R the universal gas constant, A the frequency factor (s^{-1}), and ΔE the activation energy for the irreversible damage reaction (J/mol). The parameters A and ΔE are dependent on tissue type; for the liver we considered those proposed by Jacques *et al* 1996: $A = 7.39 \cdot 10^{39} s^{-1}$ and $\Delta E = 2.577 \cdot 10^5 J/mol$. We employed the thermal damage contour $\Omega = 1$ which corresponds to a 63% percent probability of cell death. The change in the perfusion term with temperature was taken into account when modeling the in vivo condition. We considered the cessation in tissue perfusion ($Q_p = 0$) for $\Omega > 1$ (under which tissue coagulation is assumed to occur) (Chang 2010).

Finally, after comparing the thermal lesions computed from the models with the experimental values, we conducted an additional set of simulations using the computational model of the in vivo conditions and varying the applied voltage and duration values. The aim here was to explore the effect of these parameters on lesion dimensions from a computational point of view. We also repeated these simulations by considering a small applicator (D2) with 3 mm diameter electrodes separated by a distance of 4 mm, which would allow it to be passed through a trocar in laparoscopic surgery.

5.4. Results

After the convergence tests conducted with the computational models, we obtained a value of $R = H = 50$ mm (tissue dimensions), a grid size of 0.115 mm in the finest zone (electrode-tissue interface) and a step time of 0.05 s. The computational model had nearly 2,500 triangular elements. Figure 5.4(b) shows the side views of the thermal lesions created experimentally for the ex vivo and in vivo conditions. Figure 5.4(c) shows temperature distributions from the computer simulations for the ex vivo and in vivo conditions. As expected, the lesions are mainly limited to the area between the electrodes, especially on the surface tissue. This is especially noticeable in Figure 5.4(a), where the surface view of a lesion (ex vivo) shows a very limited contour along the entire length of the electrodes.

Table 5.2 shows the lesion dimensions for both ex vivo and in vivo experimental conditions and the values estimated from the computer simulations in

the corresponding conditions. In general, the computational model tended to overestimate lesion width by 45% in the ex vivo case and up to 100% in the in vivo case. In contrast, the computational estimation of the lesion depth was more accurate in both cases, by around 13% ex vivo and 45% in vivo.

In the ex vivo case a strong correlation was found between the initial impedance of the hepatic tissue and the lesion dimensions: $R^2 = 66\%$ for depth and 77% for width, but this correlation was found to be very weak ($<15\%$) in the in vivo case.

Figure 5.5 shows impedance progresses during RF heating in the ex vivo (Figure 5.5(a)) and in vivo study (Figure 5.5(b)). The initial impedance was different in both cases ($231.13 \pm 9.60 \Omega$ and $90.10 \pm 8.56 \Omega$ respectively) and progress was also slightly different. Ex vivo impedance progressively decreased during the entire period while in vivo impedance fell rapidly in the first 10 s and then increased at a slower rate until the end-point. In one case of the in vivo setup there was an abrupt impedance rise (roll-off) at 45 s. Figure 5.5 also shows the impedance progress obtained from the computational models (solid lines), which shows that in general there is good agreement between the computational and experimental results.

Finally, Figure 5.6 shows the depth of lesions estimated from the computer simulations of in vivo conditions for the applicator under test (D1) and for the smaller design (D2) when changing the applied voltage (50 - 100 V) and duration (60 - 300 s). The results indicate that the heating period has a minimum impact on lesion depth: D1 was seen to increase from 9.62 mm to 17.13 mm and D2 from 9.15 mm to 14.48 mm when the time was increased from 60 s to 300 s. In contrast, when the time was kept at 60 s, the applied voltage did not have a significant influence on lesion depth, which in fact slightly decreased from 9.62 mm to 7.76 mm for D1 and from 9.15 mm to 6.66 mm for D2 when voltage was raised from 50 V to 100 V. The low impact of the applied voltage on lesion dimensions could be due to the fact that increasing the voltage caused a sudden increase of impedance (roll-off), at which time the temperature of the tissue around the electrode reached 100°C. This could have prevented the lesion from going deeper. In this respect, Figure 5.7 shows the in vivo impedance progresses and tissue temperature distributions computed for the

applicator under test by raising the applied voltage from 50 to 100 V. We observed that roll-off occurred at a specific time for each applied voltage and at this time the temperature of the tissue around the electrode was 100°C: 40 s, 15 s and 9 s for a voltage of 65V, 80 V and 100 V, respectively.

5.5. Discussion

This study was conducted to assess the capacity of a bipolar cooled RF applicator to coagulate hepatic tissue and especially to quantify the lesion depths created. We used three complementary methodologies: ex vivo set up, in vivo experiments and computational modeling.

The results of the computer simulations were compared to the experimental results to assess the accuracy of the computational models. In general, we observed a tendency in the computer simulations to overestimate the lesion dimensions. However, we also found good agreement between the computational and experimental results of impedance progress, which suggests that the disagreement could have been due to the method used to assess the thermal lesion. The experimental lesions were assessed by the white coagulation zone. Prior to the experimental ex vivo study we evaluated the relationship between the color change in liver samples immersed in hot water, water temperature, and immersion time. The samples were heated from 50 to 75°C for times from 15 to 60 s, as in (Panescu *et al* 1995, Dadd *et al* 1996). We observed that the tissue did not turn white until the water temperature reached 70°C (González-Suárez *et al* 2011). Since it is known that temperatures around 50°C produce coagulative thermal necrosis, we can state that the experimental lesion dimensions correspond approximately to the boundary of the 70°C isotherm, while the lesion dimensions from the computer simulations using the tissue damage function include a higher amount of tissue at temperatures over 50°C. For this reason the lesions estimated from the computational models possibly give a truer representation of the dimensions than the white coagulation contours. Taking the above into account, we consider that the proposed computational model would be sufficiently accurate if used to study other issues from a computational point of view.

In practical terms, the experimental results suggest that by using the closed irrigation RF bipolar electrode, it is possible to achieve in vivo lesions with a depth ≈ 7 mm. If the computational model gives a more accurate representation of lesion depth, the value could be around 9 mm. As far as we know, no data have been reported on the lesion depth achieved by the Aquamantys bipolar system, although there are indications that it is typically less than 2 mm (Rosenberg 2007). The cooled bipolar applicator tested in this study produces deeper lesions, which could be due to the size of the electrode used (5 mm vs. 3.48 mm in the Aquamantys Model 6.0) and the distance between electrodes (6 mm vs. 2.53 mm). These dimensional differences would undoubtedly have an influence on the results, as would the different technologies they use: open vs. closed irrigation. Previous comparative studies on RF cardiac ablation have not been unanimous in their findings; while some suggest there are no differences between open and closed irrigation at the same power settings (Petersen *et al* 2004), others maintain that there are no differences for power levels higher than 20 W (Everett *et al* 2009, Yokoyama *et al* 2006) but that closed irrigation produces deeper lesions at low power setting (< 20 W) (Everett *et al* 2009). Future studies should be conducted to compare the lesion depths created by both systems in hepatic tissue.

An experimental study on cardiac tissue using the Isolator device (Atricure, Cincinnati, OH USA) based on closed irrigation bipolar RF electrodes reported a mean lesion depth of 5.3 ± 3.0 mm (Voeller *et al* 2010). This shows once again that lesion characteristics are highly dependent on the electrode design (diameter and distance between electrodes), as well as other factors such as contact pressure, power delivering protocol (including power setting), so that a direct comparison with our results is difficult. However, our findings suggest that the applicator studied would be useful for creating sufficiently deep thermal lesions in hepatic tissue to assist in sealing small vessels during surgical resection, or producing a long thermal lesion along the transection plane in preparation for cutting with a cold scalpel.

It should be emphasized that our aim was not to determine the factors affecting the incidence of steam popping or impedance rise (as in Gnerlich *et al* 2009), i.e. we did not search for the optimum combination of applied voltage and

duration. In this respect, the results from additional computer simulations in which these two parameters were varied suggest that lengthening the duration could extend lesion depth to 17 mm. They also suggest that raising the applied voltage will not increase lesion depth. In this regard, we found that at higher voltages the tissue around the electrode reaches $\approx 100^{\circ}\text{C}$ and causes an abrupt increase of impedance at a specific time. This interrupts the flow of RF current and consequently limits the size of the lesion. We therefore consider that a value around 50 V would be the optimum.

From a clinical point of view, the applicator tested here is too large to be used in a laparoscopic approach and hence can only be employed in open surgery for both liver resection and surface tumor ablation. However, the computational model proposed here could be useful for exploring the suitability of other designs for use with a trocar in laparoscopic surgery. In this respect, the computational results computed for different values of applied voltage and duration were similar to previous results. A lesion depth ≈ 14 mm could be achieved when the duration is increased. On the other hand, simply raising the applied voltage did not provide deeper lesions.

This study has certain limitations. Firstly, the computational model was two-dimensional, while the experimental models were obviously three-dimensional. The comparison between the computational and experimental results suggests that this limitation is not highly significant, at least for the durations used here, since the edge effect observed in the early stages (when heating is mainly confined to the ends of the electrodes) seems negligible for heating times longer than 60 s. Also, the *in vivo* computer simulations considered only one value for tissue perfusion, although the actual perfusion rate in each lesion zone was unknown under the specific *in vivo* experimental conditions. In fact, it would be possible to find a better correlation between computational and *in vivo* experimental results by finding an optimum value of blood perfusion coefficient.

Finally, the differences between the *ex vivo* and *in vivo* results could be due not only to the different initial impedance and temperature values, but possibly also to whether or not the Glisson's capsule had been previously removed. The electrical

and thermal effect of this layer on lesions should be made the subject of further research. Although its clinical impact seems low, its presence could have caused the steam pops observed in our in vivo study, due to steam accumulating between the hepatic tissue and capsule during heating.

5.6. Conclusions

The experimental results suggest that the cooled bipolar RF applicator tested in this study could create lesions with a depth around 7 mm under in vivo conditions. This value could be considered to be optimum for RF-assisted hepatic resection. The thermal lesion is mainly confined to the area between the electrodes, which would make it possible to control lesion width by selecting a specific applicator design. The comparison between the experimental and computational results suggests that the computational model could be useful for further studies of the performance of this device.

Table 5.1. Thermal and electrical characteristics of the elements employed in the computational modeling (Data from (Pätz *et al* 2009, Berjano *et al* 2006, Duck 1990)).

Element/Material		σ (S/m)	k (W/m·K)	ρ (kg/m ³)	c (J/kg·K)
Electrode		$7.4 \cdot 10^6$	15	8000	480
Liver	Liquid phase	σ_o^*	0.502**	1080	3455
	Gas phase			370	2156

σ , electric conductivity; k , thermal conductivity; ρ , density; and c , specific heat.

* σ_o : assessed at 17°C and adjusted to achieve the same initial impedance as in the experiments: 0.37 and 0.71 S/m for ex vivo and in vivo, respectively. ** Assessed at 37°C.

Table 5.2. Lesions dimensions created by the internally cooled bipolar applicator under ex vivo and in vivo experimental conditions together with the values estimated from computer simulations for the same conditions.

Condition	Methodology	Depth (mm)	Width (mm)
Ex vivo	Computational	4.54	11.19
	Experimental (n = 6)	4.03 ± 0.14	7.67 ± 0.41
In vivo	Computational	9.62	22.20
	Experimental (n = 10)	6.85 ± 1.25	10.90 ± 1.22

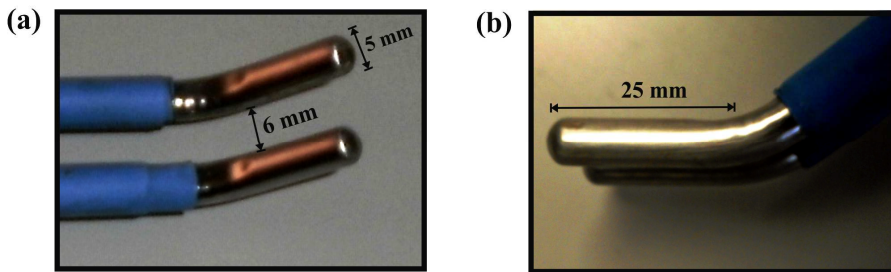


Figure 5.1. Top (a) and side (b) views of the internally cooled bipolar applicator proposed to coagulate hepatic tissue.

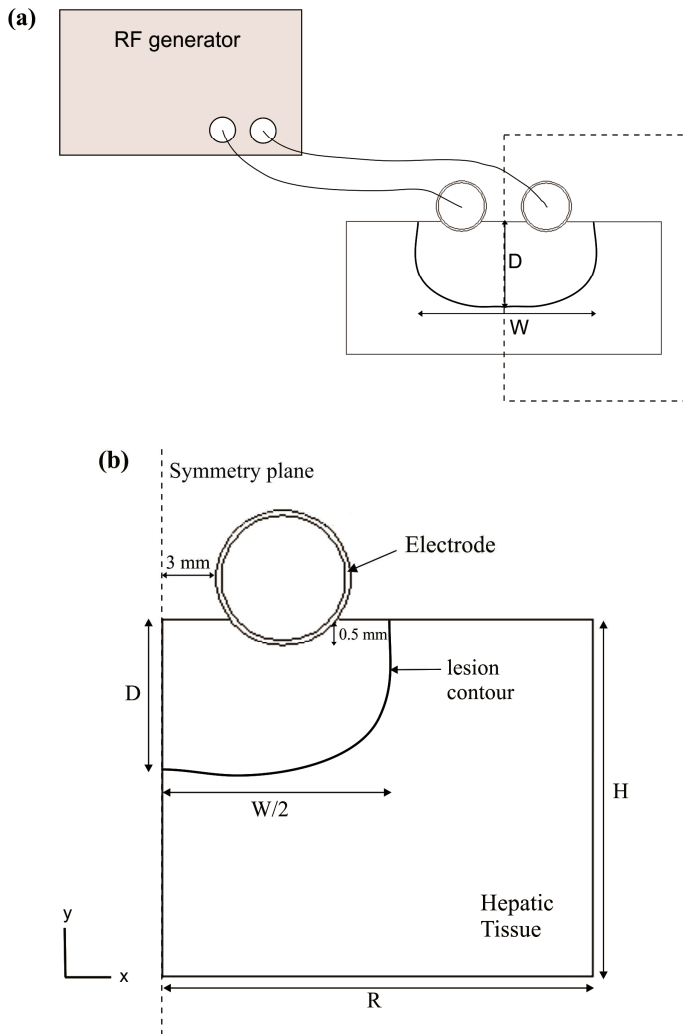


Figure 5.2. (a) Physical situation considered in the study. The dashed rectangle indicates the region considered in the computational model. (b) Computational model proposed (out of scale). R and H : dimensions of the hepatic tissue. The inner and outer electrode diameters are 4.5 and 5 mm, respectively. Since there is a symmetrical plane, the model only includes half of the electrodes-tissue set. Lesion depth (D) and width (W) were assessed by an Arrhenius damage model (see text for more details).

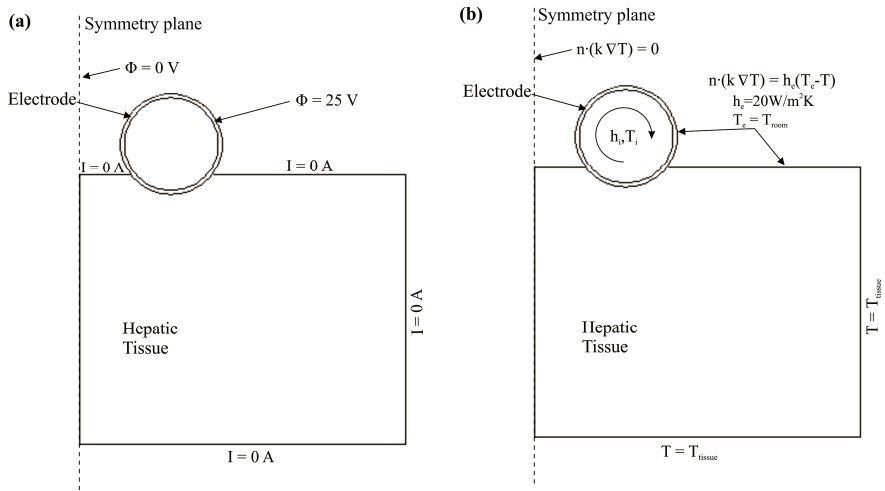


Figure 5.3. Electrical (a) and thermal (b) boundary conditions of the computational model.

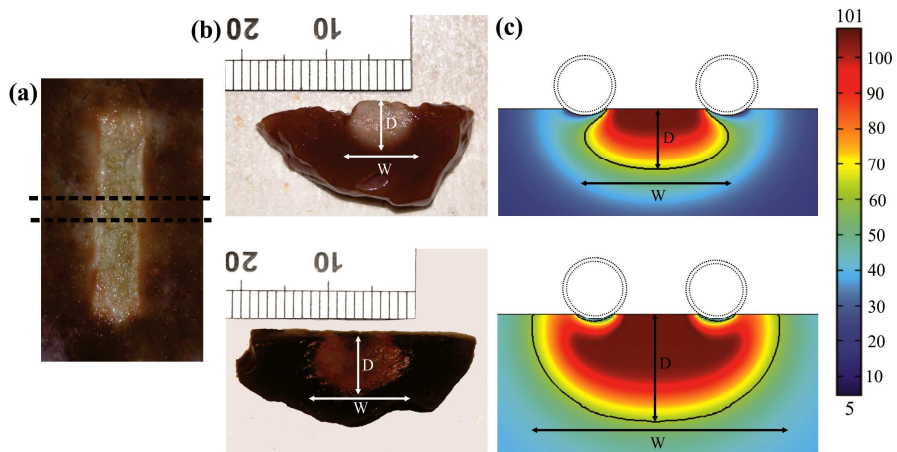


Figure 5.4. Thermal lesions created after 60 s of RF heating at 50 V (rms), considering a flow rate of 100 mL/min and a coolant temperature of 5°C. (a) Surface view of lesion created in the ex vivo model, (b) side views of lesions created in the ex vivo (top) and in vivo (bottom) models. (c) Temperature distributions from computer simulations of the ex vivo (top) and in vivo (bottom) conditions (scale in °C). The lesions were characterized by the depth (D) and maximum width (W) parameters. Experimental lesions were assessed by the white coagulation zone contour and in the computer simulations by an Arrhenius damage model (the solid black contour corresponds to $\Omega = 1$).

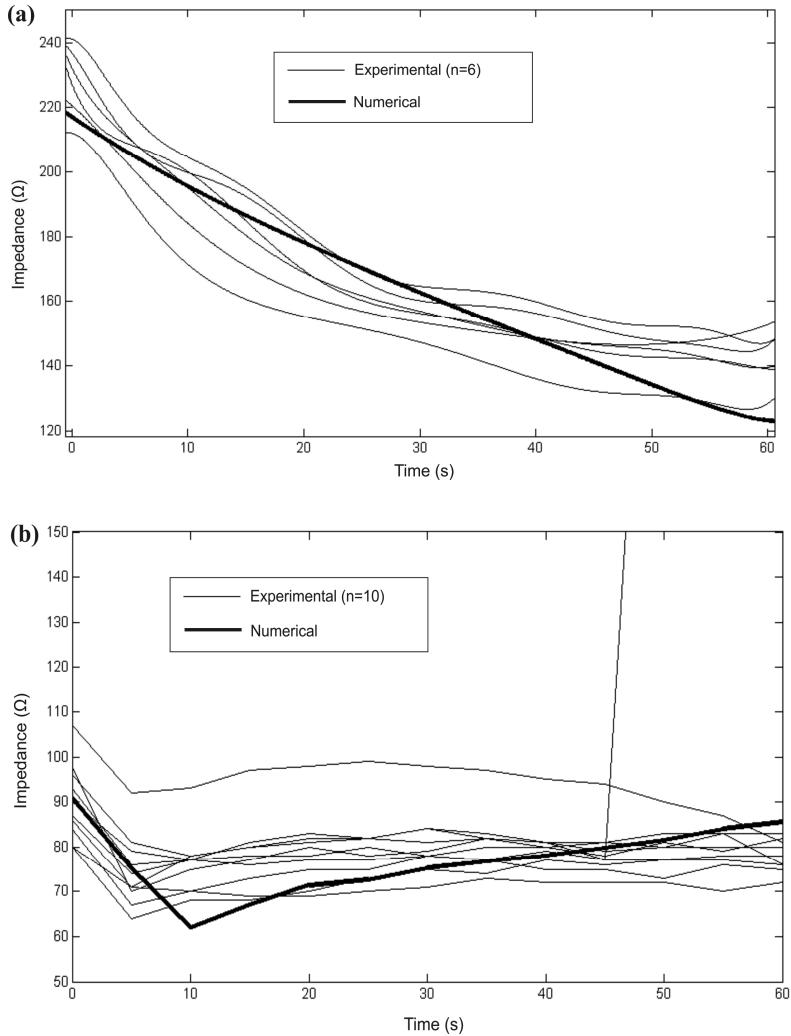


Figure 5.5. Impedance progresses during RF heating in the ex vivo (a) and in vivo study (b). The solid lines show the results of computer simulations of the corresponding conditions. Both cases (ex vivo and in vivo) consider a flow rate of 100 mL/min and a coolant temperature of 5°C. Note that an in vivo experimental case showed an impedance rise (roll-off) at 45 s.

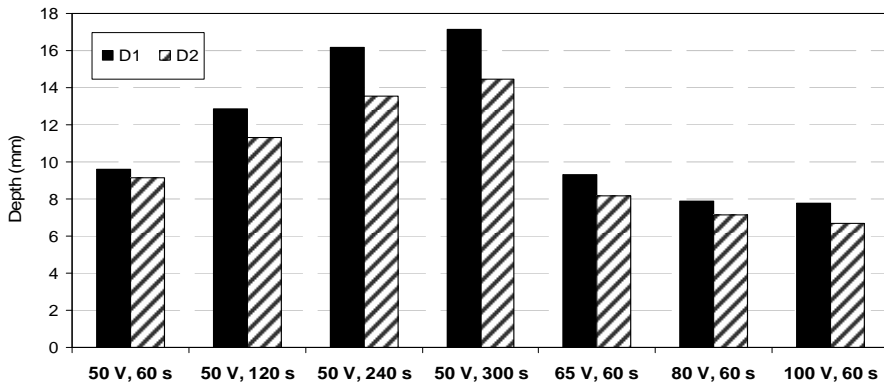


Figure 5.6. Lesion depths estimated from computer modeling of in vivo conditions for the applicator under test (D1) and the smaller design (D2) when changing applied voltage (between 50 and 100 V) and duration (between 60 and 300 s). D1 and D2 are applicators with 5 and 3 mm diameter electrodes and separated by a distance of 6 and 4 mm, respectively.

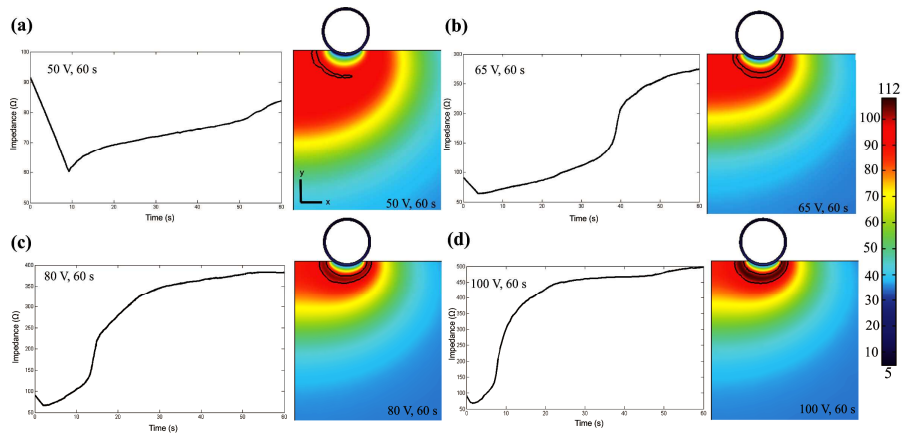


Figure 5.7. Impedance progresses and tissue temperature distributions computed for in vivo conditions for the applicator under test while changing the voltage (between 50 and 100 V) for a time of 60 s. The contour line corresponds with the 100°C isotherm plotted at the instant at which roll-off occurs. Scale in $^{\circ}\text{C}$.

Chapter 6

Could the heat sink effect of blood flow inside large vessels protect the vessel wall from thermal damage during RF-assisted surgical resection? A computer modeling and an in vivo experimental study

6.1. Abstract

Purpose: To assess whether the heat sink effect inside a large vessel could protect the vessel wall from thermal damage close to an internally cooled electrode during RF-assisted resection.

Materials and methods: Three computational models were built and we first compared three mathematical ways of modeling the heat sink effect of blood flow: 1) constant heat transfer at the tissue-vessel interface (h_v), 2) temperature-dependent h_v , and 3) advection heat method. Simulations were then carried out to study the effect of different factors such as device-tissue contact, vessel position and vessel-device distance (D) on temperature distributions and thermal lesion dimensions near the large vessel. In vivo experiments were also conducted to validate the computational results.

Results: The three methods of modeling blood flow provided a similar temperature distribution around the vessel. The advection heat method was chosen for the study. The shape of the thermal lesion was significantly modified by the heat sink effect around the vessel in all the cases considered. Thermal damage to the vessel wall was inversely related to the vessel-device distance (D). It was also more pronounced when the device-tissue contact surface was reduced or when the vessel was parallel to the device or perpendicular to its distal end, the vessel wall being damaged at $D \leq 4$ and 4.25 mm. The geometries of lesions around the vessels in the experiments were in agreement with the computational results.

Conclusions: The experimental and computational results suggest that the heat sink effect could protect the vessel wall for $D \geq 7.4$ mm. The computer simulations also predicted that a large vessel wall (such as the portal vein) would not be damaged for $D \geq 5$ mm.

6.2. Introduction

Surgical devices based on monopolar radiofrequency (RF) energy are usually employed during resection to thermally coagulate tissue and minimize blood loss. The rationale is to apply RF power to seal small vessels in the transection plane (Poon *et al* 2005). Some of these devices are based on an irrigated electrode, such as the TissueLink dissecting sealer (Salient Surgical Technologies, Portsmouth, NH, USA), which infuses saline into the tissue through openings (Poon *et al* 2005), while others are based on an internally cooled electrode (Burdío *et al* 2010), such as the Coolinside device (Apeiron Medical, Valencia, Spain). In both designs, the electrode is cooled to prevent surface charring and keep the temperature on the device-tissue interface below 100°C (Topp *et al* 2004).

Creating deep thermal lesions, which is clearly beneficial for sealing small and medium sized vessels in the transection plane, can be less effective when the device is used near large vessels. Acute and delayed portal vein thrombosis as well as injury to the hepatic artery and bile duct have been observed following radiofrequency ablation near the liver hilum, which can lead to major morbidity

such as bile stenosis and liver abscesses (Tepetes 2008, Marchal *et al* 2006). As such, some surgeons prefer using ultrasonic dissectors to remove the tissue around these vessels in order to reduce the risk of thermal damage, since ultrasonic dissectors have a low penetration depth and minimal lateral energy spread (Sutton *et al* 2010). However, we hypothesize that the simple heat sink effect of the blood flow inside the vessel could itself reduce thermal damage. To confirm this hypothesis, we planned computer modeling and *in vivo* experiments to assess the lesion dimensions in hepatic tissue thermally heated by an internally cooled electrode placed near a large vessel.

Previous studies have modeled the heat sink effect of large vessels in the proximity of a tumor ablated by RF currents (Haemmerich *et al* 2003b, Chen and Saidel 2009, Dos Santos *et al* 2008, Consiglieri *et al* 2003, Consiglieri 2012, Antunes *et al* 2012, Huang 2013). The heat sink effect of the blood flow inside the vessel was modeled by different methods: 1) a constant heat transfer coefficient (h_v) at the vessel-tissue interface (Haemmerich *et al* 2003b, Chen and Saidel 2009, Shah *et al* 2005); 2) a temperature-dependent h_v (Dos Santos *et al* 2008, Consiglieri *et al* 2003, Consiglieri 2012); and 3) advection heat method (Antunes *et al* 2012, Gopalakrishnan 2002, Incropera *et al* 2006). The aim of these studies was to determine how the heat sink effect distorted coagulation volume during RF ablation. Our goal was somewhat different: to study how the heat sink effect could protect the vessel wall in the proximity of an RF-assisted resection device. Although some previous computer modeling studies (Chen and Saidel 2009, Peng *et al* 2011) have considered vessel-wall thickness (<0.5 mm) as negligible as compared to its diameter, in the present study it was crucial to consider this factor in order to assess whether the vessel wall had been damaged by RF heating.

The objectives of the study were: 1) to study temperature distributions and thermal lesion dimensions around a large vessel next to a transection plane coagulated by RF energy for different positions and distances of the vessel from an internally cooled RF electrode; and 2) to validate the computer results by means of an *in vivo* experimental study. The results were expected to provide information on the utility of blood flow as a thermal protection mechanism.

6.3. Materials and methods

6.3.1. Description of the RF-assisted device

We considered a RF-assisted resection conducted by an internally cooled 8 mm diameter Coolinside electrode (Apeiron Medical, Valencia, Spain) which is intended to coagulate and dissect hepatic parenchyma by a laparotomy approach (Burdío *et al* 2010). Coagulation was performed by the blunt proximal tip and dissection by an 8 mm long blade attached to the distal tip, as shown in Figure 6.1.

6.3.2. Computer modeling

First, convergence tests were conducted to obtain the optimum dimensions, grid size, and time step values (Section 4.4.1). Secondly, we conducted computer simulations to compare the thermal performance of the three proposed methods to model the cooling effect of the blood inside the vessel (Section 4.4.2). And thirdly, (Section 4.4.3), we simulated: 1) the progress of the temperature distributions during heating; 2) the effect on temperature of vessel distance and position with respect to the electrode; and 3) the effect of the electrode/tissue contact surface.

The numerical model was based on a coupled electric-thermal problem, which was solved numerically using the Finite Element Method (FEM) with COMSOL Multiphysics software (COMSOL, Burlington, MA, USA). The governing equation for the thermal problem was the Bioheat Equation (Pennes 1948):

$$\rho c \frac{\partial T}{\partial t} = \nabla \cdot (k \nabla T) + q + Q_p + Q_m \quad (1)$$

where ρ is density (kg/m^3), c specific heat ($\text{J/kg}\cdot\text{K}$), T temperature ($^{\circ}\text{C}$), t time (s), k thermal conductivity ($\text{W/m}\cdot\text{K}$), q the heat source caused by RF power (W/m^3), Q_p the heat loss caused by blood perfusion (W/m^3) and Q_m the metabolic heat generation (W/m^3), which was considered negligible in comparison with the other terms (Berjano 2006).

Tissue vaporization was modeled by the enthalpy method (Abraham and Sparrow 2007, Byeongman and Alptekin 2010) which incorporates the phase change of the tissue in Equation (1) according to (Pearce *et al* 2005, Yang *et al* 2007):

$$\frac{\partial(\rho h)}{\partial t} = \nabla \cdot (k \nabla T) + q - Q_p \quad (2)$$

where h is enthalpy. For biological tissues, enthalpy is related to tissue temperature by the following expression (Abraham and Sparrow 2007, Zhao *et al* 2007):

$$\rho h = \begin{cases} \rho_i c_i T & 0 < T \leq 99^\circ C \\ \rho h(99) + h_{fg} C \frac{(T - 99)}{(100 - 99)} & 99 < T \leq 100^\circ C \\ \rho h(100) + \rho_g c_g (T - 100) & T > 100^\circ C \end{cases} \quad (3)$$

where ρ_i and c_i is the tissue density and the specific heat of liver tissue before phase-change ($i=l$) and post-phase-change ($i=g$), respectively; h_{fg} is the latent heat and C the tissue water content. We considered a latent heat value of $2.162 \cdot 10^9 \text{ J/m}^3$, which corresponds to the product of the water vaporization latent heat and the water density at 100°C , and a tissue water content of 0.68 inside the liver tissue (Pätz *et al* 2009).

The distributed heat sink effect of the microvascular perfusion was included in the tissue considering as (Pennes 1948):

$$Q_p = \alpha \rho_b c_b \omega_b (T_b - T) \quad (4)$$

where ρ_b is blood density, c_b blood specific heat, T_b blood temperature (37°C), α tissue state coefficient which ranges from 0-1, depending on the local level of tissue damage (Chang and Nguyen 2004, Chang 2010), and ω_b blood perfusion coefficient (s^{-1}). In our study, the value of the blood perfusion coefficient in liver tissue (Tungjitkusolmun *et al* 2002) was $\omega_b = 6.4 \cdot 10^{-3} \text{ s}^{-1}$. The thermal damage of the tissue was assessed by the Arrhenius equation (Chang and Nguyen 2004, Chang 2010), which associates temperature with exposure time using a first order kinetics relationship:

$$\Omega(t) = \int_0^t A e^{\frac{-\Delta E}{RT}} dt \quad (5)$$

where $\Omega(t)$ is the degree of tissue injury, R the universal gas constant, A the frequency factor (s^{-1}), and ΔE the activation energy for the irreversible damage reaction (J/mol). The parameters A and ΔE for the liver were (Jacques *et al* 1996): $A = 7.39 \cdot 10^{39} s^{-1}$ and $\Delta E = 2.577 \cdot 10^5 J/mol$. We employed the thermal damage contour $\Omega = 1$ (63% probability of cell death). When $\Omega > 1$, tissue coagulation is assumed to occur causing a cessation in tissue perfusion ($\alpha = 0$, $Q_p = 0$) (Chang and Nguyen 2004).

At the RF frequencies (≈ 500 kHz) and over the distance of interest, the biological medium can be considered almost totally resistive and a quasi-static approach is therefore possible to solve the electrical problem (Doss 1982). The distributed heat source q is given by $q = \sigma |\mathbf{E}|^2$, where $|\mathbf{E}|$ is the magnitude of the vector electric field (V/m) and σ is the electrical conductivity (S/m). \mathbf{E} is calculated from $\mathbf{E} = -\nabla\Phi$, where Φ is the voltage (V) obtained by solving Laplace's equation:

$$\nabla \cdot (\sigma \nabla \Phi) = 0 \quad (6)$$

Figure 6.2 show the geometry and dimensions of the three-dimensional model built. It represents a partially isolated metallic electrode placed parallel over a fragment of hepatic tissue and close to a large vessel. The vessel has a 10 mm diameter (b), which is the typical size of the portal vein at the liver hilum (Gray 1990), and a wall thickness of 0.5 mm (Chen and Saidel 2009, Peng *et al* 2011). We initially modeled a vessel with a length L (equal to the Y dimension of the tissue) which is located in the middle, perpendicular and at distance (D) of 5 mm below the device. We considered an insertion depth of 1 mm of the device into the tissue due to the pressure between electrode and tissue. The physical dimensions of the device (Figure 6.2(b)) are those of the actual device shown in Figure 6.1: its metallic part has outer and inner diameters of 8 and 7 mm, respectively (OD_M and ID_M), 30 mm in length (L_M) and a blade 2.5 mm depth (P_B), 0.1 mm thick (T_B) and 8 mm long (L_B); the plastic-covered section is 0.3 mm thick (T_P). The model considered this plastic section to be 45 mm long (L_P). The appropriate tissue dimensions X , Y and Z

($Z = Y/2$) were estimated by means of a convergence test in order to avoid boundary effects (Berjano 2006), using as control parameter the value of the maximal temperature achieved in the tissue (T_{\max}) after 45 s of RF heating. We first considered a tentative spatial (i.e. minimum meshing size) and temporal resolution. To determine the appropriate parameters of X and Y , we increased their values by equal amounts. When the difference in the T_{\max} between consecutive simulations was less than 0.5%, we considered the former values to be adequate. We then determined adequate spatial and temporal resolution by means of similar convergence tests using the same control parameter. Discretization was spatially heterogeneous: the finest zone was always the blade-tissue interface, where the largest voltage gradient was produced and hence the maximum value of current density. In the tissue, grid size was increased gradually with distance from the blade-tissue interface.

The thermal and electrical properties of the model elements (electrode, plastic, blood and liver tissue) are shown in Table 6.1 (Haemmerich *et al* 2003b, Pätz *et al* 2009, Berjano *et al* 2006, Duck 1990, Burdío *et al* 2009). The vessel wall was not modeled separately, since it has similar properties to normal liver tissue (Duck 1990). Liver electrical (σ) and thermal conductivity (k) were temperature-dependent and were defined by piecewise functions: for σ we considered an exponential growth (Pearce *et al* 2005) of 1.5%/°C up to 100°C and then it decreased 4 orders for five degrees (Haemmerich *et al* 2003a); and k grew linearly 0.15%/°C up to 100°C, after which temperature k was kept constant (Byeongman and Alptekin 2010).

Figure 6.3(a) shows the electrical and thermal boundary conditions applied to the model. For the electrical boundary conditions, a constant electrical voltage of 50 V was applied to the metallic part of the device and 0 V to the lower surface of the tissue (mimicking the electrical performance of the dispersive electrode). Although this voltage value is lower than that used clinically (around 100 V for the 8-mm electrode) (Burdío *et al* 2010), it should be remembered that the theoretical model (see Figure 6.2) does not include the patient's entire body, and hence the voltage drop across the body and tissue next to the dispersive electrode is missing.

Null electrical current was used on the surfaces at a distance from the device and on the tissue-ambient and device-ambient interfaces. For the thermal boundary conditions, a constant temperature of 37°C was fixed on the surfaces at a distance from the device (this was also the initial temperature value). The effect of free convection at the tissue-ambient and device-ambient interfaces was taken into account using a thermal transfer coefficient (h_e) of 20 W/m²K and a value of 21°C was considered for ambient temperature (Burdío *et al* 2009). The cooling effect produced by the fluid circulating inside the device was not modeled realistically by means of internal tubes (the device was empty, as shown Figure 6.2(b)), but by a forced thermal convection coefficient (h_i) of 1420 W/m²K and a coolant temperature of 5°C. The value of this coefficient was estimated by using the theoretical calculation of forced convection inside a tube (Burdío *et al* 2009) with an inner diameter of 7 mm and a length of the heated area of 30 mm (ID_M and L_M in Figure 6.2(b), respectively). We considered an internal flow rate of the circulating fluid of 100 mL/min and half of the cross section area of the tube with a value of 1.92×10^{-5} m².

6.3.3. Modeling blood flow

The heat sink effect of the blood flow inside the large vessel was modeled by three different methods: (a) a constant heat transfer coefficient, h_v at the tissue-vessel interface; (b) temperature-dependent h_v ; and (c) advection heat method.

6.3.3.a. Method 1: constant h_v

The thermal effect of the blood flow was modeled by a constant heat transfer coefficient at the tissue-vessel interface, assuming fully developed thermal and hydrodynamic flow (Haemmerich *et al* 2003b), i.e. the entire surface of the vessel was subjected to heat. As in previous studies (Haemmerich *et al* 2003b, Chen and Saidel 2009, Shah *et al* 2005, Peng *et al* 2011), this convective coefficient (h_v) was calculated as:

$$h_v = \frac{Nu k_b}{b} \quad (7)$$

where Nu is the (dimensionless) Nusselt number, k_b blood thermal conductivity (W/m·K) and b the diameter of the vessel (see Figure 6.3(b)). The Nusselt number can be approximated as follows (Haemmerich *et al* 2003b):

$$Nu = 4 + 0.486424 \ln^2 \left(\frac{Re Pr b}{18L} \right) \quad (8)$$

where Pr is the Prandlt number ($Pr = 25$ for blood), L the vessel length (is identical to tissue dimension Y) and Re the (dimensionless) Reynolds number calculated as:

$$Re = \frac{\rho_b u_b b}{\mu} \quad (9)$$

where u_b is the average blood velocity in the vessel, being approximately 0.2 m/s in the portal vein (Cioni *et al* 1992); and μ the viscosity of the blood (Duck 1990), $\mu = 0.0034$ N·s/m². As a result, the convective coefficient is $h_v = 855$ W/m²K.

6.3.3.b. Method 2: temperature-dependent h_v

Unlike in the first method, both vessel-wall temperature and h_v varied during the ablation procedure. Since only a small region of the vessel is heated during the process, the thermal boundary condition is not fully-developed (Dos Santos *et al* 2008, Consiglieri *et al* 2003, Consiglieri 2012). The value of this convective coefficient is calculated as a function of the temperature distribution on the vessel wall, which is updated at each time step and is set as the new convective boundary condition on the vessel wall for the next step (Dos Santos *et al* 2008) (see Eq. (10)). This equation assumes that blood behaves as a Newtonian fluid in large vessels, the blood flow has a laminar Navier-Stokes profile and the vessel geometry is linear (Dos Santos *et al* 2008, Consiglieri *et al* 2003):

$$h_v = \frac{\rho_b c_b u_b (T_o - T_i) b}{(0.25(2T_s + T_o + T_i) - T_m) a} \quad (10)$$

where T_i is the normal inlet blood temperature (37°C), T_o the temperature at the vessel outlet, T_s the maximum temperature of the heated region on the vessel wall, T_m the average temperature between T_i and T_o , a the length of the heated region in the vessel and b the vessel diameter (see Figure 6.3(b)). As in method 1, we considered $u_b = 0.2$ m/s. Based on previous experimental and theoretical studies (Dos Santos *et al* 2008, Consiglieri *et al* 2003, Consiglieri 2012), temperatures T_i and T_o were set at 37 and 37.05°C when the temperature of the vessel wall was 50°C. T_o was evaluated by means of linear interpolation from other vessel wall temperatures (Dos Santos *et al* 2008). Although previous studies (Consiglieri *et al* 2003, Consiglieri 2012) assumed a constant length of heated region in the vessel (exactly one quarter of its cylindrical surface), in reality it also changes during the ablation procedure (Dos Santos *et al* 2008). In fact, at the initial time, there is no heated region in the vessel, i.e. $a = 0$ mm ($t = 0$ s). We therefore fixed $h_v = 0$ W/m²K in order to avoid computational problems (the term a is in the denominator of Eq. (10)). The value of a in each time step was calculated as in a previous work (Dos Santos *et al* 2008).

6.3.3.c. Method 3: advection heat method

The heat diffusion produced by the blood flow was simulated as a moving liquid (Antunes *et al* 2012, Gopalakrishnan 2002) by including the following term called advection term (Incropera *et al* 2006) on the right hand of Eq.(1), which represents the heat loss due to blood flow:

$$- \rho_b c_b \mathbf{u}_b \cdot \nabla T \quad (11)$$

where $\mathbf{u}_b(x, y, z)$ is the blood velocity field in the vessel (m/s), which in our study is in direction-y when the vessel is perpendicular to the device, as shown in Figure 6.2(a). Since the blood flow is in this direction, it is not possible to consider half of the model. In order to make a comparison with the previous methods, we considered the same blood flow velocity, $\mathbf{u}_b = 0.2 \hat{y}$ m/s.

6.3.4. Comparison of blood flow models

The temperature distribution in the vessel and the geometry of the thermal lesion around the vessel after RF heating was obtained for each model. We proposed a new procedure to quantify the distances and the area between the thermal lesion and the vessel to assess whether the wall had been damaged by the RF heating. Only one previous study has measured the central distance between the RF lesion and the vessel (Haemmerich *et al* 2003b). In the present study we not only quantified this distance, but also the transverse distances between the ends of the RF lesion and the vessel according to an angle θ , as well as some intermediate distances, as shown in Figure 6.4(a). These distances were then plotted on a graph according to the value of θ , to obtain the area under the curve between d_1 and d_9 (see Figure 6.4(b)). The thermal damage in the vessel wall was assessed by parameter β , which is the arc of the damaged vessel obtained by the intersection of the lesion curve with vessel wall thickness, as shown in Figure 6.4(b). A vessel wall thickness of 0.5 mm was considered (Chen and Saidel 2009, Peng *et al* 2011), which is the maximum wall thickness of the portal vein.

6.3.5. Thermal modeling

After choosing a blood flow modeling method, we conducted simulations to study the effect of different factors on the temperature distributions and the shape of the thermal lesion around the vessel. Although in clinical practice the entire device is placed over the target tissue most of the time, i.e. its entire metallic length (L_M in Figure 6.2(b)) with the blade inserted in the tissue (Burdío *et al* 2010), the surgeon can also choose to first treat the target tissue with the proximal part only (see Figure 6.1) to create a coagulation before placing the blade on the tissue (Ríos *et al* 2011). In this case the contact surface is much smaller than in the case of total contact. In the present study we considered these two relative positions of the electrode.

In the case of total contact between electrode and tissue, we considered two relative vessel/electrode positions: perpendicular and parallel. In the case of the parallel position, the portal vein was the same length as the tissue's dimension X . In

the perpendicular vessel position, we considered three relative positions of the vessel under the electrode: central, proximal and distal. In the case of proximal contact only, at an angle of 15° between electrode and tissue, we chose the worst case: i.e. with the vessel perpendicular to the device and below its point of contact. We also considered for each case different distances (D) from 1 to 5 mm between the electrode surface and vessel wall. However, when the vessel was parallel to the device or perpendicular to its distal end, due to the presence of the blade, the distances range (D) was from 3.5 to 5 mm (i.e. leaving a gap of 1 mm between blade and vessel). In all the simulations an applied voltage of 50 V was modeled (Burdío *et al* 2010) for 45 seconds. This time was considered long enough for the worst case, as surgeons rarely apply an electrode to a single point for a longer period. The dimensions of the thermal lesion created around the portal vein after ablation were assessed by the method described above.

6.3.6. Experimental setup

The *in vivo* experiments were conducted on one Landrace pig (weight 37.6 kg). The procedure was approved by the Ethical Commission of the Universitat Autònoma de Barcelona (authorization numbers DAAM 6267 and CEEAH 1256). Preoperative care and anesthesia were provided by fully trained veterinary staff. The animal was fasted for 12 hours before surgery. After initial sedation with a combination of azaperone and ketamine (4 and 10 mg/kg IM respectively), intravenous access was obtained through marginal ear-vein cannulation. Analgesia was provided with morphine (0.2 mg/kg IM) and anesthetic induction was performed with propofol (4 mg/kg IV). The animal was endotracheally intubated and anesthesia was maintained with isoflurane 2% in 100% oxygen. An infusion of lactated Ringer's solution was administered at a rate of 10 ml/kg/h during the entire study period. Heart rate, respiratory rate, pulse oximetry and capnography were monitored during anesthesia by a multiparametric monitor. Once anesthetized, the pig was positioned in dorsal recumbency and the abdomen was prepared aseptically. A midline laparotomy was performed and the liver was exposed. A high-resolution ultrasound system (Titan, SonoSite, Bothell, WS, USA) was employed to measure

the distance of the vessel from the treated area and the vessel diameter (see Figure 6.9(a)). A total of 6 thermal lesions were performed on the liver surface while attempting to keep the electrode perpendicular to the vessel. In the experiments we applied a voltage of 100 V for 45 s using a CC-1 Cosman Coagulation System RF Generator (Radionics, Burlington, MA, USA). This voltage value was higher than that used in the simulations, since the computational model did not consider the animal's total body impedance, i.e. all impedance associated with the body and dispersive electrode (Berjano and d'Avila 2013). Finally, the animal was euthanized with pentobarbital sodium, immediately after which the liver was cut into 1 cm slices perpendicular to the applicator axis for vital staining using nitroblue tetrazolium. The samples were then macroscopically examined to evaluate the thermal lesion and to quantify the damage in the vessel wall. The damage contour was assessed by the central "white zone" avoiding the surrounding red zone (absent in ex vivo experiments) (Goldberg *et al* 2005).

6.4. Results

6.4.1. Computer modeling

The convergence tests provided a value of $X = 80$ mm, $Y = 60$ mm and $Z = 30$ mm (tissue dimensions), a grid size of 0.11 mm in the finest zone (blade-tissue interface) and a step time of 0.05 s. The model had nearly 80,000 tetrahedral elements.

6.4.2. Comparison of blood flow models

Temperature distributions were firstly plotted for the XZ -plane (see Figure 6.2(a)), which was oriented perpendicular to the blood vessel axis through the center of the model. Figure 6.5(a) shows the tissue temperature distributions obtained after 45 s of RF heating by the three blood flow modeling methods: a constant heat transfer coefficient h_v at the tissue-vessel interface (Method 1); a temperature-dependent h_v (Method 2); and advection heat method (Method 3). These simulations were conducted with the entire device placed over the tissue, perpendicular to the

portal vein and at 5 mm below its center. The different distances and areas between the RF lesion and the portal vein for each method are compared in Figure 6.5(b). It can be seen that no damage occurred to the vessel wall with any method, the area between the RF lesion and the vessel being 19.50, 17.83 and 16.10 mm² for Method 3, 2 and 1, respectively. In brief, the three methods of modeling blood flow provided a similar temperature distribution around the vessel. However, the advection heat method was the only one in which the temperature value in the lumen of the vessel was not higher than in the wall (see Figure 6.5(a)). The temperature in the center of the lumen remained at $37.04 \pm 0.02^\circ\text{C}$, as opposed to $44.33 \pm 3.25^\circ\text{C}$ in Method 1 and $43.75 \pm 3.43^\circ\text{C}$ in Method 2. Method 3 was chosen for the subsequent simulations.

6.4.3. Thermal modeling

Figure 6.6 shows the evolution of temperature distributions and lesion in the tissue during 45 s of RF heating, computed by Method 3 with the configuration as shown in Figure 6.5. From the start ($t = 5$ s) heating was seen to be mainly located at the edges, especially around the tip of the blade and at the distal and proximal edges of the device. This is an edge effect observed along the length of the electrode. A temperature of 100°C was reached after 15 s at the proximal edge, where heating was even more intense than at the blade and proximal tip. The thermal lesion then moved towards the center of the tissue beneath the device, where it reached a lower temperature ($\approx 70^\circ\text{C}$). After 45 s of RF heating the thermal damage had encircled the vessel leaving the wall intact.

The thermal lesion dimensions were also plotted for the XY-plane (see Figure 6.2(a)), which was oriented parallel to the device's axis. Both the XY- and XZ-planes were used to compute the thermal lesions for different conditions, as shown in Figure 6.7. Figure 6.7(a) shows the thermal lesion dimensions in the tissue after RF heating with total device-tissue contact and the portal vein perpendicular to the device at different distances (D) below its center. In this case the thermal lesion shape was modified by the heat sink effect inside the vessel, which protected its wall, regardless of the vessel-device distance (see XZ-plane). It is also important to

note that an edge effect along the device's axis was also observed in the center below the device when $D \leq 3$ mm, this effect was more pronounced for $D = 1$ mm (see XY-plane). As can be seen in Figure 6.8(a), the vessel wall was not damaged by the thermal lesion contour ($\Omega = 1$) after RF heating for all vessel-device distances.

Figure 6.7(b) shows the thermal lesions created in the tissue with total device-tissue contact and the portal vein perpendicular to the device at different distances below its proximal end (D from 1 to 5 mm). In this case, the lesion shape was significantly modified around the vessel for all vessel-device distances (see XZ-plane), although 7.26% of the vessel wall was damaged (which corresponds to $\beta = 26.15^\circ$) at $D = 1$ mm, as shown in Figure 6.8(b). In this case the edge effect was less marked than in the previous case and occurred at $D \leq 2$ mm (see XY-plane in Figure 6.7(b)).

Figure 6.7(c) and 6.8(c) show the thermal lesions created in the tissue and the distances obtained between vessel and thermal lesion after RF heating, with total device-tissue contact and the portal vein perpendicular to the device at different distances below its distal end. As before, the thermal lesion shape was significantly modified by the heat sink effect caused by blood flow inside the portal vein (see XZ-plane in Figure 6.7(c)). In this case the vessel wall was damaged at $D \leq 4.25$ mm, as shown in Figure 6.8(c): 12.7% and 6.7% (with β of 43.8° and 24.12°) at $D = 3.5$ and 4.25 mm, respectively. As can be seen in Figure 6.7(c), the edge effect on the XY-plane was not caused by this vessel-device configuration.

Figure 6.7(d) and 6.8(d) show the thermal lesions created in the tissue and the distances obtained between vessel and thermal lesion after RF heating with total device-tissue contact and the portal vein parallel to the device. In this case the thermal dimensions were plotted for the XY-plane, as previously, and the YZ-plane (see Figure 6.2(a)), which was oriented perpendicular to the device's axis. As can be observed in Figure 6.7(d) on the YZ-plane, the thermal lesion shape around the portal vein was also modified by the heat sink effect for all vessel-device distances (D). Although in this case the vessel wall was damaged at $D \leq 4.25$ mm (see Figure 6.8(d)), the vessel damage being 5.88% and 2.21% ($\beta = 21.17^\circ$ and 7.94°) at $D = 3.5$

and 4.25 mm, respectively. The edge effect was not observed when the vessel was parallel to the device, as shown on the XY-plane in Figure 6.7(d).

The thermal lesions created in the tissue and the distances obtained between vessel and thermal lesion after RF heating for the case of proximal contact between tissue and device are shown in Figures 6.7(e) and 6.8(e), respectively. As expected, the thermal lesion is restricted to the area around the contact point, and hence is much smaller than the parallel contact cases. Although the thermal lesion shape was modified around the portal vein for all vessel-device distances (see XZ-plane in Figure 6.7(e)), i.e. the flowing blood provided a certain thermal protective effect, the vessel wall was damaged at $D \leq 4$ mm (see Figure 6.8(e)). The damage to the vessel wall was 26.96%, 20.14%, 13.88% and 0.65% ($\beta = 89.84^\circ, 72.49^\circ, 49.97^\circ$ and 2.33°) when D was increased from 1 to 4 mm. In this case a slight edge effect can be seen at the contact point for $D \leq 1$ mm (see XY-plane in Figure 6.7(e)).

Table 6.2 shows the initial impedance (Z_i), initial power (P_i), distributed energy (E) and maximum temperature reached in the tissue (T_{\max}) for all the cases studied. Z_i was seen to be much greater (up to twice as high) for the case in which the proximal part of the device was supported over the tissue than with total contact. Also, Z_i rose when D was increased from 1 to 5 mm for all configurations: approximately $\approx 2 \Omega$ in the case of total support and up to 15Ω for proximal contact. In general, the higher the Z_i , the lower was P_i . Finally, T_{\max} was slightly higher with proximal contact, whereas E was half that of the total contact cases (approximately 2 kJ versus 1 kJ).

6.4.4. Experimental validation

It was extremely difficult to find large-diameter (10 mm) vessels very close (< 5 mm) to the electrode. From a procedural point of view, it was also extremely complex to keep the electrode perpendicular to the vessel and at its mid point. The diameter of the vessels found in the experiments ranged from 2.6 to 7.6 mm (4.05 ± 1.99 mm). Distances between the device and the vessel (D) ranged from 7.4 to 16.2 mm (11.20 ± 3.98 mm). No damage was observed in any lesion as shown in Figure 6.9(b). Figure 6.9(c) also shows the computational thermal lesions corresponding to

the experimental cases. As can be seen, the shape and dimensions of experimental and computational thermal lesions were similar in all cases.

6.5. Discussion

The aim of this study was to assess whether the heat sink effect caused by the blood flow inside a large vessel could thermally protect its wall during a monopolar RF heating conducted by an internally cooled electrode. As far as we know, this problem has not been explicitly addressed before, as previous studies focused exclusively on determining how the flow inside vessels could distort the coagulation shape.

We first compared the three mathematical methods used in previous studies for modeling blood flow inside the vessel (Haemmerich *et al* 2003b, Chen and Saidel 2009, Dos Santos *et al* 2008, Consiglieri *et al* 2003, Consiglieri 2012, Antunes *et al* 2012, Shah *et al* 2005, Gopalakrishnan 2002). Although a recent study (Peng *et al* 2011) used a combination of Methods 1 and 3, this approach was not considered in our study. It has already been pointed out in computer studies on cardiac RF ablation that the convective boundary condition accounts for an average heat loss to blood, and that the use of such a boundary condition does not give an accurate blood temperature distribution. The blood temperatures obtained when using a convective boundary condition at the tissue-blood interface are higher than would be seen experimentally. Hence, more realistic blood temperatures could be predicted by including blood motion in the model (Jain and Wolf 2000). In this respect, our computational results from Methods 1 and 2 (convective boundary conditions) showed a higher temperature in the blood than in the vessel wall, which is physically impossible, remembering that temperature can only be increased at a distant point by thermal conduction from the tissue next to the electrode towards the point, and always with a decreasing gradient (by assuming similar thermal and electrical characteristics of tissue and blood). Moreover, in our experimental setup, due to the complexity of the *in vivo* scenario it was not possible to measure the temperature in the lumen of the vessel during the RF heating process, so that it was impossible to check this factor experimentally.

The evolution of the temperature distributions in the tissue during RF ablation showed that heating is preferentially located in the tissue under the edges of the device and at the tip of the blade, rather than in the middle zone (see Figure 6.6). This is because there is a high electrical gradient at these points which causes considerable Joule heating, resulting in a marked increase of temperature.

Regarding thermal lesion dimensions, the thermal lesion shape was considerably modified by the heat sink effect inside the portal vein for all the cases considered (see Figure 6.7). Only in the case of total device-tissue contact and with the portal vein in the central zone of the electrode, did the vessel wall remain undamaged, even for a vessel-device distance of 1 mm. However, in this case the edge effect was more pronounced than in the other cases, as shown on the XY-plane in Figure 6.7(a). The reason is that the tissue under the center of the device is heated to a lower temperature than the zone below the edges of the device (see Figure 6.6) and this edge effect is also enhanced by the cooling effect of the blood inside the vessel. These computational results therefore suggest that surgeons should take special care when the edges of the RF electrode, and specially the blade tip, are placed on a proximal vessel. This edge effect practically disappeared with total device-tissue contact and with the vessel below and perpendicular to the distal end of the device, the vessel parallel, and proximal device-tissue contact (see Figures 6.7(c), (d) and (e)). In these cases, the vessel wall was more seriously damaged than in the other cases (for $D \leq 4$ and 4.25 mm with proximal contact and for the abovementioned cases of total contact, respectively), which is why surgeons use this device when they intend to occlude a nearby vessel that is actually causing a hemorrhage.

As shown in Table 6.2, in the case of proximal contact the initial impedance was approximately twice as high as with total contact, since the device-tissue contact area was much smaller, which implies higher current density. Although higher Z_i implied lower P_i (since RF power is inversely proportional to impedance and the voltage was constant) the maximum temperature was also greater in this case due to the power being deposited in a much smaller volume than is the case with total contact. From a practical point of view, this result suggests that great care

should be taken when the vessel is near the electrode and the contact area between electrode and tissue is small. The effect of vessel-device distance on initial impedance was almost negligible. The drop in impedance at shorter distances was due to the electrical conductivity of the blood (0.667 S/m) being higher than that of the tissue (0.33 S/m). However, the influence of the tissue between the device and the vessel may account for the negligible influence of the vessel on initial impedance. This suggests that a predictive method of assessing the proximity of a large vessel by measuring impedance would not be feasible.

This computational modeling can be used to assess the capability of the internal blood flow to protect the vessel wall (i.e. to predict a thermal injury risk). However, as a partially damaged vessel wall could imply a significant clinical problem (such as vascular thrombosis), this is obviously outside the scope of a computer modeling study. Moreover, individual variations and the anatomical complexity of the liver tissue to be transected could have a considerable effect on the final phenomena, e.g. several vessels (arteries and veins) could be present in the transection line. We only considered the case of the portal vein. The results could be dissimilar for other vessel (e.g. hepatic vein) with different flow rates (Kröger et al. 2008). In spite of these limitations, the following conclusions can be drawn from the results.

Previous studies (Welp *et al* 2006, Lehmann *et al* 2009) used an *ex vivo* experimental approach in which the vessels were simulated by glass tubes and the blood flow by means of a saline flow controlled by a roller pump. However, we consider that the electrical insulation characteristics of the glass tube near the RF electrode could alter the electric field, so that using this insulating vessel could be useful to study temperature distributions and thermal lesions, as long as the vessel is placed sufficiently far away from the RF device. In order to demonstrate this we conducted an additional computer simulation (device totally placed over the tissue and vessel perpendicular to the device and at a distance of 5 mm below its center) considering an electrically insulating vessel. We compared the thermal results in both situations (i.e. blood vessel vs. insulating vessel) and observed that the temperature distributions and thermal lesions were different near the vessel. The

temperature in the center of the tissue below the device was $\approx 70^{\circ}\text{C}$ and 50°C with blood and insulating vessel, respectively. We therefore concluded that conducting an *ex vivo* study with a glass vessel (as portal vein) would not be suitable in our case for modeling thermal lesion dimensions in the proximity of the vessel.

Consequently, we conducted an *in vivo* experimental study in order to validate the computational results. We did not find vessels situated at a distance less than 5 mm from the RF device or with a diameter greater than 7.6 mm. We simulated all the experimental cases and verified the agreement between the thermal lesion geometries from the computational and experimental results (see Figure 6.9(b)-(c)). We also confirmed that the vessel wall was not damaged. This suggests that our computer model would be a good tool in assessing situations even more critical than that simulated in this study, i.e. in which the vessel was of larger diameter and located closer to the device.

Some previous experimental results could be also compared to our computer findings. For instance, Ng *et al* (2004) studied the local effect of RF ablation with a 3-mm electrode Cool-Tip on the left main portal vein. They found that RF ablation was safe at 5 mm from the main portal vein branch. The same study indicates the importance of blood flow for the thermal protection of the vessel, since the use of a Pringle maneuver (i.e. stopping internal blood flow) caused damage to the vessel wall. On the other hand, in another experimental study on RF ablation (50 W power) adjacent to large hepatic veins, some cases of intimal damage to large veins were reported when the electrode tips were within 5 mm of the confluence of the hepatic veins (Metcalf *et al* 2007). A third experimental study on RF ablation with a electrode Starburst XL reported that when the electrode was placed 10 mm (± 1 mm) away from the portal vein, the delivered power was not able to overcome the heat dissipation of the vein, so that the coagulation zones around the vessels were distorted (Bangard *et al* 2006). These experimental findings suggest that the threshold value for the distance between the RF heating electrode and large hepatic vessels should be around 5 mm if thermal damage to the vessel wall is to be avoided, which is in close agreement with the value indicated by our computer results.

6.6. Conclusions

The experimental and computational results suggest that the heat skin effect could protect the vessel wall at vessel-device distances equal to or greater than 7.4 mm. The computer results also confirm that predictions can be made as to whether or not the vessel wall could be damaged at lower vessel-device distances. It is possible that the blood flow inside a large vessel (such as the portal vein) could protect its wall at distances equal to or greater than 5 mm, regardless of its position with respect to the RF device (parallel or perpendicular and under the distal, center or proximal part of the device) with the device in contact with the tissue (total or proximal). The thermal damage is inversely related to the vessel-device distance and is more marked when the vessel is placed parallel to the device or perpendicular to its distal end or with partial device-tissue contact (e.g. when only the proximal portion of the device is used to coagulate before dissecting).

Table 6.1. Thermal and electrical characteristics of the elements employed in the numerical modeling (Data from (Haemmerich *et al* 2003b, Pätz *et al* 2009, Berjano *et al* 2006, Duck 1990, Burdío *et al* 2009)).

Element/Material		σ (S/m)	k (W/m·K)	ρ (kg/m ³)	c (J/kg·K)
Electrode		$7.4 \cdot 10^6$	15	8000	480
Plastic		10^{-5}	0.026	70	1045
Blood		0.667	0.543	1000	4180
Liver tissue	Liquid phase	0.33*	0.502*	1080	3455
	Gas phase			370	2156

σ , electric conductivity; k , thermal conductivity; ρ , density; and c , specific heat.

* Assessed at 37°C.

Table 6.2. Initial impedance (Z_i), initial power (P_i), distributed energy (E), maximum temperature reached in the tissue (T_{\max}) for the cases studied. D: vessel-device distance

Cases		Z_i (Ω)	P_i (W)	E (kJ)	T_{\max} ($^{\circ}\text{C}$)
Device-tissue contact/vessel-device position	D (mm)				
Total contact/ perpendicular below its center	1	67.05	37.28	1.982	106.14
	2	67.98	36.78	1.980	109.17
	3	68.64	36.42	1.979	105.39
	4	69.00	36.23	1.980	107.07
	5	69.21	36.12	1.979	109.42
Total/ perpendicular below its proximal end	1	67.29	37.15	1.958	109.05
	2	68.36	36.57	1.964	107.73
	3	69.08	36.19	1.972	108.67
	4	69.59	35.93	1.970	107.67
	5	69.75	35.84	1.972	107.07
Total/ perpendicular below its distal end	3.5	69.09	36.18	1.966	108.22
	4.25	69.44	36.00	1.965	106.48
	5	69.69	35.87	1.968	108.13
Total/ parallel below it	3.5	66.16	37.78	2.016	106.37
	4.25	67.05	37.28	2.022	106.83
	5	67.86	36.84	2.019	108.49
Proximal/ perpendicular below its contact point	1	155.77	16.05	0.947	118.34
	2	161.82	15.45	0.970	113.23
	3	165.24	15.13	0.983	118.61
	4	167.70	14.91	0.985	112.86
	5	170.93	14.63	0.978	118.26

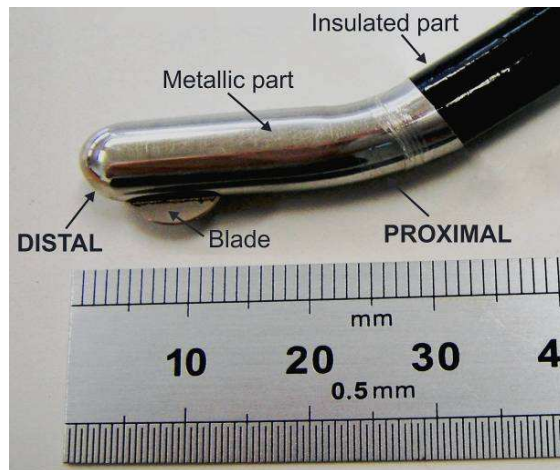


Figure 6.1. Coolinside surgical device for RF-assisted resection (Apeiron Medical, Valencia, Spain) of 8 mm in diameter and based on an internally cooled electrode. Distal end is shown with the blade and proximal end joined to the insulated part of the device.

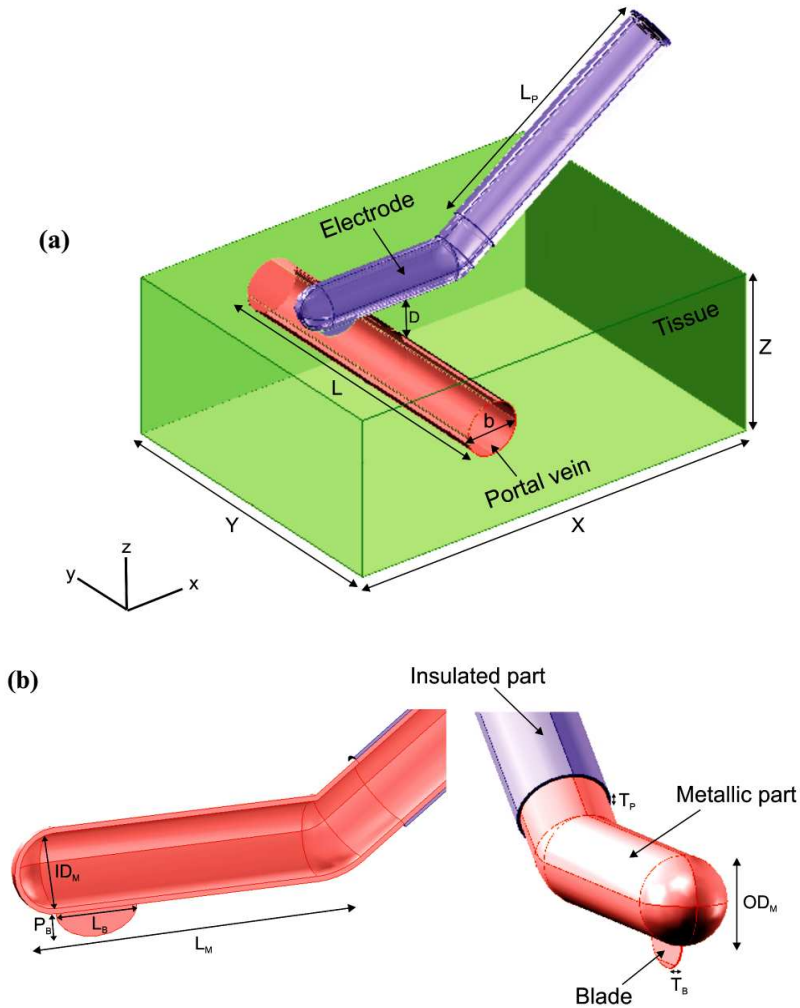


Figure 6.2. (a) Geometry and dimensions of the three-dimensional model built for the study. Tissue dimensions X , Y and Z ($Z = Y/2$) were obtained from a convergence test. The portal vein has diameter $b = 10$ mm, length L ($L = Y$) and is located in the middle, perpendicular to and at distance D below the electrode. L_p : length of the isolated section of the electrode. (b) Internal and external view and dimensions of the RF-assisted device. L_M : length of the metallic part in contact with the tissue; OD_M and ID_M : outer and inner diameter; P_B : insertion depth of the blade; L_B : blade length; T_B : blade thickness; T_P : thickness of the isolated section.

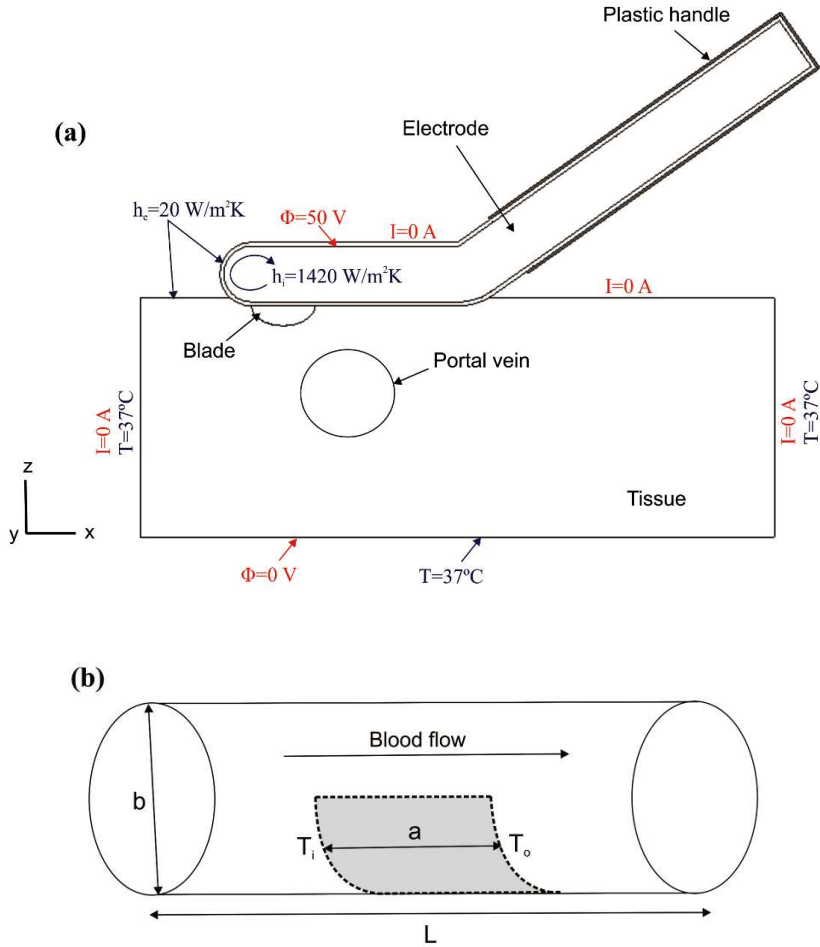


Figure 6.3. (a) Electrical (red) and thermal (blue) boundary conditions of the numerical model. The Figure shows the XZ-plane of the model. (b) Model used in the analysis of boundary conditions of the blood vessel. a: length of the heated region of the vessel during RF ablation, b: vessel diameter, T_i : inlet blood temperature, T_o : outlet blood temperature of the vessel and L : length of the vessel.

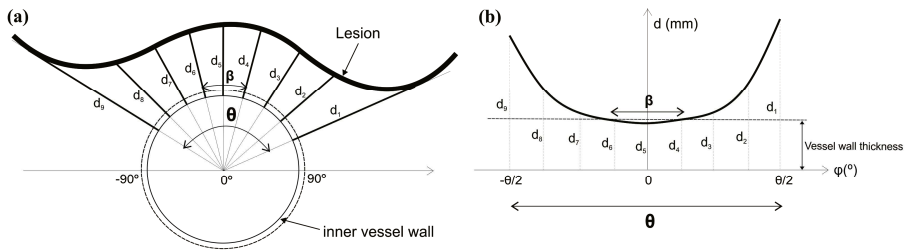


Figure 6.4. Procedure used to obtain the distances and area between the RF lesion and the vessel and to assess possible damage in the vessel wall: **(a)** Measurement of 9 distances according to angle θ , formed by the transverse distances between the lesion edges and the vessel (d_1 and d_9). **(b)** Graphical representation of these distances with respect to θ . The horizontal dashed line represents the vessel wall thickness and β the arc of the vessel damage.

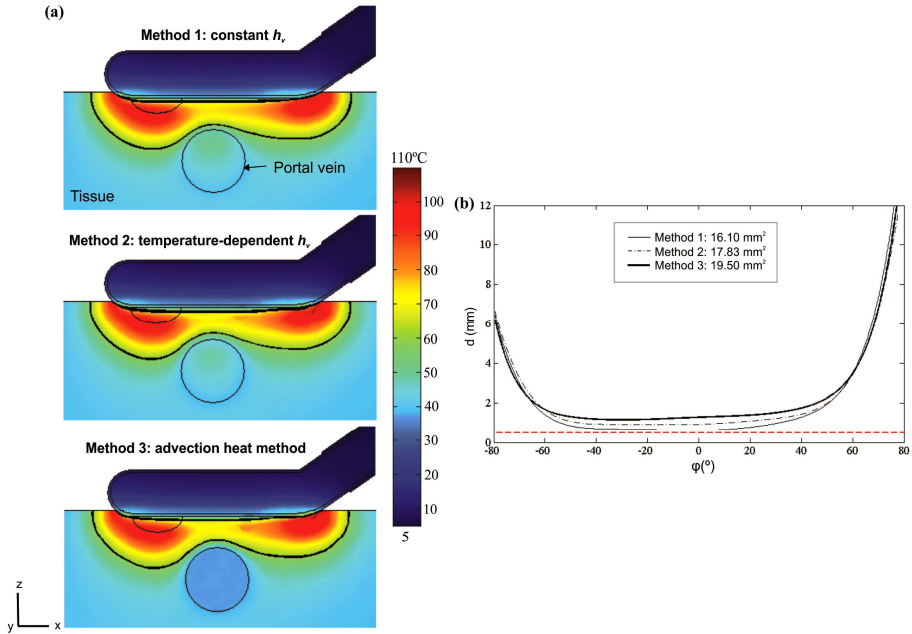


Figure 6.5. (a) Temperature distribution (in °C) in the tissue after 45 s of RF heating computed by three different methods of modeling the cooling effect of the blood flow inside the portal vein. Method 1: a constant heat transfer coefficient h_v at the tissue-vessel interface; Method 2: a temperature-dependent h_v ; and Method 3: advection heat method. The entire device is placed over the tissue and the portal vein is located perpendicular to the device and at 5 mm below its center. The solid black line is the thermal damage border ($\Omega = 1$). (b) Distances and area between the portal vein and the thermal lesion for each method to quantify the thermal damage in the vessel wall. The horizontal dashed line represents the vessel wall thickness (0.5 mm).

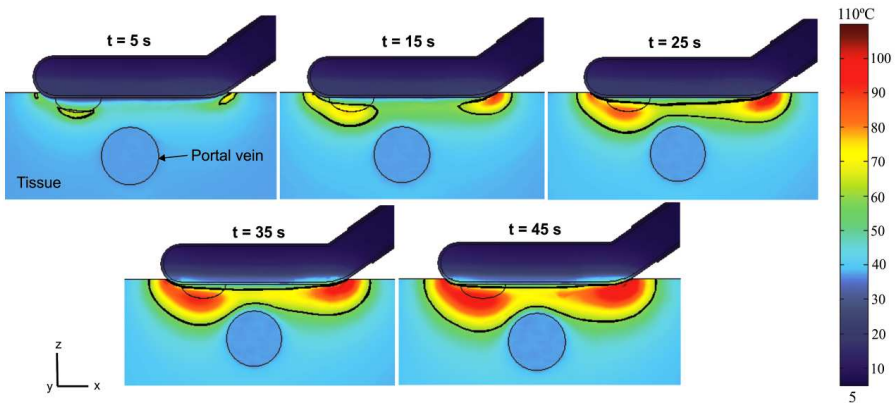


Figure 6.6. Evolution of the temperature distribution (in $^{\circ}\text{C}$) in the tissue during RF heating, considering total tissue-device contact, with the portal vein perpendicular to the device and at 5 mm below its center. The solid black line is the thermal damage border ($\Omega = 1$).

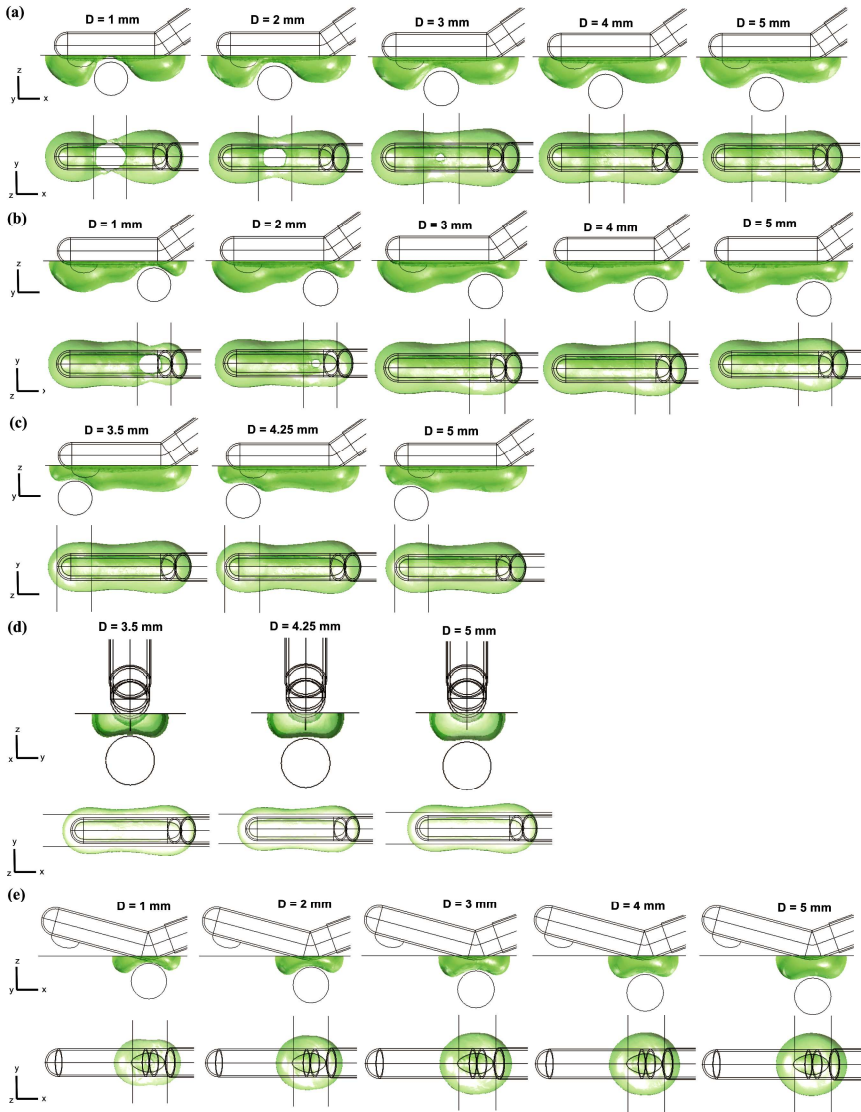


Figure 6.7. Thermal lesions created in the tissue after 45 s of RF heating, varying vessel-device distance (D), device-tissue contact and vessel position. Cases: total vessel-device contact and vessel perpendicular below the center of the device (a), below its proximal end (b) and below its distal end (c), vessel parallel to the device (d), and proximal vessel-device contact and vessel perpendicular to the device (e). The thermal damage surface corresponds to $\Omega = 1$.

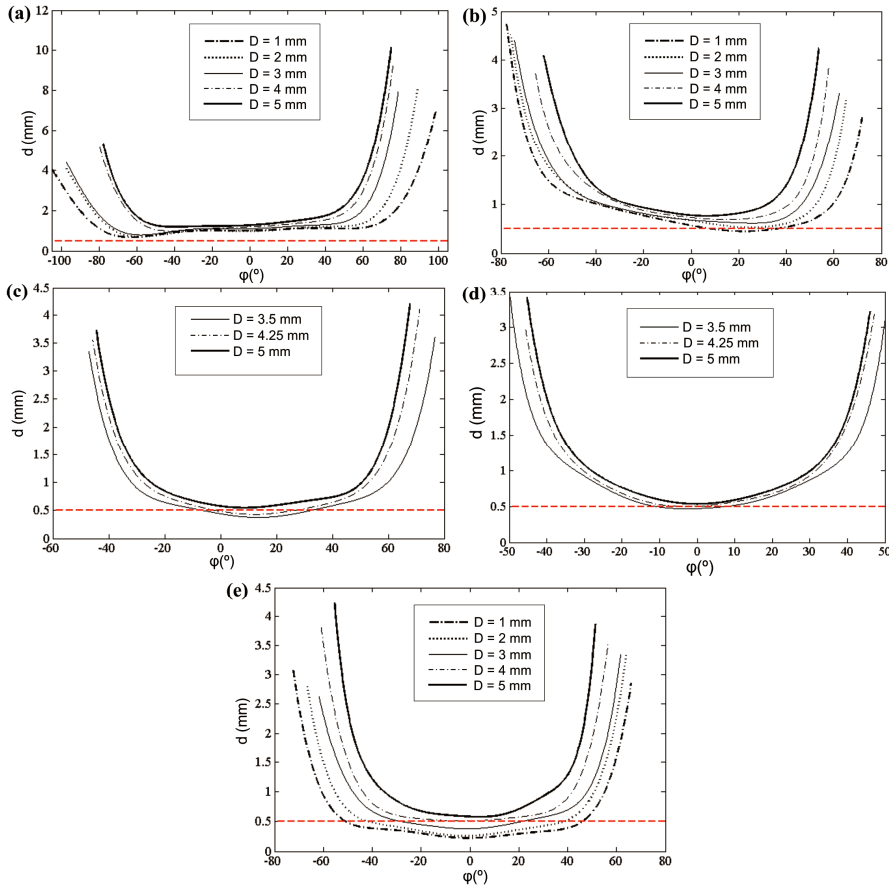


Figure 6.8. Distances obtained between the portal vein and the thermal lesion for each vessel-device distance (D) used to quantify thermal damage in the vessel wall. Cases: total vessel-device contact and vessel perpendicular below the center of the device (a), below its proximal end (b) and below its distal end (c), vessel parallel to the device (d), and proximal vessel-device contact and vessel perpendicular to the device (e). The horizontal dashed line represents the vessel wall thickness (0.5 mm).

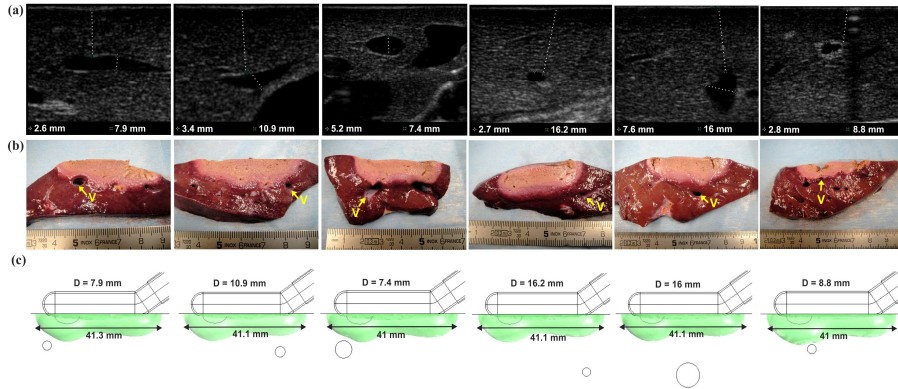


Figure 6.9. Ultrasonography employed to measure the distance of the vessel-device distance and the vessel diameter (a); experimental (b) and computational (c) thermal lesions created in the tissue after 45 s of RF heating with the entire device placed over the tissue surface, with the vessel perpendicular to the device and at different distances (D) below it. Symbol “V” indicates the location of the vessel whose diameter varies from 2.6 to 7.6 mm. The thermal damage surface corresponds to “white zone” in the experimental results and to $\Omega = 1$ in the computational simulations. Note that the “red zone” does not correspond to the thermal lesion and therefore the white zones shown in (b) have to be compared to the corresponding computed lesion in (c).

Chapter 7

Thermo-elastic Response to RF Heating with Thermal Damage Quantification of Subcutaneous Adipose Tissue of Different Fibrous Septa Architectures: A Computational Modeling Study

7.1. Abstract

Background and objectives: Radiofrequency (RF) energy is widely used to heat cutaneous and subcutaneous tissues in different dermatological applications. Since the qualitative and quantitative features of physical thermo-elastic mechanism of dermal heating in the presence of the fibrous septa network between fat lobules is not well understood, our objectives were: 1) to build a computational model for selective, non-invasive, non-ablative RF heating of cutaneous and subcutaneous tissues, considering two conditions of fibrous septa within the subcutaneous tissue: low (cellulite Grade 2.5) and high (cellulite Grade 0, i.e. smooth skin) spatial density of fibrous septa; 2) to study the effect of the fibrous septa density and orientation on the thermo-elastic response during RF heating; and 3) to quantify the induced thermal damage in both subcutaneous tissue structures after RF heating.

Methods and results: We built two-dimensional models with skin, subcutaneous tissue and muscle. The modeling of the subcutaneous tissue included two realistic structures of fibrous septa and fat lobules (low and high spatial density) obtained by

processing sagittal images of hypodermis from micro-magnetic resonance imaging (micro-MRI). Our results showed that a higher density of fibrous septa enhances the strength of the electrical field in terms of favoring the flux of electric current and consequently increases power absorption within the subcutaneous tissue. Heating and thermal damage was therefore greatest in this zone, with a damage region ≈ 1.5 times higher than with low septa density. Shrinkage of fibrous septa was higher with fibrous septa at low spatial densities. Skin and muscle were subjected to higher thermal stresses than the subcutaneous tissue.

Conclusions: Our findings show the importance of including real anatomical features when modeling RF heating of subcutaneous tissue. This is important in accurately estimating thermal damage after RF heating in order to assess the correct dosimetry.

7.2. Introduction

Radiofrequency (RF) energy is commonly used to heat tissues to specific target temperatures that vary for different procedures, ranging from a few degrees for low hyperthermia applications to over 100°C for tissue ablation. In the case of RF heating of cutaneous and subcutaneous tissues, RF currents shrink the dermal collagen and induce stimulation of fibroblast cells that produce new collagen (Sadick and Makino 2004). Applications in dermatology include skin tightening, reduction of wrinkles and treatments for acne and cellulite (Dierickx 2006, Lolis and Goldberg 2012). Unlike other clinical areas, the heating of cutaneous and subcutaneous tissues is not straightforward, since the RF device is in contact with non homogeneous tissues, resulting in more complex physical interactions between RF currents and tissue. Subcutaneous tissue morphology consists of a fine, collagenous and fibrous septa network enveloping clusters of adipocyte cells. Furthermore, the density and orientation of fibrous septa within subcutaneous tissue may vary from person to person. These variations are linked to different cellulite grades, which correlate with the percentile of adipose tissue versus connective tissue in a given volume of hypodermis and invaginations inside the dermis. Cellulite Grade is assessed by visual inspection according to skin appearance and scaled in

appearance from Grade 0, smooth skin, to Grade 4 “cottage cheese” (Mirrashed *et al* 2004).

In a previous modeling study based on a three-layer tissue (skin, subcutaneous tissue, and muscle), we found that the structural configuration of fibrous septa within subcutaneous tissue has a considerable effect on the distribution of the power deposition (Jimenez Lozano *et al* 2013). Our computer simulations predicted a greater temperature rise when the model of subcutaneous tissue included a realistic architecture of the fibrous septa (anatomically accurate and constructed from sagittal images from human micro-MRI) instead of a homogenous layer of fat only. Our research was focused on the hyperthermic range of temperatures (<50°C) and hence can be considered as non-ablative. Previous work considered only an arrangement of fibrous septa corresponding to a cellulite ‘Grade’ of 2.5. Since RF techniques are not only used to treat cellulite, it is important to be able to improve the electrical and thermal performance in the case of smooth skin, i.e. where the density of fibrous septa is highest. There is a lack of information on the qualitative and quantitative features of physical thermo-elastic mechanism of dermal heating in the presence of fibrous septa network between fat lobules. Information on the thermo-elastic response of cutaneous and subcutaneous tissues (including the fibrous septa network), such as the thermal denaturation mechanism of collagen (thermal shrinkage) during RF heating (Xu and Lu 2011), would be useful for the development of new products and improving existing products/treatments in clinical and cosmetic applications. Due to the difficulty of experimentally measuring the thermo-elastic behavior of subcutaneous tissue in physiological conditions, we conducted a computational modeling for this purpose. As far as we know, this aspect has not been studied previously. Our objectives were therefore as follows: 1) to build a computational model for selective, non-invasive, non-ablative RF heating of cutaneous and subcutaneous tissues, considering two conditions of fibrous septa within subcutaneous tissue: low (cellulite Grade 2.5) and high (cellulite Grade 0, i.e. smooth skin) spatial density of fibrous septa; 2) to study the effect of fibrous septa density and orientation on the thermo-elastic response during RF heating; and 3) to

quantify the induced thermal damage occurred in both subcutaneous tissue structures after RF heating.

7.3. Materials and methods

7.3.1. Physical Situation

Figure 7.1 shows the geometry and dimensions of the model and includes an RF applicator (plate) placed over a fragment of tissue which has three layers (skin, subcutaneous tissue: fat+septa and muscle). The geometry of the model was mirrored on the sides to avoid lateral boundary effects focusing on the area beneath the RF applicator. The thicknesses of the skin (l_s), fat+septa (l_{f+s}) and muscle (l_m) layers were 1.5, 17, and 38 mm, respectively; layer width (W) being 54.5 mm (Mirrashed *et al* 2004, Franco *et al* 2010). The RF applicator has 18.5 mm long (L) (Franco *et al* 2010) and was cooled to keep surface temperature around 30°C.

We considered two different structures of fibrous septa, which have been shown to be correlated to cellulite and non cellulite presence in human subjects (Mirrashed *et al* 2004), as shown in Figure 7.2. Hereafter, Case 1 and Case 2 represent configurations of low (cellulite Grade 2.5) and high (smooth skin, non cellulite) spatial density of fibrous septa within the hypodermis, respectively. The anatomically accurate fibrous septa structures were obtained by post-processing sagittal images of hypodermis from micro-MRI, using Adobe Illustrator CS3 (Adobe Systems, San Jose, CA, USA), as in a previous study (Jimenez Lozano *et al* 2013), which modeled the Case 1 structure. The subcutaneous tissue structure shown in Figure 7.1 is from Case 2.

7.3.2. Governing Equations

The numerical model was based on a coupled electro-thermo-elastic problem, which was solved numerically using the Finite Element Method (FEM) with COMSOL Multiphysics 4.3b (COMSOL, Burlington, MA, USA). The biological medium can be considered almost totally resistive and a quasi-static approach is therefore possible to solve the electrical problem (Doss 1982) due to the

RF frequencies (≈ 500 kHz) and over the distance of interest (the electrical power is deposited in a very small zone close to the electrode). Electric propagation is assumed time independent, since it is much faster than heat diffusion and the thermo-elastic response. The rate of energy dissipated per unit volume at a given point in biological tissue is directly proportional to the electrical conductivity of the tissue and to the square of the induced internal electric field, $Q = \sigma|\mathbf{E}|^2/2$, where Q is the power absorption (W/m^3), $|\mathbf{E}|$ the norm of the vector electric field (V/m) and σ the electrical conductivity (S/m). \mathbf{E} is calculated from $\mathbf{E} = -\nabla\Phi$, where Φ is the voltage (V) obtained by solving Laplace's equation:

$$\nabla \cdot (\sigma \nabla \Phi) = 0 \quad (1)$$

The thermo-elastic behavior of the tissue was considered to be a two-way coupled problem, which means that the elastic behavior has an influence on the thermal behavior. The deformations of the tissue caused by thermal changes also affect thermal properties. This coupling is more realistic than that set forth in (Xu and Lu 2011), where the thermo-mechanical behavior of skin was simplified to be a sequentially-coupled problem so that the temperature field in skin tissue is first obtained from solving the governing equations of bioheat transfer and it was then used as the input of the thermo-mechanical model, from which the corresponding thermal stress was obtained.

The governing equation for the thermal problem was the Bioheat Equation (Pennes 1948) which incorporates the second term for thermo-elastic coupling (i.e. \mathbf{u} in the equation was the result of the elastic problem):

$$\rho c \frac{\partial T}{\partial t} + \rho c \mathbf{u} \cdot \nabla T = \nabla \cdot (k \nabla T) + Q_m + c_b \omega (T_b - T) + Q \quad (2)$$

where ρ is density (kg/m^3), c specific heat ($\text{J}/\text{kg}\cdot\text{K}$), T temperature ($^\circ\text{C}$), t time (s), $\mathbf{u} = \{u, v\}$ is the displacement vector (m), k thermal conductivity ($\text{W}/\text{m}\cdot\text{K}$), Q_m the metabolic heat generation (W/m^3), which is considered negligible in comparison with the other terms (Berjano 2006), c_b blood specific heat ($\text{J}/\text{kg}\cdot\text{K}$) (Franco *et al* 2007), ω blood perfusion rate ($\text{kg}/\text{m}^3\cdot\text{s}$), and T_b blood temperature ($^\circ\text{C}$).

The elastic behavior of the tissue, which describes its motion and deformation, was studied by means of the motion equation for an isotropic linear elastic solid, which is given by:

$$\rho \frac{\partial^2 \mathbf{u}}{\partial t^2} - \nabla \boldsymbol{\sigma} = \mathbf{F}_v \quad (3)$$

where $\boldsymbol{\sigma}$ is the stress tensor (Pa) and \mathbf{F}_v are the external volume forces (Pa/m²). Constitutive relations for an isotropic linear elastic material are: (i) the stress tensor $\boldsymbol{\sigma} = [S(\mathbf{I} + \nabla \mathbf{u})]$, where S is the Duhamel term which relates the stress tensor to the strain tensor and temperature, $\nabla \mathbf{u}$ the displacement gradient and \mathbf{I} the identity matrix; (ii) the Duhamel relation $S - S_0 = C : (\boldsymbol{\epsilon} - \boldsymbol{\epsilon}_0 - \alpha(T - T_0))$, where C is the 4th order elasticity tensor, “:” stands for the double-dot tensor product (or double contraction), $\boldsymbol{\epsilon}$ is the strain tensor, S_0 and $\boldsymbol{\epsilon}_0$ are initial stresses and strains, α the thermal expansion coefficient (1/°C), and T_0 the initial temperature; and (iii) the strain tensor which is written in terms of the displacement gradient $\boldsymbol{\epsilon} = [\nabla \mathbf{u}^T + \nabla \mathbf{u}]/2$. The formulation of elasticity equations is Lagrangian, which means that the computed stress and deformation state always refers to the material configuration rather to the current position in space. Likewise, these material properties are derived in a material frame of reference in a coordinate system \mathbf{X} . When solid objects deform due to external or internal forces and constraints, each material particle keeps its coordinates \mathbf{X} , while spatial coordinates \mathbf{x} change with time and applied forces such that they follow a path $\mathbf{x} = \mathbf{X} + \mathbf{u}(\mathbf{X}, t)$ in space. Because the material coordinates are constant, the current spatial position is uniquely determined by the displacement vector \mathbf{u} .

The thermal damage in the tissue is assessed by the Arrhenius equation (Henriques and Moritz 1947, Moritz and Henriques 1947), which associates temperature with exposure time, using a first order kinetics relationship:

$$\Omega(t) = \int_0^t A e^{\frac{-\Delta E}{RT}} dt \quad (4)$$

where $\Omega(t)$ is the degree of tissue injury, R the universal gas constant, A the frequency factor (s^{-1}), and ΔE the activation energy for the irreversible damage reaction (J/mol). The parameters A and ΔE for the skin are (Weaver and Stoll 1969): $A = 2.2 \cdot 10^{124} s^{-1}$ and $\Delta E = 7.8 \cdot 10^5 J/mol$. We employed the thermal damage threshold $\Omega = 1$, which represents the threshold of complete irreversible thermal damage (63% reduction in cell viability).

7.3.3. Tissue Characteristics

The electrical, thermal and elastic properties of the model elements (skin, fat, fibrous septa and muscle) are shown in Table 7.1. The electrical properties were assumed frequency-dependent (Miklavčič *et al* 2006) and those used herein correspond to 1 MHz. As regards the thermal properties, we assumed that tissues were isotropic materials. Each tissue had constant values of thermal conductivity, specific heat and the blood perfusion term, since within the 35-50°C range, variations in specific heat (Haemmerich *et al* 2005), thermal conductivity (Bhattacharya and Mahajan 2005) and blood perfusion (constant in this range (Xu and Lu 2011)) were not significant. The electrical and thermal properties of fibrous septa have not previously been investigated. We assumed that the properties of fibrous septa were similar to those of the dermis, as it is a collagen tissue and an extension of the dermis (Jimenez Lozano *et al* 2013). For the elastic properties, we assumed that tissues were linear elastic materials and isotropic, with properties independent of direction that can be characterized by their Young's modulus (E) and Poisson's ratio (ν). We assumed that strains and displacements were small in order to use linear elasticity theory and thermal expansion.

7.3.4. Boundary and initial conditions

Table 7.2 shows the electrical, thermal and elastic boundary conditions applied to the model (Franco *et al* 2010, Pailler-Mattei *et al* 2008, Comley and Fleck 2010, Deng and Liu 2003, Lin 2005). As regards the electric boundary conditions, the RF applicator was modeled as a constant voltage source on the skin surface

beneath the applicator. We used an empirical voltage distribution $V(x)$ published in (Franco *et al* 2010) for a monopolar applicator operating at 1 MHz:

$$V(-L/2 \leq x \leq L/2) = [a \left(\frac{Lx}{L} \right)^2 + b] \sqrt{PZ} \quad (5)$$

where $a = -2.25 \cdot 10^{-3}$, $b = 1.28$, P (150 W) is the applied RF power and Z (100 Ω) the impedance of the tissues. A zero voltage condition was applied to the lower surface of the muscle (mimicking the electrical performance of the dispersive electrode) and a null electrical current was used on the remaining skin surface and at lateral boundaries. For the thermal boundary conditions, a constant temperature of 30°C was applied above the applicator to model its cooling (T_r), and 37°C (constant core body temperature, T_c) was fixed at the lower muscle surface. The effect of air convection on the remaining skin surface was taken into account using a thermal transfer coefficient (h_{a-s}) of 10 W/m²K and a value of 25°C was considered for ambient temperature (T_a). A zero thermal flux condition was applied at the lateral boundaries.

For the elastic boundary conditions, a free movement condition was used at the lateral boundaries to model the absence of constraints and loads. A fixed constraint condition on the upper skin and lower muscle surfaces was applied to simulate that displacements are zero in these directions, since on the skin surface was located the RF applicator and was assumed that the lower muscle surface was attached to the bone.

As initial conditions, we assumed non applied voltage (0 V), initial temperature T_0 of 37°C, and no initial strain. Simulations were run in a 64-bit PC with a 12-processor Intel Xeon platform running at 2.30 GHz with 8 GB of RAM memory. The model meshes consisted of 30,545 and 45,208 elements for low (Case 1) and high (Case 2) spatial density of fibrous septa, respectively. Skin, fat, muscle and septa central domains (beneath RF applicator) had a higher mesh density. The time-dependent solution was set from 0–8000 s with a time-step of 0.1 s. We used a multifrontal massively parallel sparse (MUMPS) direct solver.

7.4. Results

7.4.1. Electric Response

Figure 7.3 shows the voltage distributions for the two cases of subcutaneous tissue considered. The maximum value of voltage in both cases was located just below the mid-point of the applicator (see Figure 7.3(a)-(b)). In both cases, the largest voltage drop occurred within skin and subcutaneous tissue layers, as shown in the voltage distribution profile at $x = 0$ (Figure 7.3(c)). However, slightly more irregularities in the subcutaneous tissue (fat+septa) were observed in Case 2. In fact, a higher density of fibrous septa (Case 2) caused an increase in both the extent (in depth and width) and strength of the electric field within the subcutaneous tissue (see Figure 7.4(a)-(b)), with a maximum electric field value of 4.321 V/mm, as opposed to 3.365 V/mm for a lower density of fibrous septa (Case 1). We observed clearly in Figure 7.4(c) that the strength of the electrical field in the fat lobules was greater than in the fibrous septa, in other words, the electric field profile showed an abrupt drop exactly where the electrical currents flow through fibrous septa. This means the fibrous septa network conducted the electric flux to deeper subcutaneous tissue zones, favoring electric field accumulation in the fat lobules.

Electric power absorption within the tissue is shown in Figure 7.5 for both cases. A higher density of electric field was generated at the edges of the applicator, causing an accumulation of power absorption in that zone, as shown in Figure 7.5(a)-(c). The fibrous septa eased the flow of electric currents and thus caused considerable accumulation of electric power in some fibers (see Figure 7.5(b)-(d)).

7.4.2. Temperature Response and Damage Quantification

Figure 7.6 shows the temperature distributions after RF heating for both cases of subcutaneous tissue structure. The heating was mainly confined to the subcutaneous tissue, as a consequence of greater electric absorption and heat diffusion into this area. The temperature in the skin remained lower than the subcutaneous tissue, due to surface cooling. The effect of increasing the density of fibrous septa slightly enhanced the heating of the subcutaneous tissue, causing an

increase of $\approx 1^\circ\text{C}$ in the maximum temperature (48.12°C in Case 1 vs. 49.28°C in Case 2). The time progression of temperature distribution profiles at $x = 0$ are shown in Figure 7.7 for both cases. The temperature profile showed a similar pattern in both cases: it stayed lower in the skin due to the cooling effect of the plate, increased parabolically within the subcutaneous tissue and then decayed exponentially in the muscle. The temperature difference between cases increased with time, being greater with higher fibrous septa density (Case 2). The thermal damage zone in both cases was located within the subcutaneous tissue, without damage to the skin (see Figure 7.6), and was ≈ 1.5 times larger in the case of higher spatial fibrous septa density (Case 2). In this case, the thermal lesion region was also slightly deeper and even reached the muscle.

7.4.3. Thermo-elastic Response

Volumetric strain can be used to assess the thermo-elastic response of the tissue during RF heating, since it measures the deformation of the tissue from its original volume. Figure 7.8 shows the volumetric strain map at different times (25 and 8000 s) for both cases. As observed in Figure 7.8(a)-(b), during the initial times (25 s) most of the subcutaneous tissue (both fat lobules and fibrous septa) had a positive volumetric strain value, showing that it initially expanded before the steady-state was reached. The fact that the skin had negative volumetric strain was due to its contact with the cooling plate. At the steady-state (see Figure 7.8(c)-(d)), volumetric strain was greater in the subcutaneous tissue zone, where a higher temperature was reached, and also in the connective fat-muscle layer. However, this value was negative in the fibrous septa, showing the contraction (shrinkage) process.

The time progression of volumetric strain profiles at $x = 0$ for both cases is shown in Figure 7.9. In both cases, at initial times (25 s) fibrous septa showed greater volumetric strain than fat, since we assumed that septa had a higher thermal expansion coefficient. At later times, the fibrous septa showed a negative strain (i.e. shrinkage) due to the adjacent expansion of fat lobules and skin contraction. This shrinkage was more marked in subcutaneous tissue with lower fibrous septa spatial density, as shown in Figure 7.9(a).

The Von Mises yield criterion states that a material starts yielding when its Von Mises stress reaches a critical value, known as the yield strength. All materials have an associated yield strength, which is a measure of their elastic limit, and will not return to their original shape if the stress is removed. As the Von Mises stress is a good measure of thermal stress, we also plotted the Von Mises stress map for both cases (see Figure 7.10(a)-(b)). It can be seen that skin and muscle were subjected to a higher stress than subcutaneous tissue. Stress in the skin was uniform, due to thermal contact with the cold plate, while in the muscle it was higher close to the subcutaneous tissue region associated with the highest temperature. Von Mises stress was higher in Case 2 than in Case 1 (31.24 Pa and 28.77 Pa, respectively). Figure 7.10(c) shows marked changes in the stress in the skin-subcutaneous tissue and subcutaneous tissue-muscle interfaces. These abrupt changes at the interfaces cause shear in the tissue.

7.4.4. Comparison with case of absence of fibrous septa

Finally, we compared the thermal damage zones computed by considering the exact anatomy of the two conditions of fibrous septa density within the subcutaneous tissue (Cases 1 and 2) and a homogeneous subcutaneous tissue layer (with fat only), as considered in (Jimenez Lozano *et al* 2013). In this case we modeled RF heating with 200 W of applied power. Figure 7.11 shows that when simplifying the subcutaneous tissue model by ignoring the fibrous septa network, the thermal lesion was approximately 2 and 3 times smaller, respectively, than for the two conditions of fibrous septa density considered (Cases 1 and 2).

7.5. Discussion

The aim of this study was to assess the thermo-elastic response of low and high fibrous septa density during RF hyperthermic heating and to quantify the induced thermal damage after heating in both cases. To our knowledge, no study has previously been made of either the thermo-elastic response or the thermal damage in both structures.

As regards electrical response, the results showed that the electric flux preferably flowed through the fibrous septa network surrounding the fat lobules, as shown in Figure 7.5. As we mentioned in a previous work (Jimenez Lozano *et al* 2013), this is due to the electrical conductivity of the septa ($\sigma_{sp} = 0.22$ S/m) being much higher than that of fat ($\sigma_f = 0.025$ S/m) and consequently providing a less resistive path for electrical currents to the deeper subcutaneous tissues zones. Higher fibrous septa density (Case 2) therefore created preferential electrical paths within the subcutaneous tissue (see Figure 7.5(d)) and higher electric field accumulation in the fat lobules (see Figure 7.4(b)). Moreover, in the case of higher septa density (Case 2) the electric field had greater depth and width than in the lower density case (see Figure 7.4), which was probably the cause of the larger thermal lesion in Case 2 (see Figure 7.6(b)). In both cases, the highest temperatures were confined to the subcutaneous tissue (see Figure 7.6). This was due to the electric field in the fat lobules being much stronger than in the skin, septa or muscle, as can be seen in Figure 7.4. Consequently, higher power absorption occurred in the fat lobules, since absorption is proportional to E^2 . In the case of the higher septa density (Case 2), heating within the subcutaneous tissue was greater than in Case 1, since the electric field was stronger at some points in the fat lobules, as shown in Figure 7.4(b).

Regarding thermo-elastic response, we observed that the shrinkage of fibrous septa within subcutaneous tissue was smaller in Case 2, probably because the contraction of this tissue was compensated by the effect of opposing forces (i.e. expansion and contraction) in the solid structure of the fibrous septa network. Thermal denaturation of collagen may not occur in either density of fibrous septa, since our study was conducted within the hyperthermic temperature range ($< 50^\circ\text{C}$) and collagen is denatured around 65°C (Xu and Lu 2011).

The comparison between the thermal damage zones computed for both fibrous septa densities within the subcutaneous tissue and the homogeneous subcutaneous tissue case (fat only) (see Figure 7.11) showed a difference of up to 50%, which suggests the necessity of accurately modeling the structure of the subcutaneous tissue during RF heating, i.e. by considering the actual fibrous septa network, in order to accurately estimate thermal damage. In general, the geometry of

the fibrous septa of each patient should be accurately measured in order to calculate the correct dosimetry in RF treatments of subcutaneous tissue disorders, such as cellulite, lipomatosis, lipedema and Madelung's disease. Our findings could thus be used to design and develop novel devices and RF treatments for subcutaneous fat disorders.

The main limitation of this study is the lack of real electric, thermal and elastic values for the fibrous septa. In fact, we considered these septa as a collagen-like structure with characteristics similar to the dermis, which is a mere approximation. Moreover, the parameters used in the Arrhenius model (A and ΔE) were taken from skin, due to the lack of actual values for subcutaneous tissue comprised of fat lobules and fibrous septa. Future work should be conducted to measure these parameters in the case of fibroblasts, keratinocytes and adipocytes, not only for characterizing complete irreversible thermal damage, but also other non-ablative effects involving stimulating cells to produce new collagen.

Although the thermal dependence of the Young's modulus could have been included in this model, as in previous studies (Zhou *et al* 2010), these experimental data are always measured on complete skin, and no measurements on specific components of the subcutaneous tissue are presently available, especially for fibrous septa. Our findings suggest that this is a crucial element that should be taken into account in the electrical-thermo-elastic behavior.

7.6. Conclusions

We built a computational model for selective non-invasive, non-ablative RF heating of cutaneous and subcutaneous tissues with low and high conditions of fibrous septa density within the subcutaneous tissue. These models included not only electrical performance but also the thermo-elastic response, which provides information on the volumetric strain map (expansion and shrinkage) in the tissue during RF heating. Our results show that the structure of fibrous septa within subcutaneous tissue greatly affects the electrical and thermo-elastic response. The computational findings suggested that: 1) a higher density of fibrous septa enhances the strength of the electric field and the flux of electric current, and consequently

increases power absorption within subcutaneous tissue; 2) low spatial density fibrous septa has higher shrinkage; and 3) skin and muscle are subjected to higher thermal stresses than the subcutaneous tissue, with more intense changes at the junction between layers.

Table 7.1. Electrical, thermal and elastic properties of the elements employed in the computer modeling (Franco *et al* 2010, Pailler-Mattei *et al* 2008, Comley and Fleck 2010, Deng and Liu 2003, Lin 2005)

Element	σ (S/m)	k (W/m·K)	ρ (kg/m ³)	c (J/kg·K)	ω (kg/m ³ ·s)	E (kPa)	α (1/°C)
Skin	0.22	0.53	1200	3800	2	35	$6 \cdot 10^{-5}$
Fat	0.025	0.16	850	2300	0.6	2	$2.76 \cdot 10^{-5}$
Muscle	0.5	0.53	1270	3800	0.5	80	$4.14 \cdot 10^{-5}$
Septa	0.22*	0.53*	1200*	3800*	0**	0.09	$6 \cdot 10^{-5}$ *

σ , electric conductivity; k , thermal conductivity; ρ , density; c , specific heat; ω , blood perfusion rate; E , Young's Modulus; and α , thermal expansion coefficient.

* Assumption. ** The perfusion term in the septa is neglected (i.e. septa as solid).

Table 7.2. Electrical, thermal and elastic boundary conditions.

Location	Electric	Thermal	Elastic
Skin surface	$\{n \cdot \mathbf{J} = 0 \mid -W/2 < x < -L/2\}$, $\{V = V_0 \mid -L/2 < x < L/2\}$, $\{n \cdot \mathbf{J} = 0 \mid L/2 < x < W/2\}$	$\{n \cdot k \nabla T = h_{a-s}(T_a - T) \mid -W/2 < x < -L/2\}$ $\{T = T_r \mid -L/2 < x < L/2\}$, $\{n \cdot k \nabla T = h_{a-s}(T_a - T) \mid L/2 < x < W/2\}$	$\{u = 0 \mid -W/2 < x < W/2\}$
Muscle bottom	$\{V = 0 \mid -W/2 < x < W/2\}$	$\{T = T_c \mid -W/2 < x < W/2\}$	$\{u = 0 \mid -W/2 < x < W/2\}$
Left side	$\{n \cdot \mathbf{J} = 0 \mid l_s + l_{f+s} + l_m < y < 0\}$	$\{n \cdot k \nabla T = 0 \mid l_s + l_{f+s} + l_m < y < 0\}$	$\{u = free \mid l_s + l_{f+s} + l_m < y < 0\}$
Right side	$\{n \cdot \mathbf{J} = 0 \mid l_s + l_{f+s} + l_m < y < 0\}$	$\{n \cdot k \nabla T = 0 \mid l_s + l_{f+s} + l_m < y < 0\}$	$\{u = free \mid l_s + l_{f+s} + l_m < y < 0\}$

L: length of the RF applicator; l_s , l_{f+s} and l_m : Layer thickness of skin, fat and muscle respectively. W: width of the mathematical domain; T_a : ambient temperature; T_c : constant core body temperature, T_r : cooled plate (applicator) temperature; h_{a-s} : thermal transfer coefficient between air and skin surface.

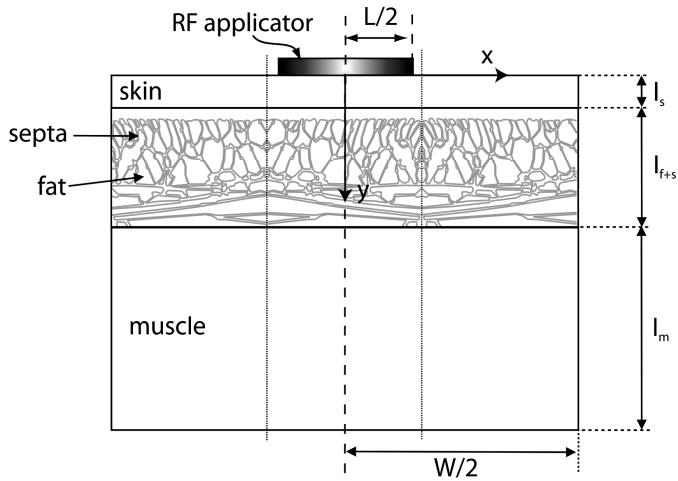


Figure 7.1. Geometry and dimensions of the model built, which is composed of three tissue layers of skin, fat+septa and muscle and RF applicator. l_i : thickness of each layer, where i represents skin (s), fat+septa ($f+s$) and muscle (m). W : width of each layer. L : length of the RF applicator. The subcutaneous tissue consists of a fine, collagenous, fibrous septa network enveloping fat clusters. Vertical dashed lines indicate the planes on which the geometry of the model was mirrored on the sides. Mathematical domain: $-W/2 < x < W/2$ and $(l_s + l_{f+s} + l_m) < y < 0$.

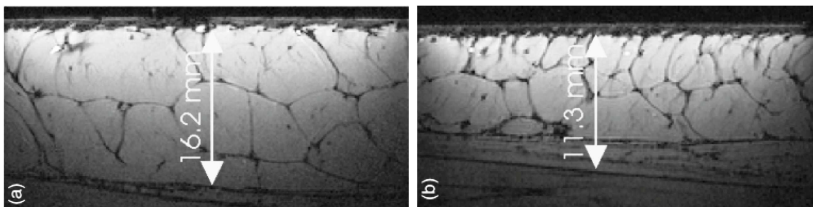


Figure 7.2. High-resolution in vivo MRIs of the skin of two females (Mirrashed *et al* 2004) corresponding with two conditions of density of fibrous septa: **(a)** Case 1: Low density (Cellulite Grade 2.5); and **(b)** Case 2: High density (Cellulite Grade 0, smooth skin). Dark filaments correspond to fibrous septa within the subcutaneous tissue.

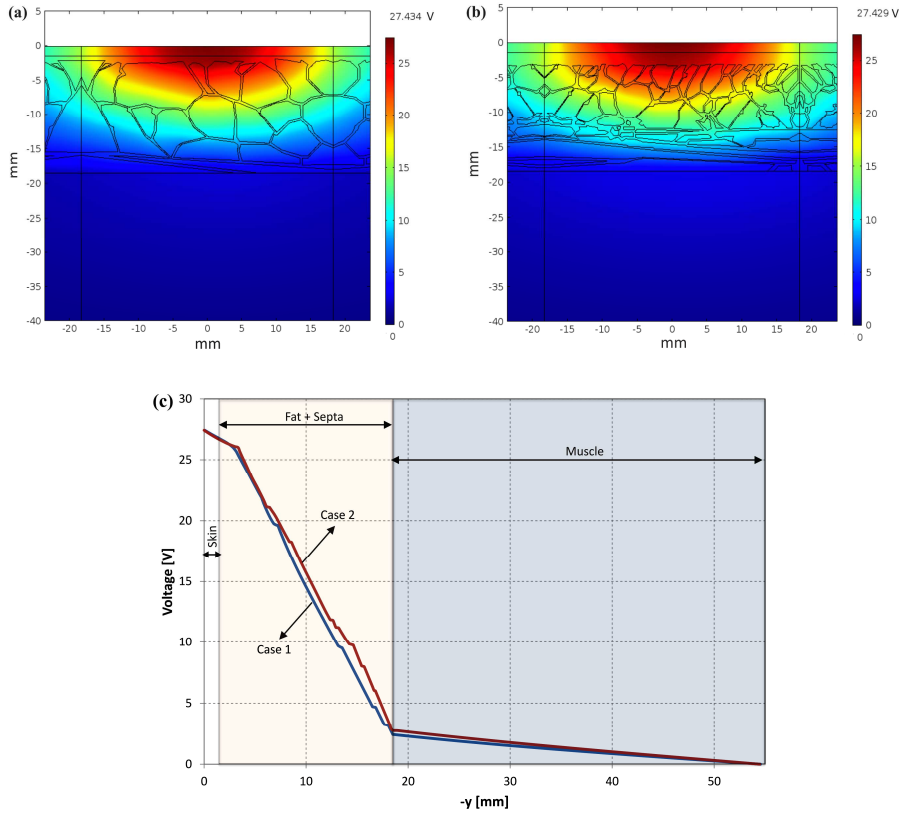


Figure 7.3. Voltage distribution in the tissue for two conditions of density of fibrous septa: (a) Case 1 (Jimenez Lozano *et al* 2013); and (b) Case 2. (c) Voltage profiles at $x = 0$. Note the voltage drop occurs mostly in the section fat+septa in both cases.

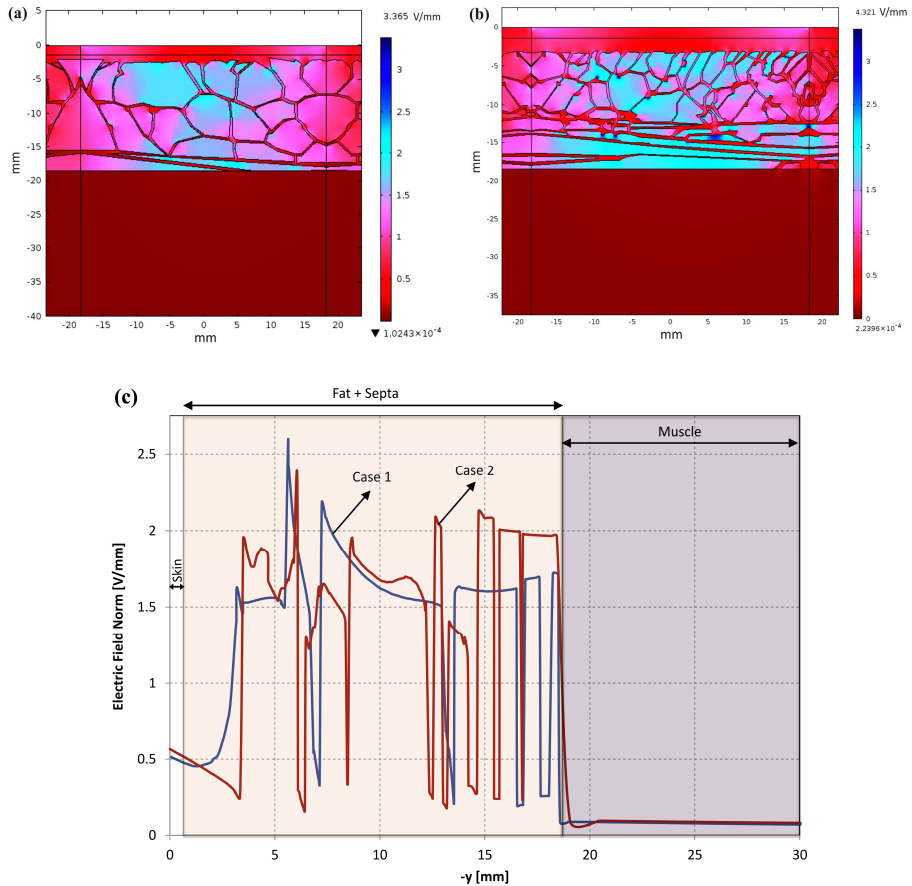


Figure 7.4. Electric field norm distribution within tissue for two conditions of density of fibrous septa: (a) Case 1 (Jimenez Lozano *et al* 2013); and (b) Case 2. Distributions scaled to 0–4.321 V/mm. (c) Comparison of the electric field norm profiles at $x = 0$.

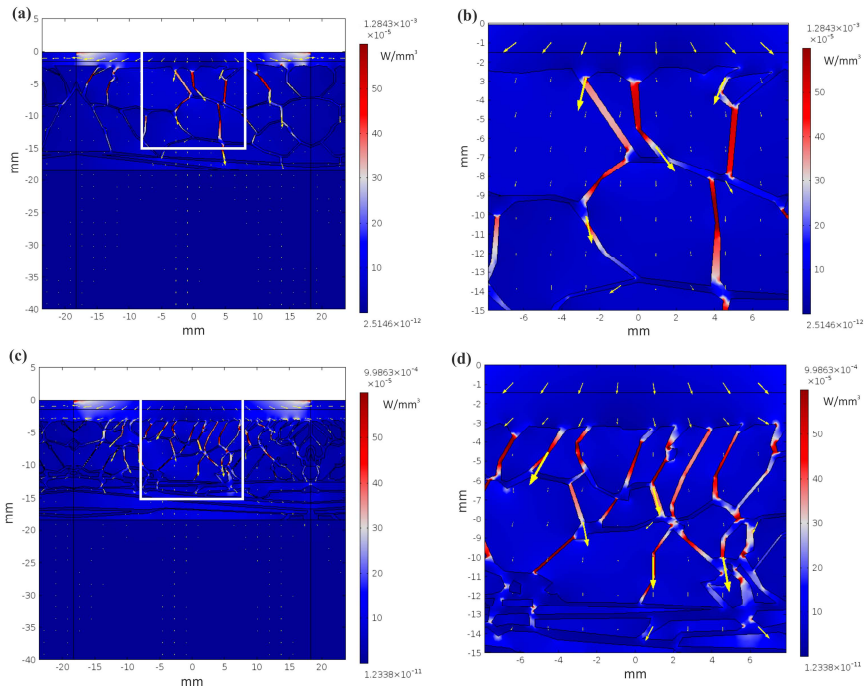


Figure 7.5. Total electric power absorption (surface map) and electric current density (arrows) for two conditions of density of fibrous septa: **(a)** Case 1 (Jimenez Lozano *et al* 2013) and **(c)** Case 2. **(b)** and **(d)** show close-up views of Cases 1 and 2, respectively. The white rectangle indicates the extended area in **(b)** and **(d)**.

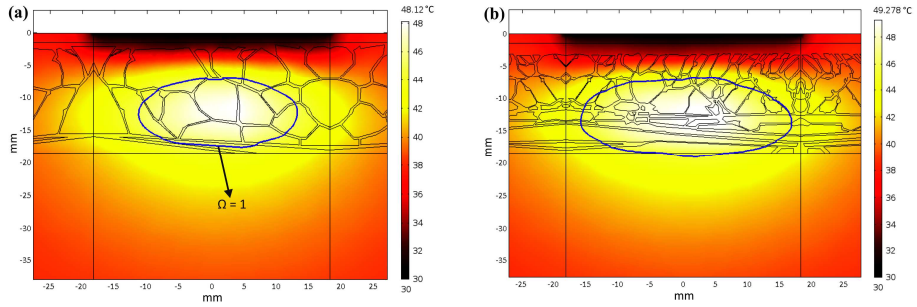


Figure 7.6. Temperature distribution (in °C) in the tissue after 8000 s of RF heating for two conditions of density of fibrous septa: (a) Case 1, and (b) Case 2. The solid line is the thermal damage contour ($\Omega = 1$).

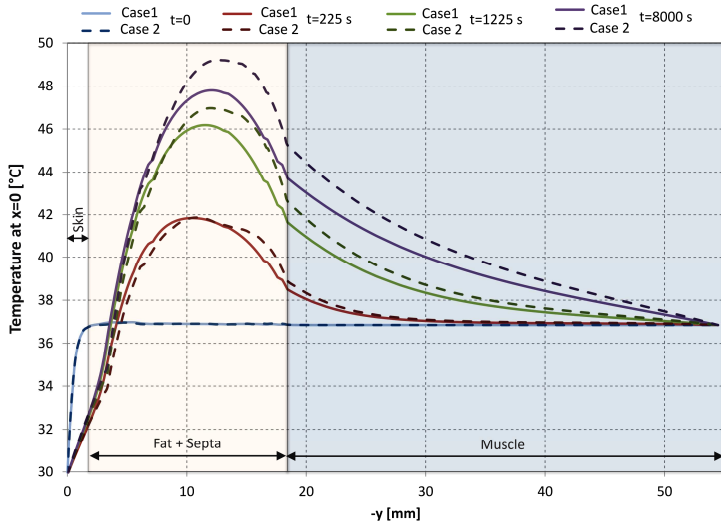


Figure 7.7. Time progression of depth profiles of temperature profiles at $x = 0$ for two conditions of density of fibrous septa: Case 1 and Case 2.

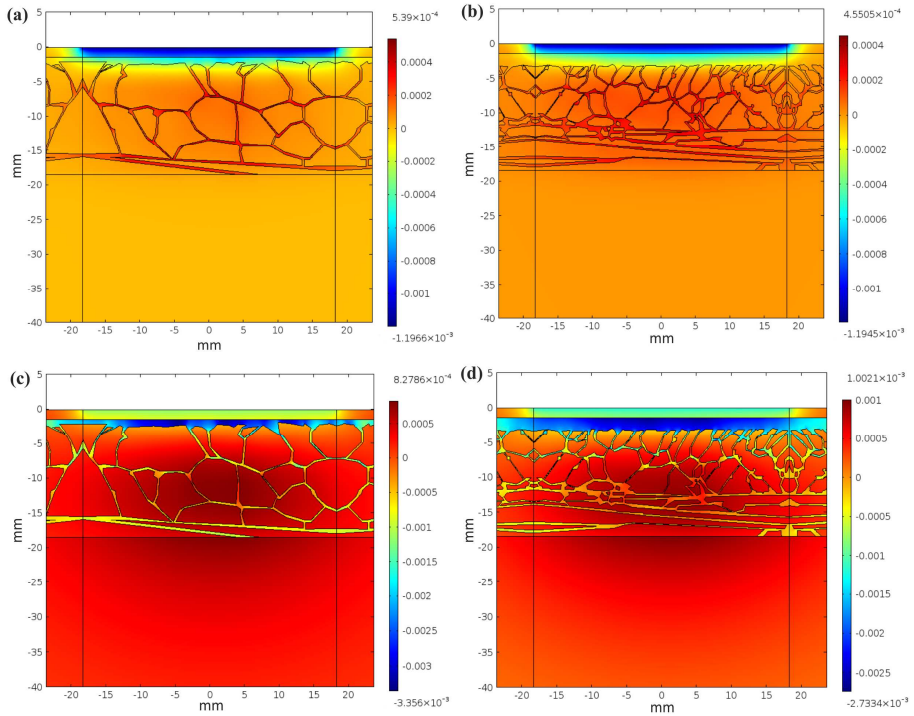


Figure 7.8. Volumetric strain map for two conditions of density of fibrous septa: (a) and (c) Case 1; (b) and (d) Case 2. Maps computed at two times during RF heating: 25 s in (a) and (b); and 8000 s in (c) and (d).

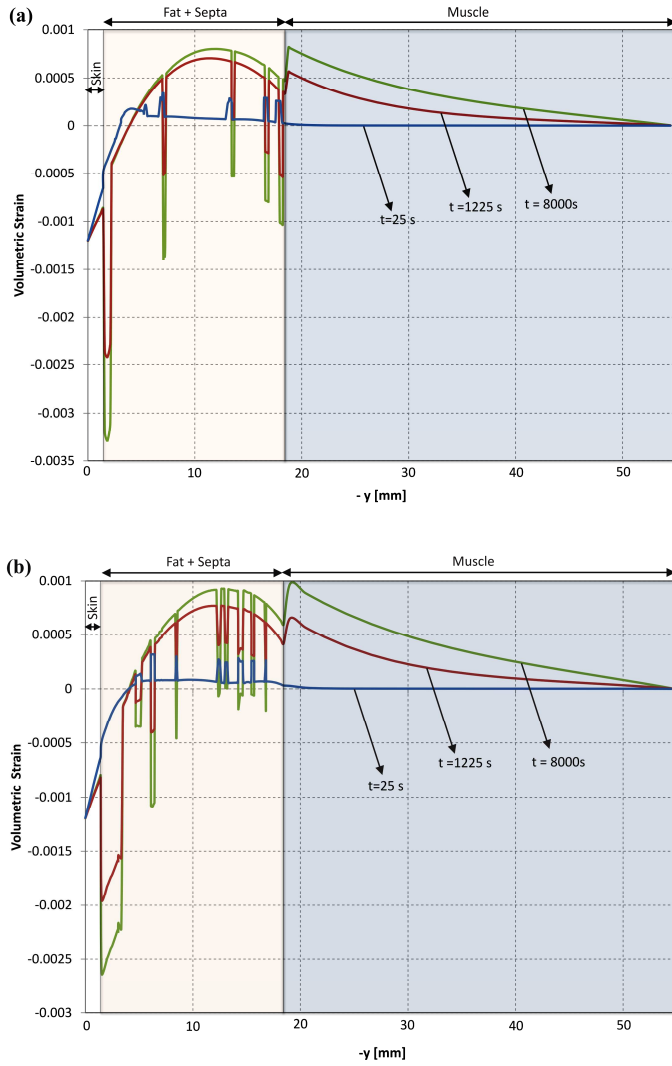


Figure 7.9. Time progress of the volumetric strain profiles at $x = 0$ for two conditions of density of fibrous septa: (a) Case 1; and (b) Case 2.

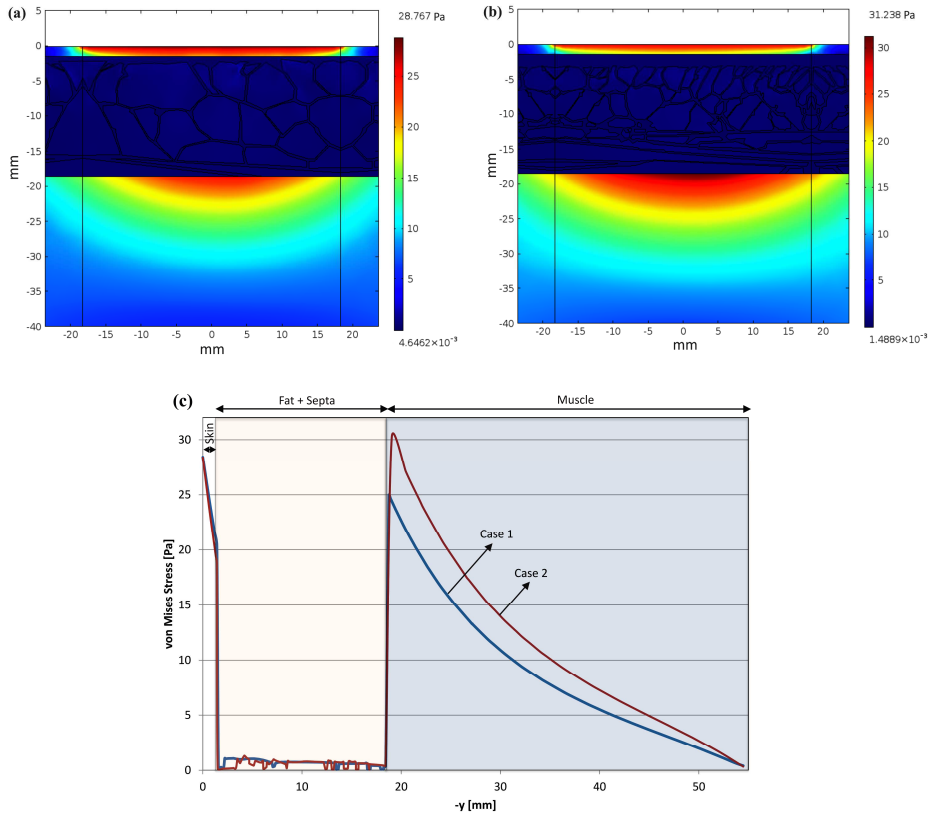


Figure 7.10. Stress distribution map of Von Mises Stress for two conditions of density of fibrous septa: (a) Case 1; and (b) Case 2. Von Mises Stress profile at $x = 0$ for both cases (c).

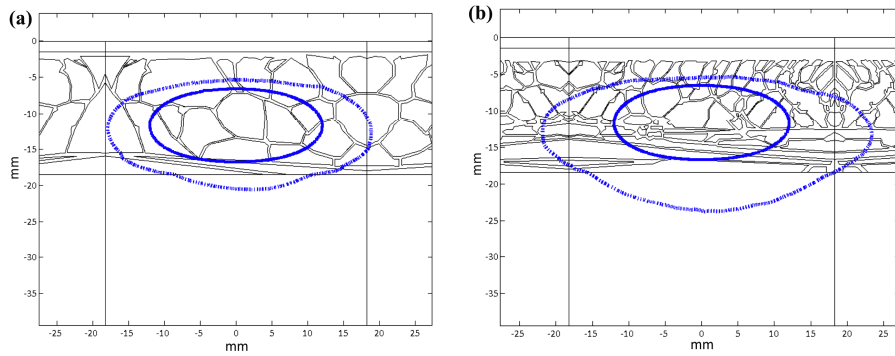


Figure 7.11. Thermal damage zones ($\Omega = 1$) computed after 8000 s of RF heating (200 W power) considering the subcutaneous tissue as a homogeneous layer (solid line) and for two conditions of fibrous septa density (dotted lines): **(a)** Case 1, and **(b)** Case 2.

Chapter 8

General discussion

The PhD Thesis focuses on developing computational and experimental models designed to study various aspects of the heating of biological tissues by RF currents, with the aim of discovering improved ablative techniques for use in treating cardiac, oncologic and dermatologic disorders.

The research on cardiac surgery was focused firstly on improving intraoperative ablation of atrial fibrillation by an epicardial approach (Chapters 2 and 3). As there are currently no devices capable of giving easy access to atrial tissue and automatically creating continuous transmural lesions in areas with overlying fat tissue (Kiser *et al* 2007), we believe our results are worth consideration. In Chapter 3, we proposed a new system based on measuring bioimpedance capable of accurately assessing the epicardial fat profile prior to RF atrial ablation. The next step should be to set up an *ex vivo* experimental model including myocardium and fatty tissue to validate the potential of the proposed procedure in estimating the overlying epicardial fat. Our results also suggest a future line of research to address the development of intelligent RF ablation systems which could respond to different adipose tissue thicknesses. This would allow fine-tuning the RF energy needed to ablate atrial tissue according to the thickness of epicardial fat of individual patients when treating atrial fibrillation.

Secondly, in Chapter 4, we focused on a computational study of the efficiency of different modes of RF cardiac ablation in terms of creating transmural

lesions in the ventricular wall by two catheters on opposite sides, when treating ventricular tachycardia. There are currently no comparative studies of these ablation modes according to the location of ventricular tachycardia, either in the interventricular septum (endocardial-endocardial approach) or in the ventricular free wall (endocardial-epicardial approach). Although our results could be a useful guide in the choice of ablation mode according to the site of the affected ventricular wall, in future work it would be interesting to check whether these results could be altered by using other catheter types (e.g. non-irrigated or open-irrigated). Furthermore, our computational models could be refined to include blood velocity in the ventricles, rather than using forced convection coefficients. This aspect would not affect either the temperature distribution in the tissue or the lesions created in the ventricular wall, but would provide a more realistic temperature distribution in the blood (Jain and Wolf 2000). Finally, it would also be interesting to conduct an experimental study using internally cooled electrodes (as used in our study) to assess the lesions created at both sites of the ventricular wall by the three different ablation modes. The comparison with the experimental results could validate our computational models.

As regards oncology, our research was focused on RF-assisted hepatic resection. In Chapter 5, we studied the capacity of an internally cooled bipolar RF device to coagulate hepatic tissue, for which we quantified the lesion depth created in a computational, ex vivo and in vivo model. Although currently internally cooled bipolar RF devices do exist, they have not so far been used in RF-assisted hepatic resection, but in other clinical applications. For instance, the Isolator device was used to create lesions in cardiac tissue in treating atrial fibrillation (Voeller *et al* 2010). The open-irrigated bipolar Aquamantys device is currently used in surgical resection, but, as far as we know, there are no detailed data on the lesion depth it created. It would therefore be of interest to conduct a comparative study on the lesion depth created in hepatic tissue between the bipolar device tested in our study (internally cooled electrodes) and the Aquamantys device (irrigated electrodes).

Also in the context of the RF-assisted hepatic resection, we focused on assessing whether the heat sink effect of the blood flow inside a vessel could protect

its wall in the proximity of a RF-assisted resection device (Chapter 6). The idea behind this is that some surgeons prefer using ultrasonic dissectors instead of RF devices to remove the tissue around the vessel. The theoretical rationale is to reduce the risk of thermal damage to the vessel, since ultrasonic dissectors do not produce deep thermal lesions (Sutton *et al* 2010). In our study, we observed that the heat sink effect caused by blood flow inside the vessel could in fact be a thermal protection mechanism under certain conditions (device-vessel distance and vessel-device position).

Finally, as regards dermatology, we focused on improving the current treatments for subcutaneous fat tissue diseases by RF heating techniques (Chapter 7). These techniques can produce localized and selective heating in the subcutaneous tissue without causing damage to other skin structures (epidermis and dermis) and muscle. However, there is currently a total lack of knowledge of the correct dosimetry of RF energy needed to treat a specific disease in the subcutaneous tissue, due to its being a non homogeneous tissue (i.e. it consists of a fibrous septa network enveloping clusters of adipocyte cells) and its structure varies between individuals. In our study, we assessed and quantified the thermal damage in two different structures of subcutaneous tissue after RF heating. Future work could address the design of an automatic control system capable of estimating the exact dosimetry from an analysis of the affected area. For this purpose, we have already begun a new study aimed at obtaining the parameters of the Arrhenius Equation (A and ΔE) for each of the cell types that compose subcutaneous tissue (fibroblasts, keratinocytes and adipocytes), since these parameters have not yet been experimentally estimated. After obtaining these parameters, they will be entered in the mathematical models to quantify thermal damage in the subcutaneous tissue in a more realistic way.

Chapter 9

Conclusions

The results of our research provide a better understanding of the electrical and thermal phenomena involved in certain medical techniques based on the heating of biological tissues by RF electrical currents. Some of the findings suggest changes that would improve the efficacy and safety in the current clinical practice, while others are used to propose technical improvements in designing more efficient and safer RF applicators. The specific conclusions of the research can be summarized as follows in relation to the objectives outlined in Chapter 1.

1.1. To study the effect of different procedural and anatomical factors on transmural lesion in atrial tissue during epicardial RF ablation.

The results of this study showed the difficulty of ablating the atrial wall underneath a thick epicardial fat layer, regardless of electrode design and power delivery protocol. The results suggest that this is due to the electrical conductivity of fat being much lower than that of atrial tissue. In addition, as fat also has a lower thermal conductivity than atrial tissue, the presence of this fat layer has a negative impact on creating transmural lesions. It can therefore be concluded that the epicardial fat layer seriously impedes the passage of RF current during epicardial RF cardiac ablation, thus reducing the effectiveness of ablation on the atrial wall.

Due to the current low efficacy of treating atrial fibrillation by RF cardiac ablation in an epicardial approach, our computational results could be used to improve present RF ablation techniques by assessing the capacity of different electrode designs and RF power delivery protocols.

1.2. To conduct a proof-of-concept of a new probe for assessing the amount of epicardial fat present prior to RF ablation.

The results of this study suggest that a technique based on impedance measurements could be an accurate method of quantifying epicardial fat prior to RF intraoperative cardiac ablation, i.e. to “map” the amount of adipose tissue under the probe. This is based on the fact that the impedance profiles obtained approximately coincided with the epicardial fat profiles present under the electrodes of the probe.

As the main impediment to ablating the atrial wall is the presence of overlying fat (see Conclusion 1.1), this result could be useful for improving current ablative techniques, since knowing the amount of epicardial fat present would make it possible to choose a particular RF power delivery protocol in order to optimize the thermal lesion.

1.3. To study the effect of different modes of RF cardiac ablation on transmural lesions in the ventricular wall by a pair of catheters placed on opposite sides of the wall.

The results of this study showed that the bipolar RF mode is superior to both unipolar modes in terms of achieving transmural lesions across the interventricular septum (endocardial-endocardial approach) and the ventricular free wall (endocardial-epicardial approach), even when the catheters are misaligned. The only situation in which the bipolar mode is inferior to unipolar modes is in the case of ventricular free wall ablation when there is air around the epicardial catheter tip. In this case, simultaneous unipolar mode is the only mode capable of creating transmural lesions.

These findings could be useful in guiding electrophysiologists to choose the most appropriate ablation mode to treat ventricular tachycardia by means of two catheters placed on opposite sides of the ventricular wall.

2.1. To study the electro-thermal behaviour of an internally cooled bipolar applicator for RF-assisted hepatic resection.

Both the theoretical and experimental results showed that an internally cooled bipolar RF applicator (5 mm diameter, 6 mm inter-electrode distance) could create sufficiently deep lesions in hepatic tissue (≈ 7 mm depth) to coagulate hepatic parenchyma and seal small vessels. This means a long thermal lesion could be made along the transection plane in order to minimize intraoperative blood loss during surgical resection. In addition, our results showed that the thermal lesion created is mainly confined to the area between the electrodes, which would make it possible to control lesion width by selecting a specific applicator design.

Although open-irrigation bipolar RF applicators are currently used to coagulate hepatic tissue, they have some drawbacks when compared with closed-irrigation applicators, including the risk of burning contiguous organs by hot saline. Our results therefore suggest that the use of internally cooled bipolar electrodes could improve safety while creating sufficiently deep lesions in the tissue or to seal vessels during surgical resection.

2.2. To study the heat sink effect inside a large vessel close to an internally cooled electrode during RF-assisted hepatic resection.

The experimental results showed that the heat sink effect inside a large vessel could protect its wall when the vessel is at a distance from the RF-assisted resection device equal to or greater than 7.4 mm. The computer results also confirmed that predictions can be made as to whether or not the vessel wall could be damaged at lower vessel-device distances. It is possible that the blood flow inside a large vessel (such as the portal vein) could protect its wall at distances equal to or

greater than 5 mm, regardless of its position with respect to the device and the device-tissue contact.

Knowing the conditions under which the heat sink effect inside the vessel thermally protects its wall could be useful to surgeons, since this could avoid the need for using ultrasonic dissectors to remove tissue around the vessel prior to RF-assisted resection.

3.1. To study the electrical, thermal and thermo-elastic effect of two different structures of fibrous septa within subcutaneous tissue during RF hyperthermic heating.

The results showed that the structure of fibrous septa within subcutaneous tissue greatly affects the electrical and thermo-elastic response. We observed that a higher density of fibrous septa enhances the strength of the electric field and the flux of electric current, as well as increasing the power absorption within subcutaneous tissue, which implies greater heating and thermal damage in this region. The lower the spatial density of fibrous septa the higher the shrinkage, and skin and muscle are subjected to higher thermal stresses than the subcutaneous tissue.

These findings demonstrate the importance of considering the real structure of the subcutaneous tissue when modeling RF heating of subcutaneous tissue and could be used to make an accurate estimate of thermal damage after RF heating. This would make it possible to apply the correct dosimetry in treating subcutaneous fat disorders by RF heating.

References

- Abraham JP and Sparrow EM 2007 A thermal-ablation bioheat model including liquid-to-vapor phase change, pressure- and necrosis-dependent perfusion, and moisture-dependent properties *Int. J. Heat Mass Tran.* **50**(13-14) 2537-2544
- Antunes CL, Almeida TR and Raposeiro N 2012 Saline-enhanced RF ablation on a cholangiocarcinoma: a numerical simulation *COMPEL: The International Journal for Computational and Mathematics in Electrical and Electronic Engineering* **31** 1050-1066
- Arita J, Hasegawa K, Kokudo N, Sano K, Sugawara Y and Makuuchi M 2005 Randomized clinical trial of the effect of a saline-linked radiofrequency coagulator on blood loss during hepatic resection *Br. J. Surg.* 2005 **92**(8) 954-959
- Ayav A, Jiao L, Dickinson R, Nicholls J, Milicevic M, Pellicci R, Bachellier P and Habib N 2008 Liver resection with a new multiprobe bipolar radiofrequency device *Arch. Surg.* 2008 **143**(4) 396-401
- Ba M, Fornés P, Nutu O, Latrémouille C, Carpentier A and Chachques JC 2008 Treatment of atrial fibrillation by surgical epicardial ablation: bipolar radiofrequency versus cryoablation *Arch. Cardiovasc. Dis.* **101**(11-12) 763-768
- Bangard C, Gossmann A, Kasper HU, Hellmich M, Fischer JH, Hölscher A, Lackner K and Stippel DL 2006 Experimental radiofrequency ablation near the portal and the hepatic veins in pigs: differences in efficacy of a monopolar ablation system *J. Surg. Res.* **135**(1) 113-119

- Benjamin EJ, Levy D, Vaziri SM, D'Agostino RB, Belanger AJ and Wolf PA 1994 Independent risk factors for atrial fibrillation in a population-based cohort. The Framingham Heart Study *JAMA* **271**(11) 840-844
- Berjano E and d'Avila A 2013 Lumped element electrical model based on three resistors for electrical impedance in radiofrequency cardiac ablation: estimations from analytical calculations and clinical data *Open Biomed. Eng. J.* **7** 62-70
- Berjano EJ 2006 Theoretical modeling for radiofrequency ablation: state-of-the-art and challenges for the future *Biomed. Eng. Online* **5** 24
- Berjano EJ 2008 Ablación quirúrgica. Fuentes de energía y tecnología *Cir. Cardio.* **15**(4) 375-383
- Berjano EJ and Hornero F 2004 Thermal-electrical modeling for epicardial atrial radiofrequency ablation *IEEE Trans. Biomed. Eng.* **51**(8) 1348-1357
- Berjano EJ and Hornero F 2005a A cooled intraesophageal balloon to prevent thermal injury during endocardial surgical radiofrequency ablation of the left atrium: a finite element study *Phys. Med. Biol.* **50** 269-279
- Berjano EJ and Hornero F 2005b What affects esophageal injury during radiofrequency ablation of the left atrium? An engineering study based on finite-element analysis. *Physiol. Meas.* **26** 837-848
- Berjano EJ and Hornero F 2006 Esophageal temperature during radiofrequency catheter ablation of left atrium: a three-dimensional computer modeling study *J. Cardiovasc. Electrophysiol.* **17** 405-410
- Berjano EJ, Burdío F, Navarro AC, Burdío JM, Güemes A, Aldana O, Ros P, Sousa R, Lozano R, Tejero E and Gregorio MA 2006 Improved perfusion system for bipolar radiofrequency ablation of liver *Physiol. Meas.* **27**(10) 55-66
- Berjano EJ, Navarro E, Ribera V, Gorris J and Alió JL 2007 Radiofrequency Heating of the Cornea: An Engineering Review of Electrodes and Applicators *The Open Biomedical Engineering Journal* **6** 71-76
- Berjano EJ, Romero-Méndez R and Franco W 2010 Radiofrequency based on hyperthermia therapy: a centennial technique serving modern surgery *Revista Mexicana de Ingeniería Biomédica* **31**(2) 142-153

- Bhattacharya A and Mahajan RL 2005 Temperature dependence of thermal conductivity of biological tissues *Physiol. Meas.* **24**(3) 769-783
- Blaauw Y and Crijns HJ 2007 Atrial fibrillation: insights from clinical trials and novel treatment options *J. Intern. Med.* **262**(6) 593-614
- Brankov JG, Danchev DM and Tonchev NS 2000 Theory of critical phenomena in finite-size systems. Scarling and quantum effects (Singapore: World Scientific)
- Burdío F, Berjano EJ, Navarro A, Burdío JM, Grande L, González A, Cruz I, Güemes A, Sousa R, Subiró J, Castiella T, Poves I and Lequerica JL 2009 Research and development of a new RF-assisted device for bloodless rapid transection of the liver: Computational modeling and in vivo experiments *Biomed. Eng. Online* **8** 6
- Burdío F, Berjano EJ, Navarro A, Burdío JM, Güemes A, Grande L, Sousa R, Subiró J, Gonzalez A, Cruz I, Castiella T, Tejero E, Lozano R and de Gregorio MA 2007 RF tumor ablation with internally cooled electrodes and saline infusion: what is the optimal location of the saline infusion? *Biomed. Eng. Online* **6** 30.
- Burdío F, Grande L, Berjano E, Martinez-Serrano M, Poves I, Burdío JM, Navarro A and Güemes A 2010 A new single-instrument technique for parenchyma division and hemostasis in liver resection: a clinical feasibility study *Am. J. Surg.* **200**(6) e75-80.
- Burdío F, Navarro A, Berjano E, Sousa R, Burdío JM, Güemes A, Subiró J, Gonzalez A, Cruz I, Castiella T, Tejero E, Lozano R, Grande L and de Gregorio MA 2008 A radiofrequency-assisted device for bloodless rapid transection of the liver: A comparative study in a pig liver model *Eur. J. Surg. Oncol.* **34**(5) 599-605.
- Byeongman J and Alptekin A 2010 Prediction of the extent of thermal damage in the cornea during conductive keratoplasty *J. Therm. Biol.* **35**(4) 167-174
- Chang I and Nguyen U 2004 Thermal modelling of lesion growth with radiofrequency ablation devices *Biomed. Eng. Online* **3**(1) 27

- Chang IA 2010 Considerations for thermal injury analysis for RF ablation devices
Open Biomed. Eng. J. **4** 3-12
- Chen X and Saidel GM 2009 Mathematical modeling of thermal ablation in tissue surrounding a large vessel *J. Biomech. Eng.* **131**(1) 011001
- Cioni JL, D'Alimonte P, Cristani A, Ventura P, Abbati G, Tincani E, Romagnoli R and Ventura E 1992 Duplex-Doppler assessment of cirrhosis in patients with chronic compensated liver disease *J. Gastroenterol. Hepatol.* **7**(4) 382-384
- Comley K and Fleck NA 2010 A micromechanical model for the Young's modulus of adipose tissue *Int. J. Solids Structures* **47**(21) 2982-2990
- Consiglieri L 2012 Continuum models for the cooling effect of blood flow on thermal ablation techniques *Int. J. Thermophys.* **33** 864-884
- Consiglieri L, Dos Santos I and Haemmerich D 2003 Theoretical analysis of the heat convection coefficient in large vessels and the significance for thermal ablative therapies *Phys. Med. Biol.* **48** 4125-4134
- Cooper JM, Sapp JL, Tedrow U, Pellegrini CP, Robinson D, Epstein LM and Stevenson WG 2004 Ablation with an internally irrigated radiofrequency catheter: learning how to avoid steam pops *Heart Rhythm* **1**(3) 329-333
- Cox JL, Schuessler RB, Lappas DG and Boineau JP 1996 An 8 1/2-year clinical experience with surgery for atrial fibrillation *Ann. Surg.* **224** 267-273
- Cushing H and Bovie WT 1928 Electro-surgery as an aid to the removal of intracranial tumors *Surg. Gynecol. Obstet.* **47** 751-784.
- d'Arsonval A 1981 Action physiologique des courants alternatifs *Soc. Biol.* **43** 283-386
- Dadd JS, Ryan TP and Platt R 1996 Tissue impedance as a function of temperature and time *Biomed. Sci. Instrum.* **32** 205-214
- d'Avila A, Houghtaling C, Gutiérrez P, Vragovic O, Ruskin JN, Josephson ME and Reddy VY 2004 Catheter ablation of ventricular epicardial tissue: a comparison of standard and cooled-tip radiofrequency energy *Circulation* **109**(19) 2363-2369

- Demazumder D, Mirotznik MS and Schwartzman D 2001 Comparison of irrigated electrode designs for radiofrequency ablation of myocardium *J. Interv. Card. Electrophysiol.* **5**(4) 391-400
- Deneke T, Khargi K, Müller KM, Lemke B, Mügge A, Laczkovics A, Becker AE and Grewe PH 2005 Histopathology of intraoperatively induced linear radiofrequency ablation lesions in patients with chronic atrial fibrillation *Eur. Heart J.* **26** 1797-1803
- Deng Z-S and Liu J 2003 Non-Fourier heat conduction effect on prediction of temperature transients and thermal stress in skin cryopreservation *J. Thermal Stresses* **26**(8) 7779-7798
- Dierickx CC 2006 The role of deep heating for noninvasive skin rejuvenation *Laser Surg. Med.* **38**(9) 799–807
- Dorcaratto D, Burdío F, Fondevila D, Andaluz A, Poves I, Martinez MA, Quesada R, Berjano E and Grande L 2012 Laparoscopic distal pancreatectomy: feasibility study of radiofrequency-assisted transection in a porcine model *J. Laparoendosc. Adv. Surg. Tech. A.* **22**(3) 242-248
- Dos Santos I, Haemmerich D, Pinheiro Cda S and da Rocha AF 2008 Effect of variable heat transfer coefficient on tissue temperature next to a large vessel during radiofrequency tumor ablation *Biomed. Eng. Online* **7** 21
- Doss JD 1982 Calculation of electric fields in conductive media *Med. Phys.* **9**(4) 566-573
- Duck F 1990 Physical properties of tissue - A comprehensive reference book (New York: Academic Press)
- Dukkipati SR, d'Avila A, Soejima K, Bala R, Inada K, Singh S, Stevenson WG, Marchlinski FE and Reddy VY 2011 Long-term outcomes of combined epicardial and endocardial ablation of monomorphic ventricular tachycardia related to hypertrophic cardiomyopathy *Circ. Arrhythm. Electrophysiol.* **4**(2) 185-194
- Dumas JH, Himel HD, Kiser AC, Quint SR and Knisley SB 2008 Myocardial electrical impedance as a predictor of the quality of RF-induced linear lesions *Physiol. Meas.* **29** 1195-1207

- Everett TH 4th, Lee KW, Wilson EE, Guerra JM, Varosy PD and Olgin JE 2009 Safety profiles and lesion size of different radiofrequency ablation technologies: a comparison of large tip, open and closed irrigation catheters *J. Cardiovasc. Electrophysiol.* **20**(3) 325-335
- Franco W, Kothare A and Goldberg D J 2009 Controlled volumetric heating of subcutaneous adipose tissue using a novel radiofrequency technology *Lasers Surg. Med.* **41** 745–750
- Franco W, Kothare A, Ronan SJ, Grekin RC and McCalmont TH 2010 Hyperthermic injury to adipocyte cells by selective heating of subcutaneous fat with a novel radiofrequency device: Feasibility studies *Lasers Surg. Med.* **42**(5) 361-370
- Franco W, Liu J, Romero-Méndez R, Jia W, Nelson JS and Aguilar G 2007 Extent of lateral epidermal protection afforded by a cryogen spray against laser irradiation *Lasers Surg. Med.* **39**(5) 414-421
- Gabriel S, Lau RW and Gabriel C 1996 The dielectric properties of biological tissues: III. Parametric models for the dielectric spectrum of tissues *Phys. Med. Biol.* **41**(11) 2271-2293
- Geddes LA 1989 Detection of physiological events by impedance. Principles of Applied Biomedical Instrumentation *Wiley Interscience* **1** 276-410
- Gnerlich JL, Ritter JH, Linehan DC, Hawkins WG and Strasberg SM 2009 Saline-linked surface radiofrequency ablation: a safe and effective method of surface ablation of hepatic metastatic colorectal cancer *Ann. Surg.* **250**(1) 96-102
- Goldberg SN, Grassi CJ, Cardella JF, Charboneau JW, Dodd 3rd GD, Dupuy DE, Gervais D, Gillams AR, Kane RA, Lee Jr FT, Livraghi T, McGahan J, Phillips DA, Rhim H and Silverman SG 2005 Society of Interventional Radiology Technology Assessment Committee; International Working Group on Image-Guided Tumor Ablation; Image-guided tumor ablation: Standardization of terminology and reporting criteria *Radiology* **235**(3) 728-739

-
- González-Suárez A, Alba J, Trujillo M and Berjano E 2011 Experimental and theoretical study of an internally cooled bipolar electrode for RF coagulation of biological tissues *Conf. Proc. IEEE Eng. Med. Biol. Soc.* 6878-6881
- González-Suárez A, Berjano EJ and Hornero F 2009 Assessment of the epicardial fat prior to RF cardiac ablation: concept proof using computational modeling *Proc. of the XXVII Ann. Meeting of the Biomedical Engineering Spanish Society (Cádiz, Spain)* pp 279-82.
- González-Suárez A, Hornero F and Berjano EJ 2010a Mathematical Modeling of Epicardial RF Ablation of Atrial Tissue with Overlying Epicardial Fat *TOBEJ* **4** 47-55
- González-Suárez A, Hornero F and Berjano EJ 2010b Impedance measurement to assess epicardial fat prior to RF intraoperative cardiac ablation: a feasibility study using a computer model *Physiol. Meas.* **31**(11) N95-104
- González-Suárez A, Trujillo M, Burdío F, Andaluz A and Berjano E 2012 Feasibility study of an internally cooled bipolar applicator for RF coagulation of hepatic tissue: Experimental and computational study *Int. J. Hyperthermia* **28**(7) 663-673
- Gopalakrishnan J 2002 A mathematical model for irrigated epicardial radiofrequency ablation *Ann. Biomed. Eng.* **30**(7) 884-893
- Gray S 1990 *Gray's Anatomy* (New York: Vintage Books)
- Grimmes S and Martinsen OG 2008 *Bioimpedance and Bioelectricity Basics* 2nd edn (Oxford: Academic Press)
- Haemmerich D and Wood BJ 2006 Hepatic radiofrequency ablation at low frequencies preferentially heats tumour tissue *Int. J. Hyperthermia* **22**(7) 563-574
- Haemmerich D, Chachati L, Wright AS, Mahvi DM, Lee FT and Webster JG 2003a Hepatic radiofrequency ablation with internally cooled probes: effect of coolant temperature on lesion size *IEEE Trans. Biomed. Eng.* **50**(4) 493-499
- Haemmerich D, Schutt DJ, dos Santos I, Webster JG and Mahvi DM 2005 Measurement of temperature-dependent specific heat of biological tissues *Physiol. Meas.* **26**(1) 59-67
-

- Haemmerich D, Wright AW, Mahvi DM, Lee Jr FT and Webster JG 2003b Hepatic bipolar radiofrequency ablation creates coagulation zones close to blood vessels: a finite element study *Med. Biol. Eng. Comput.* **41**(3) 317-323
- Haines DE and Watson DD 1989 Tissue heating during radiofrequency catheter ablation: a thermodynamic model and observations in isolated perfused and superfused canine right ventricular free wall *Pacing Clin. Electrophysiol.* **12**(6) 962-976
- Haïssaguerre M, Gencel L, Fischer B, Métayer PL, Poquet F, Marcus FI, and Clémenty J 1994 Successful catheter ablation of atrial fibrillation *J. Cardiovasc. Electrophysiol.* **5** 1045–1054
- Henriques FC and Moritz AR 1947 Studies of Thermal Injury: I. The Conduction of Heat to and through Skin and the Temperatures Attained Therein. A Theoretical and an Experimental Investigation *Am. J. Pathol.* **23**(4) 530-549
- Hong KN, Russo MJ, Liberman EA, Trzebucki A, Oz MC, Argenziano M and Williams MR 2007 Effect of epicardial fat on ablation performance: a three-energy source comparison *J. Card. Surg.* **22**(6) 521-524
- Huang HW 2013 Influence of blood vessel on the thermal lesion formation during radiofrequency ablation for liver tumors *Med Phys.* **40**(7) 073303
- Huang SK, Bharati S, Graham AR, Lev M, Marcus FI and Odell RC 1987 Closed chest catheter desiccation of the atrioventricular junction using radiofrequency energy: a new method of catheter ablation *J. Am. Coll. Cardiol.* **9** 349-358
- Incropera FP, DeWitt DP, Bergman TL and Lavine AS 2006 *Fundamentals of Heat and Mass Transfer* 6th ed (John Wiley & Sons Inc Hoboken)
- Jacques S, Rastegar S, Thomsen S and Motamedi M 1996 Nonlinear finite-element analysis of the role of dynamic changes in blood perfusion and optical properties in laser coagulation of tissue *IEEE J. Sel. Top Quantum Electron.* **2** 922-933
- Jacques SL and Gaenli MO 1989 Thermally induced changes in optical properties of heart *Proc. 11th Ann. Int. Conf. of the IEEE Eng. Med. Biol. Soc.* **4** 1199–1200

- Jain MK and Wolf PD 1999 Temperature-controlled and constant-power radio-frequency ablation: what affects lesion growth? *IEEE Trans. Biomed. Eng.* **46**(12) 1405-1412
- Jain MK and Wolf PD 2000 A three-dimensional finite element model of radiofrequency ablation with blood flow and its experimental validation *Ann. Biomed. Eng.* **28**(9) 1075-1084
- Jain MK, Wolf PD and Henríquez C 1995 Chilled-tip electrode radio frequency ablation of the endocardium: a finite element study *Proceedings of the 17th Annual Conference of the IEEE Engineering in Medicine and Biology Society (IEEE-EMBS)* 273-274
- Jimenez Lozano JN, Vacas-Jacques P, Anderson RR and Franco W 2013 Effect of fibrous septa in radiofrequency heating of cutaneous and subcutaneous tissues: computational study *Lasers Surg. Med.* **45**(5) 326-338
- Kannel WB, Wolf PA, Benjamin EJ and Levy D 1998 Prevalence, incidence, prognosis, and predisposing conditions for atrial fibrillation: population-based estimates *Am. J. Cardiol.* **82** 2N-9N
- Khargi K, Hutten BA, Lemke B and Deneke T 2005 Surgical treatment of atrial fibrillation; a systematic review *Eur. J. Cardiothorac. Surg.* **27** 258-265
- Kiser AC, Wimmer-Greinecker G and Chitwood WR 2007 Totally extracardiac Maze procedure performed on the beating heart *Ann. Thorac. Surg.* **84**(5) 1783-1785
- Koovor P, Eipper VE, Dewsnap BI, McKinley S, Nguyen HT, Uther JB and Ross DL 1996 The effect of different frequencies on lesion size during radiofrequency ablation *Circulation* **94** I677
- Kröger T, Preusser T and Peitgen H-O. Blood Flow Induced Cooling Effect in Radio Frequency Ablation for Hepatic Carcinoma, *IPAM UCLA* May 19–23, 2008
- Kumar P, Mounsey JP, Gehi AK, Schwartz JD and Chung EH 2013 Use of a closed loop irrigated catheter in epicardial ablation of ventricular tachycardia *J. Interv. Card. Electrophysiol.* **38**(1) 35-42
- Latchamsetty R and Oral H 2012 Ablation of atrial fibrillation using an irrigated-tip catheter: open or closed? *Pacing Clin. Electrophysiol.* **35**(5) 503-505

- Leen E and Horgan PG 2007 Radiofrequency ablation of colorectal liver metastases *Surg. Oncol.* **16**(1) 47–51
- Lehmann KS, Ritz JP, Valdeig S, Knappe V, Schenk A, Weihusen A, Rieder C., Holmer C, Zurbuchen U, Hoffmann P, Peitgen HO, Buhr HJ and Frericks BB 2009 Ex situ quantification of the cooling effect of liver vessels on radiofrequency ablation *Langenbecks Arch. Surg.* **394**(3) 475-481
- Lin JC 2005 Microwave Thermoelastic Tomography and Imaging *Advances in Electromagnetic Fields in Living Systems* **4** 41-76
- Lolis MS and Goldberg DJ 2012 Radiofrequency in cosmetic dermatology: A review *Dermatol. Surg.* **38**(11) 1765–1776
- Marchal F, Elias D, Rauch P, Zarnegar R, Leroux A, Verhaeghe JL, Guillemin F, Carteaueb JP and Villemont JP 2006 Prevention of biliary lesions that may occur during radiofrequency ablation of the liver: study on the pig *Ann. Surg.* **243** (1) 82-88
- Melo J, Adragao P, Neves J, Ferreira MM, Timoteo A, Santiago T, Ribeiros R and Canada M 2000 Endocardial and epicardial radiofrequency ablation in the treatment of atrial fibrillation with a new intra-operative device *Eur. J. Cardio-Thorac. Surg.* **18** 182–186
- Metcalfé MS, Mullin EJ, Texler M, Berry DP, Dennison AR and Maddern GJ 2007 The safety and efficacy of radiofrequency and electrolytic ablation created adjacent to large hepatic veins in a porcine model *Eur. J. Surg. Oncol.* **33**(5) 662-667
- Miklavčič D, Pavšelj N and Hart FX 2006 Electric properties of tissues *Wiley Encyclopedia of Biomedical Engineering*
- Mirrashed F, Sharp JC, Krause V, Morgan J and Tomanek B 2004 Pilot study of dermal and subcutaneous fat structures by MRI in individuals who differ in gender, BMI, and cellulite grading *Skin Research and Technology* **10**(3) 161-168
- Mitnovetski S, Almeida AA, Goldstein J, Pick AW and Smith JA 2009 Epicardial high-intensity focused ultrasound cardiac ablation for surgical treatment of atrial fibrillation *Heart Lung Circ.* **18**(1) 28-31

- Miyagi Y, Ishii Y, Nitta T, Ochi M and Shimizu K 2009 Electrophysiological and histological assessment of transmural ablation after epicardial ablation using unipolar radiofrequency energy *J. Card. Surg.* **24**(1) 34-40
- Moritz AR and Henriques FC 1947 Studies of Thermal Injury: II. The Relative Importance of Time and Surface Temperature in the Causation of Cutaneous Burns *Am. J. Pathol.* **23**(5) 695-720
- Nagashima K, Watanabe I, Okumura Y, Ohkubo K, Kofune M, Ohya T, Kasamaki Y and Hirayama A 2011 Lesion formation by ventricular septal ablation with irrigated electrodes: comparison of bipolar and sequential unipolar ablation *Circ. J.* **75**(3)565–570
- Nagashima K, Watanabe I, Okumura Y, Sonoda K, Kofune M, Mano H, Ohkubo K, Nakai T, Kunimoto S, Kasamaki Y and Hirayama A 2012 Epicardial ablation with irrigated electrodes: – effect of bipolar vs. unipolar ablation on lesion formation – *Circ. J.* **76**(2) 322-327
- Nakajima H, Kobayashi J, Bando K, Niwaya K, Tagusari O, Sasako Y, Nakatani T and Kitamura S 2002 The effect of cryo-maze procedure on early and intermediate term outcome in mitral valve disease: case matched study *Circulation* **106** 146-150
- Nerst W 1908 Zur Theorie des elektrischen Reizes *Pflügers Arch.* **122**:275
- Ng KK, Lam CM, Poon RT, Shek TW, Fan ST and Wong J 2004 Delayed portal vein thrombosis after experimental radiofrequency ablation near the main portal vein *Br. J. Surg.* **91**(5) 632-639
- Pai M, Spalding D, Jiao L and Habib N 2012 Use of bipolar radiofrequency in parenchymal transection of the liver, pancreas and kidney *Dig. Surg.* **29**(1) 43-47
- Pailler-Mattei C, Bec S and Zahouani H 2008 In vivo measurements of the elastic mechanical properties of human skin by indentation tests *Med. Eng. Physics* **30**(5) 599-606

- Panescu D, Fleischman SD, Wayne JG and Swanson DK 1995a Temperature distribution under cooled electrodes during radiofrequency catheter ablation *Proceedings of the 17th Annual Conference of the IEEE Engineering in Medicine and Biology Society (IEEE-EMBS)* 299-300
- Panescu D, Wayne JG, Fleishman SD, Mirotznik MS, Swanson DK and Webster JG 1995b Three-dimensional finite element analysis of current density and temperature distributions during radio-frequency ablation *IEEE Trans. Biomed. Eng.* **42**(9) 879-890
- Pasic M, Bergs P, Müller P, Hofmann M, Grauhan O, Kuppe H and Hetzer R 2001 Intraoperative radiofrequency maze ablation for atrial fibrillation: The berlin modification *Ann. Thorac. Surg.* **72** 1484-1491
- Pätz T, Körger T, Preusser T 2009 Simulation of Radiofrequency Ablation Including Water Evaporation *IFMBE Proceedings 25/IV of World Congress on Medical Physics and Biomedical Engineering* 1287-1290.
- Paul M and Mulholland RS 2009 A new approach for adipose tissue treatment and body contouring using radiofrequency-assisted liposuction *Aesthetic Plast. Surg.* **33**(5) 687-694
- Paul M, Blugerman G, Kreindel M and Mulholland RS 2011 Three-dimensional radiofrequency tissue tightening: a proposed mechanism and applications for body contouring *Aesthetic Plast. Surg.* **35**(1) 87-95
- Pearce J, Panescu D and Thomsen S 2005 Simulation of diopter changes in radio frequency conductive keratoplasty in the cornea *WIT Trans. Biomed. Health* **8** 469-477
- Pearce JA 1986 *Electrosurgery* (Cambridge: Chapman and Hall) 224-234
- Peng T, O'Neill D and Payne S 2011 Mathematical study of the effects of different intrahepatic cooling on thermal ablation zones *Conf. Proc. IEEE Eng. Med. Biol. Soc.* 6866-6869
- Pennes HH 1948 Analysis of tissue and arterial blood temperatures in the resting human forearm *J Appl. Physiol.* **1**(2) 93-122

- Petersen HH, Roman-Gonzalez J, Johnson SB, Hastrup Svendsen J, HaunsØ S and Packer DL 2004 Mechanisms for enlarging lesion size during irrigated tip radiofrequency ablation: is there a virtual electrode effect? *J. Interv. Cardiol.* **17**(3) 171-177
- Poon RT, Fan ST and Wong J 2005 Liver resection using a saline-linked radiofrequency dissecting sealer for transection of the liver *J. Am. Coll. Surg.* **200**(2) 308-313
- Pruitt JC, Lazzara RR and Ebra G 2007 Minimally invasive surgical ablation of atrial fibrillation: The thoracoscopic box lesion approach *J. Interv. Card. Electrophysiol.* **20**(3) 83-87
- Raman J S, Ishikawa S and Power J M 2002 Epicardial radiofrequency ablation of both atria in the treatment of atrial fibrillation: Experience in patients *Ann. Thorac. Surg.* **74**(5) 1506-1509
- Ríos JS, Zalabardo JM, Burdio F, Berjano E, Moros M, González A, Navarro A and Güemes A 2011 Single instrument for hemostatic control in laparoscopic partial nephrectomy in a porcine model without renal vascular clamping *J. Endourol.* **25**(6) 1005-1011
- Rivera MJ, López Molina JA, Trujillo M and Berjano EJ 2009 Theoretical modeling of RF ablation with internally cooled electrodes: comparative study of different thermal boundary conditions at the electrode-tissue interface *Math. Biosci. Eng.* **6**(3) 611-627
- Rosenberg AG 2007 Reducing blood loss in total joint surgery with a saline-coupled bipolar sealing technology *J. Arthroplasty* **22**(4 Suppl 1) 82-85
- Sadick N 2008 Tissue tightening technologies: fact or fiction *Aesthet. Surg. J.* **28**(2) 180-8
- Sadick NS and Makino Y 2004 Selective electro-thermolysis in aesthetic medicine: A review *Lasers Surg. Med.* **34**(2) 91-97
- Sakamoto Y, Yamamoto J, Kokudo N, Seki M, Kosuge T, Yamaguchi T, Muto T and Makuuchi M 2004 Bloodless liver resection using the monopolar floating ball plus ligasure diathermy: preliminary results of 16 liver resections *World J. Surg.* **28**(2) 166-172

- Santiago T, Melo J, Gouveia RH, Abecasis LM, Adragão P and Martins AP 2003a Epicardial radiofrequency applications: in vitro and in vivo studies on human atrial myocardium *Eur. J. Cardiothorac. Surg.* **24** 481-486
- Santiago T, Melo JQ, Gouveia RH and Martins AP 2003b Intra-atrial temperatures in radiofrequency endocardial ablation: histologic evaluation of lesions *Ann. Thorac. Surg.* **75** 1495-1501
- Schutt D, Berjano EJ and Haemmerich D 2009 Effect of electrode thermal conductivity in cardiac radiofrequency catheter ablation: a computational modeling study *Int. J. Hyperthermia* **25**(2) 99-107
- Shah J, Dos Santos I, Haemmerich D and Valvano JW 2005 Instrument to measure the heat convection coefficient on the endotelial surface of arteries and veins *Med. Biol. Eng. Comput.* **43**(4) 522-527
- Sitzmann JV and Greene PS 1994 Perioperative predictors of morbidity following hepatic resection for neoplasm. A multivariate analysis of a single surgeon with 105 patients *Ann. Surg.* **219**(1) 13-17
- Sivagangabalan G, Barry MA, Huang K, Lu J, Pouliopoulos J, Thomas SP, Ross D, Thiagalingam A and Kovoor P 2010 Bipolar ablation of the interventricular septum is more efficient at creating a transmural line than sequential unipolar ablation *Pacing Clin. Electrophysiol.* **33**(1) 16-26
- Sosa E, Scanavacca M, d'Avila A, Oliveira F and Ramires JA 2000 Nonsurgical transthoracic epicardial catheter ablation to treat recurrent ventricular tachycardia occurring late after myocardial infarction *J. Am. Coll. Cardiol.* **35**(6) 1442-1449
- Spicák J 2007 Treatment of gastroesophageal reflux disease: endoscopic aspects *Dig. Dis.* **25**(3) 183-187
- Sprunger J and Herrell SD 2005 Partial laparoscopic nephrectomy using monopolar saline-coupled radiofrequency device: Animal model and tissue effect characterization *J. Endourol.* **19** 513-519

- Stephenson K, Steinberg S, Hughes KS, Vetto JT, Sugarbaker PH and Chang AE 1988 Perioperative blood transfusions are associated with decreased time to recurrence and decreased survival after resection of colorectal liver metastases *Ann. Surg.* **208**(6) 679-687
- Steward DL 2004 Effectiveness of multilevel (tongue and palate) radiofrequency tissue ablation for patients with obstructive sleep apnea syndrome *Laryngoscope* **114** 2073-2084
- Sutton P A, Awad S, Perkins AC and Lobo DN 2010 Comparison of lateral thermal spread using monopolar and bipolar diathermy, the Harmonic Scalpel and the Ligasure *Br. J. Surg.* **97**(3) 428-433
- Takayama T, Makuuchi M, Kubota K, Harihara Y, Hui AM, Sano K, Ijichi M and Hasegawa K 2001 Randomized comparison of ultrasonic vs clamp transection of the liver *Arch. Surg.* **136**(8) 9922-9928
- Tepetes K 2008 Risks of the radiofrequency-assisted liver resection *J. Surg. Oncol.* **97**(2) 193
- Thomas SP, Guy DJ, Boyd AC, Eipper VE, Ross DL and Chard RB 2003 Comparison of epicardial and endocardial linear ablation using handheld probes *Ann. Thorac. Surg.* **75** 543-548
- Topp SA, McClurken M, Lipson D, Upadhyga GA, Ritter JH, Linehan D and Strasberg SM 2004 Saline-linked surface radiofrequency ablation: factors affecting steam popping and depth of injury in the pig liver *Ann. Surg.* **239**(4) 518-527
- Tungjitkusolmun S, Staelin ST, Haemmerich D, Tsai JZ, Webster JG, Lee Jr FT, Mahvi DM and Vorperian VR 2002 Three-dimensional finite element analyses for radio-frequency hepatic tumor ablation *IEEE Trans. Biomed. Eng.* **49** (1) 3-9
- VanSonnenberg E, McMullen W and Solbiati L 2005 *Tumor ablation: Principles and Practice* (Springer: New York)

- Voeller RK, Zierer A, Lall SC, Sakamoto S, Schuessler RB and Damiano Jr RJ 2010 Efficacy of a novel bipolar radiofrequency ablation device on the beating heart for atrial fibrillation ablation: a long-term porcine study *J. Thorac. Cardiovasc. Surg.* **140**(1) 203-208
- Watanabe I, Nuo M, Okumura Y, Ohkubo K, Ashino S, Kofune M, Kofune T, Nakai T, Kasamaki Y and Hirayama A 2010 Temperature-controlled cooled-tip radiofrequency ablation in left ventricular myocardium *Int. Heart J.* **51**(3) 193–198
- Wattiez A, Khandwala S and Bruhat MA 1995 *Electrosurgery in Operative Endoscopy* (Hoboken, New Jersey: Wiley-Blackwell)
- Weaver JA and Stoll AM 1969 Mathematical model of skin exposed to thermal radiation *Aerospace Med.* **40**(1) 24–30
- Weber JC, Navarra G, Jiao LR, Nicholls JP, Jensen SL and Habib NA 2002 New technique for liver resection using heat coagulative necrosis *Ann. Surg.* **236**(5) 560-563
- Welp C, Siebers S, Ermert H and Werner J 2006 Investigation of the influence of blood flow rate on large vessel cooling in hepatic radiofrequency ablation *Biomed. Tech. (Berl)* **1**(5-6) 337-346
- Wittkampf FH, Hauer RN and Robles de Medina EO 1988 Radiofrequency ablation of atrial fibrillation with a cooled porous electrode catheter *J. Am. Coll. Cardiol.* **11** 17
- Wolf PA, Abbott RD and Kannel WB 1991 Atrial fibrillation as an independent risk factor for stroke: the Framingham Study *Stroke* **22** 983-988
- Xu F and Lu T 2011 *Introduction to skin biothermomechanics and thermal pain* (Berlin Heidelberg: Science Press Beijing and Springer-Verlag)
- Yang D, Converse MC, Mahvi DM and Webster JG 2007 Expanding the bioheat equation to include tissue internal water evaporation during heating *IEEE Trans. Biomed. Eng.* **54** 1382-1388
- Yao P and Morris DL 2006 Radiofrequency ablation-assisted liver resection: review of the literature and our experience *HPB (Oxford)* **8**(4) 248-254

- Yetkinler DN, Greenleaf JE and Sherman OH 2002 Histologic analysis of radiofrequency energy chondroplasty *Clin. Sports Med.* **21** 649-661
- Yokoyama K, Nakagawa H, Wittkamp FH, Pitha JV, Lazzara R and Jackman WM 2006 Comparison of electrode cooling between internal and open irrigation in radiofrequency ablation lesion depth and incidence of thrombus and steam pop *Circulation* **113**(1) 11–19
- Zeh A, Messer J, Davis J, Vasarhelyi A and Wohlrab D 2010 The Aquamantys system-an alternative to reduce blood loss in primary total hip arthroplasty? *J. Arthroplasty* **25**(7) 1072-1077
- Zhao G, Zhang HF, Guo X J, Luo DW and Gao DY 2007 Effect of blood flow and metabolism on multidimensional heat transfer during cryosurgery *Med. Eng. Phys.* **29**(2) 205-215
- Zhou B, Xu F, Chen CQ and Lu TJ 2010 Strain rate sensitivity of skin tissue under thermomechanical loading *Phil. Trans. R. Soc. A.* **368**(1912) 679–690

Publications

International peer-reviewed journals

- González-Suárez A, Jimenez Lozano JN, Berjano E and Franco W. Thermo-elastic response to radiofrequency heating with thermal damage quantification of subcutaneous adipose tissue of different fibrous septa architectures: a computational modeling study. *To be submitted to Lasers in Surgery and Medicine*
- González-Suárez A, Trujillo M, Koruth J, d'Avila A and Berjano E. RF Ablation with Catheters Placed on Opposing Sides of the Ventricular Wall: Computer Modeling Comparing Bipolar and Unipolar Modes. *Submitted: International Journal of Hyperthermia*
- González-Suárez A, Trujillo M, Burdío F, Andaluz A and Berjano E. Could the heat sink effect of blood flow inside large vessels protect the vessel wall from thermal damage during RF-assisted surgical resection? A computer modeling and an in vivo experimental study. *Submitted: Medical Physics*
- González Suárez A, Trujillo M and Berjano E 2013 Study of cardiac arrhythmias removal by using mathematical modeling *MSEL-Modelling in Science Education and Learning* **6**(3) 33-41
- González-Suárez A, Trujillo M, Burdío F, Andaluz A and Berjano E 2012 Feasibility study of an internally cooled bipolar applicator for RF coagulation of hepatic tissue: experimental and computational study *Int. J. Hyperthermia* **28**(7) 663-73
- González-Suárez A, Hornero F and Berjano EJ 2010a Mathematical modeling of epicardial RF ablation of atrial tissue with overlying epicardial fat *Open Biomed. Eng. J.* **4** 47-55

González-Suárez A, Hornero F and Berjano EJ 2010b Impedance measurement to assess epicardial fat prior to RF intraoperative cardiac ablation: a feasibility study using a computer model *Physiol. Meas.* **31**(11) N95-104

Conferences Proceedings

González-Suárez A, Trujillo M, Burdío F, Andaluz A and Berjano E. Computational and experimental study of the heat sink effect of blood flow inside large vessels as a protective mechanism during RF-assisted surgical resection. *Proceedings of the 19th Congress of the Spanish Society for Surgical Investigations* 2013, pp 35. **Poster.** Publication in: *British Journal of Surgery* 2014, 101 (Suppl. 1): 1-14.

González-Suárez A, Jimenez-Lozano JN and Franco W. Electrical response and thermal damage assessment of cutaneous and subcutaneous tissues to noninvasive radiofrequency heating: a computational modeling study. *Proceedings of the COMSOL Conference Boston* 2013. **Talk.**

González-Suárez A, Trujillo M, Koruth J, d'Avila A and Berjano E. Computational modeling to study the treatment of cardiac arrhythmias using radiofrequency ablation. *Proceedings of the Comsol Conference Europe* 2012, pp 1-6. **Talk.**

González-Suárez A, Trujillo Guillén M, Koruth J, d'Avila and Berjano E. Computer modeling of bipolar radiofrequency ablation of ventricular wall through epicardial approach. *Proceedings of the 18th Congress of the Spanish Society for Surgical Investigations* 2012, pp 13. **Talk.** Publication in: *British Journal of Surgery* 2013, 100 (Suppl. 1): 1-20.

González-Suárez A, Trujillo Guillén M and Berjano E. Electrical and thermal performance of a radiofrequency-assisted resection electrode: computational modeling. *Proceedings of the 18th Congress of the Spanish Society for Surgical Investigations* 2012, pp 35. **Poster.** Publication in: *British Journal of Surgery* 2013, 100 (Suppl. 1): 1-20.

- González-Suárez A, Trujillo Guillén M, Koruth J, d'Avila A and Berjano Zanón E. Ablación por radiofrecuencia de la pared ventricular mediante acceso epicárdico: estudio computacional. *Proceedings of the XXX Congress of the Spanish Society of Biomedical Engineering* 2012, pp 1-4. **Talk.**
- González-Suárez A, Trujillo M and Berjano E. Modelización matemática en ablación por radiofrecuencia de la pared ventricular para la eliminación de arritmias cardíacas. *Proceedings of the III Conference on Mathematical Modeling of the Valencia Polytechnic University* 2012, pp 14. **Poster.**
- González Suárez A, Trujillo Guillén M and Berjano Zanón E. Estudio experimental y teórico de un electrodo bipolar internamente refrigerado para coagulación de tejido hepático mediante corrientes de radiofrecuencia. *Proceedings of the XXIX Congress of the Spanish Society of Biomedical Engineering* 2011, pp 339-42. **Talk.**
- González Suárez A, Trujillo Guillén M and Berjano Zanón E. Ablación por radiofrecuencia empleando catéteres colocados en los lados opuestos de la pared ventricular: comparative entre el modo bipolar y secuencial unipolar mediante modelado computacional. *Proceedings of the XXIX Congress of the Spanish Society of Biomedical Engineering* 2011, pp 431-4. **Talk.**
- González-Suárez A, Alba J, Trujillo M and Berjano EJ. Experimental and theoretical study of an internally cooled bipolar electrode for RF coagulation of biological tissues. *Proceedings of the 33rd Annual International Conference of the IEEE Engineering in Medicine and Biology Society* 2011, pp 6878-81. **Talk.**
- Alba J, González-Suárez A, Trujillo M and Berjano EJ. Theoretical and experimental study on RF tumor ablation with internally cooled electrodes: When does the roll-off occur? *Proceedings of the 33rd Annual International Conference of the IEEE Engineering in Medicine and Biology Society* 2011, pp. 314-7. **Poster.**

- González-Suárez A, Trujillo M and Berjano E. Estudio de elementos finitos de un electrodo bipolar internamente refrigerado para coagulación de tejidos biológicos mediante corrientes de radiofrecuencia. *Proceedings of the V Latin American Congress of Biomedical Engineering* 2011, vol. 33. **Talk.**
- González Suárez A and Berjano Zanón EJ. Estudio de elementos finitos de un electrodo bipolar internamente refrigerado para coagulación de tejidos biológicos mediante corrientes de radiofrecuencia. *Proceedings of the XXVIII Congress of the Spanish Society of Biomedical Engineering* 2010, pp 181. **Talk.**
- González A, Hornero F and Berjano EJ. Impedance measurement to assess the epicardial fat prior to RF intraoperative cardiac ablation: feasibility study using a computer model. *Proceedings of the 1st International Conference on Multiphysics Simulation- Advanced Methods for Industrial Engineering* 2010. **Talk.**
- González Suárez A, Hornero F and Berjano Zanón EJ. Valoración pre-ablación de la grasa epicárdica: prueba de concepto mediante modelado computacional. *Proceedings of the XXVII Congress of the Spanish Society of Biomedical Engineering* 2009, pp 279-82. **Talk.**

List of Figures

Figure 1.1. RFA using monopolar (a) and bipolar (b) arrangements. AE: active electrode and DE: dispersive electrode	27
Figure 1.2. Cooled electrodes: (a) closed-irrigated electrode (or internally cooled electrode) and (b) open-irrigated electrode	29
Figure 1.3. Overview of percutaneous cardiac ablation for treatment of a cardiac arrhythmia.....	31
Figure 1.4. Multi-electrode catheter probes: (a) closed-irrigated-tip and (b) open-irrigated-tip catheter	31
Figure 1.5. Uni-electrode probes: Cardioblate® monopolar pens	32
Figure 1.6. Electrosurgical forceps for RF bipolar cardiac ablation: (a) open-irrigated and (b) closed-irrigated forceps	33
Figure 1.7. Liver with tumor showing the resection line on removing the tissue fragment containing the tumor	34
Figure 1.8. (a) Habib 4X multiprobe RF device, (b) In-line RFA device, and (c) process used to achieve a hepatic resection with these systems.....	35
Figure 1.9. Ligasure RF device for open (a) and laparoscopic surgery (b).....	36
Figure 1.10. TissueLink dissecting sealer for RF-assisted hepatic resection	36
Figure 1.11. Coolinside RF device for open (a) and laparoscopic surgery (b)	37
Figure 1.12. The skin-fat structure composed of three layers: epidermis, dermis and subcutaneous tissue.....	38
Figure 1.13. RF monopolar applicator which consists of a multidimensional series of tightly spaced concentric rings.....	39
Figure 1.14. (a) Bipolar RF handpiece with the aspirating cannula: cannula for BodyTite system (left) and V-dissector tip for CelluTite system (right). (b) RFAL handpiece inserted into the body with directional energy applied to adipose fat and fibrous septa	41

Figure 2.1.	Explanted heart in which the presence of epicardial fat can be noted on left atrium..	63
Figure 2.2.	Two-dimensional theoretical model proposed	64
Figure 2.3.	Temperature distributions for three modes of delivering RF power	65
Figure 2.4.	Temperature distributions for RF ablation using a cooled electrode and for four values of epicardial fat thickness.	66
Figure 2.5.	Maximal temperature and lesion depth in the atrial wall for RF ablation using a dry electrode with different protocols.	67
Figure 3.1.	Physical situation considered in the study of the estimation of the epicardial fat profile.	78
Figure 3.2.	Theoretical model proposed with a uniform fat profile.	78
Figure 3.3.	Impedance measurements conducted by a tetrapolar technique	79
Figure 3.4.	Theoretical models with different epicardial fat profiles	80
Figure 3.5.	Model used to study the effect of lateral width of epicardial fat on the measured impedance.	81
Figure 3.6.	Impedance calculated for uniform (a), linear (b), convex (c), and concave (d) fat profiles.	83
Figure 3.7.	Impedance measurements by changing the lateral width of epicardial fat and the epicardial fat layer thickness	84
Figure 4.1.	Geometry of the computational model for interventricular septum ablation	101
Figure 4.2.	Electrical boundary conditions of the model for interventricular septum ablation for (a) bipolar mode, (b) sequential unipolar mode and (c) simultaneous unipolar mode; (d) thermal boundary conditions for all cases.	102
Figure 4.3.	Temperature distribution in the tissue after RFA across the interventricular septum for different septum thickness, considering three modes of ablation: (a) bipolar mode, (b) sequential unipolar mode, and (c) simultaneous unipolar mode.	103

Figure 4.4.	Temperature distribution in the tissue after RFA across the ventricular free wall with pericardial fluid in the epicardial space, considering different wall thickness and three modes of ablation: (a) bipolar mode, (b) sequential unipolar mode, and (c) simultaneous unipolar mode ..	104
Figure 4.5.	Temperature distributions after of RFA across the ventricular free wall with the epicardial catheter surrounded by air, considering three modes of ablation: (a) bipolar mode, (b) sequential unipolar mode, and (c) simultaneous unipolar mode.....	105
Figure 4.6.	Temperature distributions after of RFA with bipolar mode across the ventricular free wall comparing two orientations of the epicardial catheter: (a) perpendicular and (b) parallel to the epicardium.....	105
Figure 4.7.	Temperature distributions in the tissue after of RFA with bipolar mode (a) and simultaneous unipolar mode (b) across the interventricular septum, increasing the misalignment between catheters.....	106
Figure 4.8.	Temperature distributions in the tissue after of RFA with bipolar mode and simultaneous unipolar mode (b) across the ventricular free wall, increasing the misalignment between catheters.	107
Figure 5.1.	Top (a) and side (b) views of the internally cooled bipolar applicator proposed to coagulate hepatic tissue.	126
Figure 5.2.	(a) Physical situation considered in the study. (b) Computational model proposed.....	127
Figure 5.3.	Electrical (a) and thermal (b) boundary conditions of the computational model	128
Figure 5.4.	Thermal lesions created after RF heating. (a) Surface view of lesion created in the ex vivo model, (b) side views of lesions created in the ex vivo and in vivo models. (c) Temperature distributions from computer simulations of the ex vivo and in vivo conditions.....	129
Figure 5.5.	Impedance progresses during RF heating in the ex vivo (a) and in vivo study (b)	130

Figure 5.6.	Lesion depths estimated from computer modeling of in vivo conditions for the applicator under test (D1) and the smaller design (D2) when changing applied voltage and duration.....	131
Figure 5.7.	Impedance progresses and tissue temperature distributions computed for in vivo conditions for the applicator under test while changing the voltage for a time	132
Figure 6.1.	Coolinside surgical device for RF-assisted resection based on an internally cooled electrode.....	156
Figure 6.2.	Geometry and dimensions of the three-dimensional model built for the study.....	157
Figure 6.3.	(a) Electrical and thermal boundary conditions of the numerical model (b) Model used in the analysis of boundary conditions of the blood vessel.....	158
Figure 6.4.	Procedure used to obtain the distances and area between the RF lesion and the vessel and to assess possible damage in the vessel wall.....	159
Figure 6.5.	(a) Temperature distribution in the tissue after RF heating computed by three different methods of modeling the cooling effect of the blood flow inside the portal vein (b) Distances and area between the portal vein and the thermal lesion.....	160
Figure 6.6.	Evolution of the temperature distribution in the tissue during RF heating, considering total tissue-device contact, with the portal vein perpendicular to the device and at 5 mm below its center.	161
Figure 6.7.	Thermal lesions created in the tissue after RF heating, varying vessel-device distance, device-tissue contact and vessel position.....	162
Figure 6.8.	Distances obtained between the portal vein and the thermal lesion for each vessel-device distance.	163
Figure 6.9.	Ultrasonography employed to measure the distance of the vessel-device distance and the vessel diameter (a); experimental (b) and computational (c) thermal lesions created in the tissue.....	164

Figure 7.1.	Geometry and dimensions of the model built, which is composed of three tissue layers of skin, fat+septa and muscle and RF applicator..	180
Figure 7.2.	High-resolution in vivo MRIs of the skin of two females corresponding with two conditions of density of fibrous septa: (a) Case 1: Low density; and (b) Case 2: High density	180
Figure 7.3.	Voltage distribution in the tissue for two conditions of density of fibrous septa: (a) Case 1; and (b) Case 2. (c) Voltage profiles	181
Figure 7.4.	Electric field norm distribution within tissue for two conditions of density of fibrous septa: (a) Case 1; and (b) Case 2. (c) Comparison of the electric field norm profiles.....	182
Figure 7.5.	Total electric power absorption (surface map) and electric current density (arrows) for two conditions of density of fibrous septa: (a) Case 1 and (c) Case 2. (b) and (d) show close-up views of Cases 1 and 2, respectively	183
Figure 7.6.	Temperature distribution in the tissue after RF heating for two conditions of density of fibrous septa: (a) Case 1, and (b) Case 2	184
Figure 7.7.	Time progression of depth profiles of temperature profiles for two conditions of density of fibrous septa: Case 1 and Case 2	184
Figure 7.8.	Volumetric strain map for two conditions of density of fibrous septa: (a) and (c) Case 1; (b) and (d) Case 2.	185
Figure 7.9.	Time progress of the volumetric strain profiles for two conditions of density of fibrous septa: (a) Case 1; and (b) Case 2	186
Figure 7.10.	Stress distribution map of Von Mises Stress for two conditions of density of fibrous septa: (a) Case 1; and (b) Case 2. Von Mises Stress profile for both cases (c).....	187
Figure 7.11.	Thermal damage zones computed after RF heating (200 W power) considering the subcutaneous tissue as a homogeneous layer (solid line) and for two conditions of fibrous septa density (dotted lines): (a) Case 1, and (b) Case 2	188

List of Tables

Table 2.1.	Characteristics of the elements employed in the computer modeling..	58
Table 2.2.	Effect of frequency and thickness of fat layer on lesion geometry and maximal temperature at a constant voltage of 30 V for 60 s.....	59
Table 2.3.	Effect of frequency and fat thickness on lesion geometry and maximal temperature at a constant temperature of 70°C for 60 s.	60
Table 2.4.	Effect of frequency and fat thickness on lesion geometry and maximal temperature at a constant current of 12 mA for 60 s.	61
Table 2.5.	Effect of frequency and fat thickness on lesion geometry and maximal temperature using an RF cooled electrode and 38 V for 60 s.	62
Table 4.1.	Thermal and electrical characteristics of the elements of the numerical models.....	98
Table 4.2.	Lesion dimensions in the interventricular septum for different septum thickness and three modes of RF ablation: bipolar mode, sequential unipolar mode and simultaneous unipolar mode.....	99
Table 4.3.	Lesion dimensions in the ventricular free wall with the epicardial catheter surrounded by pericardial fluid for different wall thickness and three modes of RF ablation: bipolar mode, sequential unipolar mode and simultaneous unipolar mode.....	100
Table 5.1.	Thermal and electrical characteristics of the elements employed in the computational modeling	125
Table 5.2.	Lesions dimensions created by the internally cooled bipolar applicator under ex vivo and in vivo experimental conditions together with the values estimated from computer simulations	125
Table 6.1.	Thermal and electrical characteristics of the elements employed in the numerical modeling	154
Table 6.2.	Initial impedance, initial power, distributed energy, maximum temperature reached in the tissue for the cases studied.....	155

Table 7.1. Electrical, thermal and elastic properties of the elements employed in the computer modeling179

Table 7.2. Electrical, thermal and elastic boundary conditions.....179

